Methods for Sensing, Analysis and Computation of Loads and Distributed Damage in Bridges

BY

Saeed Karim Baba Najad Mamaghani

M.Sc., University of Tehran, Tehran, Iran, 2011

B.Sc., University of Tehran, Tehran, Iran, 2009

Thesis

Submitted as partial fulfillment of the requirements

for the degree of Doctor of Philosophy in Civil Engineering

to the Graduate College of the University of Illinois at Chicago, 2015

Chicago, Illinois

Defense Committee:

Farhad Ansari, Chair and Adviser

Eduard Karpov

Mustafa Mahamid

Didem Ozevin

Michael Stroscio, Electrical and Computer Engineering Department

I dedicate my thesis to my lovely wife, Raha, my dear mother, Mahin, my kind father, Rasoul as well as my brother, Masoud. Their never ending love and favor have greatly strengthened and encouraged me during the course of this research. I will try all my bests in my life to compensate and become their honor.

ACKNOWLEDGMENTS

AUTHORS CONTRIBUTIONS

Some of the results and discussions in this thesis are partially derived from my published paper with written permission from the journal (see appendix). Below, the contributions of all the co-authors are listed:

Authors' contributions in the below citation (mainly used in Chapters 1 and 2):

"Generalized Method and Monitoring Technique for Shear Strain Based Bridge Weigh in Motion" by Bao, T., Babanajad, S.K., Taylor, T., and Ansari, F., Journal of Bridge Engineering, ASCE, 04015029, 2015, 1-13

F. Ansari has conceived the new approach of using rosette shear sensor for BWIM purposes since 2009. T. Bao has initiated the methodology and then was developed by T. Bao and S.K. Babanajad in details. All the calculation and preparation of tables and figures as well as the data analysis of the paper was performed by S.K. Babanajad. The draft was initially drafted by T. Bao and S.K. Babanajad and then reviewed by T. Taylor and F. Ansari. For Lambert Road Bridge, the instrumentation and calibration tests were primarily done by T. Taylor. Only some of the results were used in current journal paper and thesis. For Salt Creek Bridge, the instrumentation was done by T. Taylor and the calibration tests were done by T. Taylor, S.K. Babanajad, and T. Bao. For Lock Street Bridge, the instrumentation as well as the calibration tests were done by T. Taylor and S.K. Babanajad. F. Ansari led the project and supervised the entire process.

Authors' contributions in the below citation (mainly used in Chapters 1 and 3):

"Virtual Reference Approach for Dynamic Distributed Sensing of Damage in Large Structures" by Babanajad, S.K., Zhan, Y., Taylor, T., and Ansari, F. Journal of Aerospace Engineering, ASCE, under review

F. Ansari and S.K. Babanajad have conceived the new approach and also designed the experiment. S.K. Babanajad has developed the methodology. T. Taylor built the testing set up. T. Taylor, S.K. Babanajad, and Y. Zhan have instrumented and performed the experimental program. S.K. Babanajad, and Y. Zhan have analyzed the experimental results. All the calculation and preparation of tables and figures as well as manuscript were performed by S.K. Babanajad. Then it was reviewed by F. Ansari. F. Ansari led the project and supervised the entire process.

TABLE OF CONTENTS

CHAPTER	PAGE

LIST OF TABLES

LIST OF FIGURES

Summary

The worldwide aging of the infrastructure and the development of new technologies in the construction industry provided a need for structural health monitoring (SHM). SHM provides a tool for owners and researchers to assess the condition of a structure and monitor its behavior under real life conditions. Road transport and the related infrastructures are clearly an integral part of the economic, political, and social development of the western world. As an example, highway bridges as a major part of infrastructures can be greatly damaged by excessively heavy vehicles or severe environmental conditions. It is therefore, important to assure that such facilities are well maintained and function properly in order to avoid major failures or the need for costly repairs. In current thesis, it is attempted to innovate techniques in order to measure the vehicles loads affecting the bridge elements as well as damage detection methods to monitor the defects along the in-service bridge structural components.

Bridge Weigh-in-Motion (BWIM) is using an existing bridge to weigh trucks while they are moving at full highway speeds. A new method of BWIM has been established in order to weigh the passing trucks relying on the shear strain measurements near the bridge abutments which differs from the flexural strain based traditional systems. The shear strain are measured using the rosettes sensors installed on the webs of bridge girders to directly measure the individual axle weights of trucks passing over the bridge abutments. Two concrete slab on steel girder bridges, and a box girder prestressed concrete with different structural types, span lengths, and different sizes were instrumented for the performance

verification of the proposed BWIM system. A series of truck runs were implemented in the field to calibrate and evaluate the proposed BWIM system's efficiency.

In addition, current research formulated a reference-free distributed damage detection method in order to locate the defects that occur in structures under in-service operating conditions. The sensing method is developed on the basis of Brillouin scattering phenomena. It employs the dynamic distributed strain measurement data in order to sense the structural perturbations under in-service operations, i.e. bridges subjected to traffic loadings, or aircrafts during flights. The advantage of the method developed in this study is that it enables the structure to be monitored at any stage during its service life without the need for prior reference data. An experimental program was designed to investigate the feasibility of the proposed approach in detecting the locations of very small defects. Laboratory experiments were designed in order to simulate the effect of ambient conditions in bridges, especially in terms of realistic displacements, i.e. deflections occurring in highway bridges.

In a following effort, a theoretical model was also investigated to analysis the strain transfer mechanism from the structure surface to the distributed optical fiber components in the presence of local defects. The main objective pertained to the accurate quantification of local defects sizes based on distributed monitoring of strains in large structural systems. The theoretical formulation simulated the strain distribution within the components of an optical fiber crossing over a single crack opening. The proposed model was formulated in a manner to quantify defects in the presence of structural vibration. Both linear and nonlinear mechanical characteristics of optical fiber components were also assumed in the formulation. The spatial resolution effect was further numerically implemented within the

formulation in order to simulate the measurement configurations. An experimental program was designed for calibration as well as the validation of theoretical formulation. The experiments involved dynamic tests of a 15 meter long steel I beam with two fabricated defects with small opening displacements ranging between 50 and 550 microns.

Chapter I: Introduction

1.1. Background

The worldwide aging of the infrastructure and the development of new technologies in the construction industry provided a need for structural health monitoring (SHM). SHM provides a tool for owners and researchers to assess the condition of a structure and monitor its behavior under real life conditions. Rytter (1993) has proposed a four level SHM classification system in order to sort the SHM activities. Level 1 damage identification method determines the presence of damage in the structure while level 2 technique is additionally locate the damage along the structure. Level 3 method could also quantify the severity of damage, as well as its presence and location. In the following step, level 4 also estimates the remaining service life of structure in addition to the information released by level 3. Determining the remaining service life of the structures is considered as the critical issue regarding to the infrastructures condition (Zarafshan 2013). These structures play strategically and vital roles in the life of countries. Therefore, keeping the infrastructures in a well conditional level is the top priority of the governments and owners priorities.

Road transport and the related infrastructures are clearly an integral part of the economic, political, and social development of the western world. Highway bridges can

be greatly damaged by excessively heavy vehicles or severe environmental conditions. Based on a report released by Lambert and Crawley (2011), 11.5 percent, or 69,000, bridges need serious attention or replacement. The report mentioned that spending budget for bridge repair and maintenance has severely lagged estimates of needed funding. It was noted that from 2006 through 2009 the federal government increased the budget by $650 million, while the Federal Highway Administration (FHWA) estimated that $22.8 billion was needed for deficiencies fixation. Also, based on the American Society of Civil Engineers (ASCE) report on 2009 it is expected that the federal government spends $17 billion annually to improve current bridge conditions, however, it is only invested $10.5 billion annually on bridges (Lambert and Crawley 2011). Incidents of the past have taught us that catastrophic failures are associated with loss of many lives, disruption of service, and adverse economic ramifications. Degradation of infrastructures such as bridges lowers the quality of service and necessitates increase in frequency of costly repairs, replacements, and infrastructure shut downs. It is therefore, important to assure that such facilities are well maintained and function properly in order to avoid major failures or the need for costly repairs. To accomplish this, it will be necessary to inspect and monitor the health of the structural systems frequently, and with optimum degree of efficiency in order to detect and quantify all the defects at their early stages of formation.

There are two main categories that can be evaluated on the bridges. The first one corresponds to the analysis of the action affecting the bridge components. In other words, it is necessary to know the external parameters directly/indirectly affecting the structural components of bridges. The vehicles axle loads, thermal cycles, exposure to

adverse environments, and fabrication imperfections are the examples of external actions. Accurate and detailed information such as frequency and magnitude of passing trucks are necessarily needed to evaluate the performance of bridge to the overweighed trucks. Therefore, it is necessary to find a comprehensive method to obtain all the information of the vehicles crossing over the bridges. Static and dynamic weighing are the techniques generally used for measuring the vehicles' gross vehicle weights (GVW) as well as the individual axle weights. The most common practice types of these systems are briefly introduced in the following section of 1.2.

The second subcategory includes the analysis of bridge reaction in terms of applied action. Bridge deflection, vibration, defects, corrosion etc. are the examples of reactions generated by the bridges in response to the applied actions. All of these characteristics should be evaluated along the structure's life in order to prevent any major and catastrophic failures.

As pinpointed by Zarafshan (2013), visual inspection with the aid of simple instruments such as Schmidt Hammer could successfully implement condition assessment of the bridges. However, with constructing complex structures as well as increasing the skilled labor wage, the visual inspection technique was questioned as a proper tool box for bridge SHM purposes. To address the issues regarding the visual inspection, three major categories of SHM techniques were employed to facilitate the bridge monitoring. These three techniques include Nondestructive Test and Evaluation methods (NDT/NDE), Global Vibration Response, and Fiber Optic Sensing. These different techniques as well as their advantages and disadvantages are briefly discussed in the following sections of 1.3 through 1.5.

1.2. Static/Dynamic Weighing

In the past decades both weight and volume of the trucks increased due to the high demand in the materials and instruments transportation. The truck overloading has caused major problems in the highway roads and bridges. Therefore, the states DOTs were mandated to increase the limitation and enforcement penalties in order to avoid the truck drivers from overloading the trucks. The enforcements and standards are all established based on the static (or unchanged) weights of trucks' GVW and individual axles.

The two most common types of static weighing systems consist of platform scales that remain in a fixed location and portable scales that vehicles can drive onto resulting in individual wheel loads (Quilligan 2003). These systems are normally used by police departments or different agencies to detect overweight trucks by randomly stopping the traffic. This data could also be used for statistical purposes. These systems individually weigh the axle's static weights.

a) Platform Scales:

A truck scale is comprised of a rigid supporting frame, several load cells and a system to calculate and indicate the truck weight. These systems can calculate the GVW or individual axle weights within 0.5% error. However, from a data collection and weight enforcement perspective, they are subject to a number of drawbacks such as delaying the traffic, temporary operation, and scale avoidance of offending vehicles by selecting routes known not to have these scales (Quilligan 2003). Fig. 1.1 demonstrates an example of Platform scale.

Figure 1.1 Platform Scale

b) Portable Wheel Scales:

These systems allow for measuring wheel and axle loads, as well as GVW. Each wheel is weighed separately or in groups, as a consequence their accuracy is lower than that of platform scales. The number of scales used may cause additional errors due to abnormal weight transfer between the axles. This condition could be caused by tilting of the vehicle, improper leveling of the scale, site unevenness, or friction in the suspension. This can be avoided by using the same number of scales as the number of wheels. These systems allow the GVW to be calculated with less than 3% error (Quilligan 2003).

As mentioned previously, since these systems measure the weight of trucks in their static condition the results have slight errors and could be considered as the actual weights of trucks, which enable them to be used for enforcement purposes. However, the weigh stations are primarily located on interstates entering the states and could only screen few vehicles entering the state for weight and equipment violations. For example, for I-80/94 highway ~28,660 trucks cross each day and ~37 trucks are over 90,000 lbs each day while the weigh stations could only identify 14 trucks over 85,000

5

over a two month period. In other words, only 0.6% of overweighed trucks could be identified (Newland 2006).

Alternatively, Weigh-in-motion (WIM) systems capture and measure individual axles, GVW, axle spacing as well as speeds of vehicles passing over the measurement site which is typically instrumented on the road or over the bridge (Quilligan 2003). Compared to static weighing (e.g. weigh stations or portable scales), WIM techniques are able to measure all above mentioned features of passing vehicles without closuring the road or stopping the vehicles (en.Wikipedia.org/weigh-in-motion). This capacity enables the agencies to collect all the information of vehicles (specifically trucks) travelling on the highways. Also, WIM techniques obtain the weight information of all commercial vehicles in an easier way without stopping the underweight-limitation trucks to stop by either weigh stations or portable scales (Quilligan 2003). Fig. 1.2 represents a general schematic view of WIM packages. The WIM systems fall in two main categories of Pavement WIM and Bridge WIM, which will be explained in detail in the following:
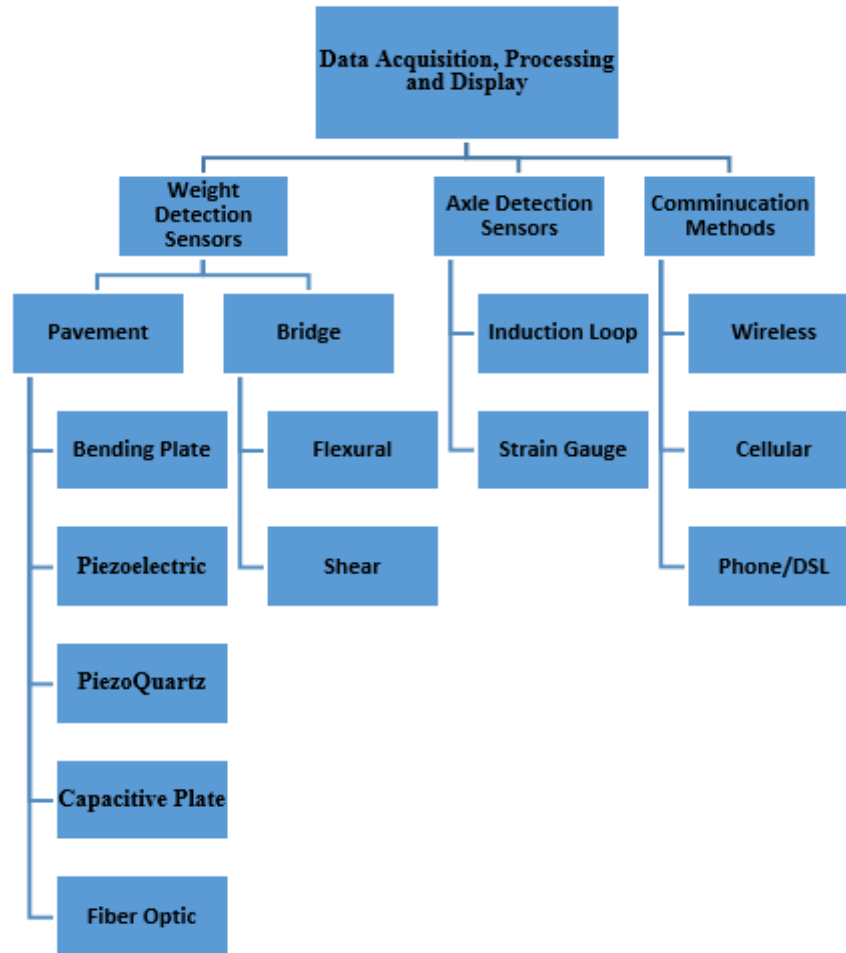
Figure 1.2 WIM System Configurations

a) Pavement WIM Systems:

In the Pavement systems the sensors are installed inside the pavements in perpendicular to the direction of traffic (Quilligan 2003). The system operations rely on the measurement of specific property of the installed sensor which is changing based on the applied load. Pavement WIM system is the most common system used to detect overweight trucks while they are on the road (Fig. 1.3). This system is advantageous over the aforementioned systems since there is no need to stop the traffic and weigh the truck out of the roadway. This system could be installed on the road and controlled

automatically and remotely. The major point of a Pavement WIM system is the capability of recording all truck passage on the road. This data further could be used for transportation and enforcement purposes. The system uses two inductive loops for axle detection, and calculation of velocity and axle spacing. The piezoelectric strips are used to calculate the axle weights. Since the measurements are performed while the vehicles move on the road, dynamic effects will cause deviation in the measurements from the static axle weights. In some cases the errors are considerable and could not be considered reliable.

Figure 1.3 Pavement WIM (www.invicom.com)

Various types of pavement sensors exist with their own specifications and limitations. The Pavement WIM sensors fall into two main categories namely Bending Plate (Load Sensors) and Strip Sensors: Bending Plate WIM systems use metal plates in which the sensors are attached to their underside, as shown in Fig. 1.4. The strain is measured by the strain gauges, which is exerted by the rolling tires and the dynamic loads are calculated. Load cell WIM systems (see Fig. 1.5) are available in two types, hydraulic and strain gauge. The hydraulic pressure is measured and correlated to vehicle weight when the tire pressure is exerted on the load cell. One of major disadvantages of these

systems is their permanent installation in normal roads. To install, it is necessary to build a concrete foundation for the system as a frame support, which is time and cost consuming (Quilligan 2003).

Figure 1.4 Bending Plate Scale (www.irdinc.com)

Figure 1.5 Single Load Cell Scale (www.irdinc.com)

With Strip Sensors, unlike Bending Plates, only a portion of the tire is covered by the width of the strip. For this type, different factors such as truck dynamics, road unevenness and temperature must be considered. These sensors are embedded in grooves in the road and are small in size. This specification makes them more economical while consequently their results are less accurate. This type of sensor is

categorized as piezoelectric, capacitive, quartz and fiber optic sensors, which are briefly explained in the following, mainly derived from Quilligan (2003):

- Piezoelectric: The most common form of WIM sensor consists of copper encased piezoelectric material which surrounds a copper wire. As load is applied to the piezoelectric material a charge is induced and conducted to the sensing system by the copper wires.

- Piezo-Quartz Crystal: For this sensor a quartz crystal is mounted within an aluminum extrusion. This minimizes the effects of lateral stresses while maximizing load transfer in the vertical direction. As load is applied the electrical properties of the crystal changes proportionally.

- Capacitive Systems: This sensor consists of two overlapping, electrically charged metal plates. As load is applied the upper plate deflects causing a change in the sensors overall capacitance.

- Fiber Optic: The construction of this sensor consists of two metal plates welded and encasing a glass fiber. As load is applied the stresses cause a proportional phase shift in the modes of light travelling through the fiber.

All types of Pavement WIM systems include inductive loops to define the vehicle entry and exit from the WIM scale. These signals are used to start and stop the measurements for each vehicle passing over the sensors (en.Wikipedia.org/weigh-in-motion). For toll gate or low speed application, other types of vehicle sensors such as light curtains, axle sensors or piezocables may be replaced with inductive loops (www.invicom.com).

As reported by Quilligan (2003), the negative points of Pavement WIM system are listed as:

- For system installation, the road must be fully or partially closed.

- To install the system, the roadway should be cut to open enough space for installation. This could cause premature degrading of the roadway and cause problems for road performance.

- The installed system will face different environmental conditions during the seasons affecting the system's durability.

- The system and the wiring must be protected against thieves, animals, and natural disasters.

- The system is visible to drivers and could be avoided by truck drivers.

- The system must be periodically calibrated for different temperatures during different seasons. Based on the reports of different companies, these systems have serious problems with temperature variations.

- These systems have serious problems in accurate estimation of static loads from measurements of dynamic impact forces applied by the axles. The sensors placement and the interaction between the tires and sensors would adversely affect the performance of system.

b) Bridge WIM Systems

Bridge Weigh-in-Motion (BWIM) is using an existing bridge to weigh trucks while they are moving at full highway speeds. The calculations would be based on measurement

of the deformation of the bridge to estimate the attributes of passing traffic loads. The advantageous points of this system over Pavement WIM systems are listed as:

- The roadway need not be closed for the system installation.

- Pavement WIM systems use instantaneous force for the time the tire is supported on the WIM sensor. The sensor width and vehicle speed will determine the time that the tire is on the sensor and the oscillation is recorded. The deviations from the actual weights (static) for a pavement in good condition can be well in excess of 30%, while the BWIM could overcome this problem (Wave 2001). BWIM systems are capable of measuring truck responses continuously as the truck travels on the bridge.

- Since the system must be installed on the steel or concrete girders of bridge structures, there is no need to cut into any pavement. Moreover, the installation of sensors on the girder will only be performed using epoxies or micro-welding.

- Installation on different lanes (even high speed lanes) is possible without any limitation.

- Since the system will be installed on the bottom of the bridge, it is protected from environmental conditions during the different seasons.

- The system and the wires could be easily protected by conduits and enclosures.

- The system is not visible to drivers.

- Accuracy is similar to other pavement-based WIM technologies

According to Quilligan (2003), different techniques of existing BWIM can be categorized in different types including:

MOSES' Algorithm: In the 1970's the Federal Highway Administration started efforts regarding applying BWIM systems. Moses (1979) for the first time developed a technique to predict the axle and gross weights of passing trucks using instrumented bridge girders. In Moses' approach two different types of measurement systems were employed, tape switches in the pavement for measurement of truck speeds and axle spacing, and strain gauges on the bottom flanges of girders for the measurement of flexural strains. Further improvements were made on the BWIM by Moses and Ghosn (1983). They used an influence surface instead of an influence line to distinguish the trucks' weights crossing over the bridge in multiple lanes. The influence surface has been extracted from the recorded strain data at the passage time of calibrated truck.

AXWAY and CULWAY: In 1984, a new BWIM technique was developed by Peters (1984) which was based on that fact that the GVW of a truck is proportional to the area under its influence line. The GVW is determined as the area under the strain response. The axle weights are varied in an iterative process to decrease the distance between the measured and expected (calculated) responses. Later, Peters improved his technique and used culverts (CULWAY) (Peters 1986; Peters 1998). The new technique had the capability to remove the problem of dynamics encountered due to the damping effects of the surrounding soil and the absence of any expansion joints.

DuWIM: Based on the WAVE project, a group of staff and professors from Trinity College Dublin (TCD) and University College Dublin (UCD) used their own BWIM algorithm (which is based on MOSES' concept) on the instrumented bridge located in Lulea, Sweden. This system is not automatic and is not commercialized. A unique

13

feature of the DuWIM system was a "point by point" graphical method of calculating the influence line from the bridge response.

SiWIM: Based on the WAVE project, a group of staff and professors from Slovenian National Building and Civil Engineering Institute (ZAG) used an improved version of MOSES' BWIM algorithm on the instrumented bridge located in Lulea, Sweden (Jacob 2002). This system is now fully automatic and is commercialized. A unique feature of the SiWIM system is that SiWIM passes the results to an optimization algorithm, which has been shown to increase the accuracy of results.

Later on, since the tape switches degraded within short periods of use, Žnidarič et al. (2002) proposed a Free-of-Axle Detector (FAD) system by installing separate sets of strain sensors under bridges. The strain sensors were either exclusively used for axle detection or as part of the overall weigh-in-motion measurement system. However, only bridges with sharp peaks in flexural strain responses, i.e. short spans or those with secondary elements such as cross beams were suitable for the FAD system (Kalin et al. 2006). Other BWIM systems that have been developed over the past few years include the area method (Ojio and Yamada 2002; Cardini and DeWolf 2009), reaction force method (Ojio and Yamada 2002), and the moving force identification method (Law et al. 1997; Zhu and Law 2006; Yu and Chan 2007; Pinkaew 2006; Rowley et al. 2009; Deesomsuk and Pinkaew 2010). In general, two approaches have been employed for the construction of flexural strain influence lines. Quilligan (2003) and O'Brien et al. (2006) directly obtained the influence lines by measuring the flexural strains during the calibration process at the bridge sites. Also, Quilligan (2003) has considered the 2D multi vehicle algorithm (influence surface) to increase the accuracy of the BWIM. Others

constructed the influence lines numerically based on the geometrical and structural configuration of the bridges (Lechner et al. 2013). Overall, the prevailing approach that has been used in the majority of BWIM systems is the method introduced by MOSES including the improvements following its introduction (González et al. 2008). However, all the aforementioned methods only improve the existing conventional BWIM methods and do not introduce a completely new BWIM technique. In most cases, the proposed improvements could not be used as an applicable BWIM technique which is able to identify and weigh the moving trucks in a real time manner.

1.3. NDT/NDE methods

Recently several researchers innovated different techniques for employment in bridge health monitoring to solve the issues regarding the simple visual inspection techniques (Zarafshan 2013). The NDT/NDE techniques are rich in locating and quantification of defects along the structures; however, they require painstaking point-by-point interrogation of every single element of the structure in order to determine the location and extent of multiple defects. Examples of the NDT methods commonly employed for inspection of metallic materials include acoustic emissions (Nair and Cai 2010; Yaman et al. 2001), liquid penetration test (Van Dalen et al. 2009; Hellier 2001), eddy current (Wu et al. 2014;), magnetic particle (Chedister 2002), radiography (Cawley 2001; Sherlock 1996), corrosion measurements (Zhu et al. 1998), microwave, thermography, X-ray diffraction (Maeder et al. 1981), and Ultrasonics (Atzlesberger et al. 2013; Fujita and Masuda 2014). Additional expenses at the time of installation as well as human resources are required for a comprehensive SHM by using NDT tests. Issues such as

resolution of measurements, measurement access requirements, reliability, flaw size, and applicability to different construction materials limits their capabilities (Ansari 2005). Point sensing only yields information for its specific location and requires many points (locations) along the structure. The details regarding the comprehensive review of these techniques falls out of scope of the current thesis and is recommended to study the other available references as Farrar and Jauregui (1998) and Fan and Qiao (2011).

1.4. Global Vibration Response Methods

Over the past decades, a number of vibration based damage detection techniques have been developed. The main idea of these methods is to correlate the change in physical properties of the damaged structure to measurable changes in modal properties. Modal properties include natural frequency, mode shape and modal damping of the structure (Zarafshan and Ansari 2014). It is possible that these changes covered by the alterations resulted from service and ambient conditions. For this reason, the damage identification methods relying on the frequency evaluation are investigated only in laboratory scales rather than testing of real structures with considering the operating environment (Fan and Qiao 2011). Herein few of successful global vibration techniques previously have been listed by An et al. (2014) include: neural network methods for bridge monitoring (Lee et al. 2005, 2002); stochastic traffic modeling-based method (Chen et al. 2009); model updating methods (Jaishi and Ren 2005; Brownjohn et al. 2003; Lin et al. 2009); direct stiffness calculation methods (Huth et al. 2005; Maeck et al. 2001), and load carrying estimation of bridge (Lee et al. 2007; Moyo et al. 2004). Shortcoming and advantages of several damage identification techniques have been

studied by Talebinejad et al. (2011). Their findings demonstrated that only high intensity damage is detectable by these methods. Several damage detection methods have been also developed based on processing the vibration signals. In these methodologies, an index of damage is defined as the difference between undamaged (healthy) state and damage state of the structure. Fast Fourier Transform (FFT) based methods are among the most commonly used techniques to identify modal properties of the structure from ambient vibration data. Littler and Ellis (1995) deduced that FFT based methods can overestimate the modal damping. In addition, these methods are not sensitive to slight to moderate amount of damage in complex structures. Comprehensive literature study of several damage detection methods can be found in Farrar and Jaureguiz (1998) and Fan and Qiao (2011). Vibration based methods are not able to overcome all the problems in detecting various types of damages. An essential limitation of these methods is that the changes in modal properties such as natural frequency and modal damping caused by damage are usually very small. An et al. (2014) stated that vibration-based monitoring techniques are introduced to be powerful toolboxes in order to monitor the global dynamic characteristics and overall condition of bridge structures. However, Chang et al. (2003) and Lynch (2007) have concluded that these global techniques are often insensitive to local incipient damage, and they cannot be considered as reliable damage detection methods in order locate the local damages. To overcome such problem, An et al. (2014) listed few ongoing efforts to adapt local NDT methods for continuous bridge monitoring purposes such as guided wave techniques (Greve et al. 2005; Cawley and Alleyne 1996; Giurgiutiu 2008; Raghavan and Cesnik 2007, 2008; Rose 2002; Dalton et al. 2001). In a general definition, Zarafshan (2013)

has categorized these types of techniques into four main categories: a) Methods based on shift in natural frequency, b) Mode shape alteration based methods, c) Curvature or strain-shape based methods, and d) Methods based on the other modal parameters. Structural health monitoring methods based on global vibration response lack sufficient resolution for health monitoring of larger and more complex structures, especially for those with sophisticated geometries, multitudes of joints, elements, and boundaries (Jaishi and Ren 2005; Talebinejad et al. 2011). Even for smaller structures, i.e. short span bridges, these techniques have not been capable of detecting cracks and defects within various segments of the structure. Global structural health monitoring techniques are able to provide coarse evaluation of structural behavior, but they are not capable of providing detailed information.

1.5. Fiber Optic Sensing

The advent of optical fiber sensors provided opportunities for large scale monitoring of structures. Optical fibers are geometrically compatible with structural systems, capable of providing high resolution measurements, immune to electric and electromagnetic interferences, and can cover large sections of the structures (Ansari 2007; Bao et al. 2015; Meng and Ansari 2013; Nazarian et al. 2015a).

It was highlighted that fiber optic sensors are apparently expensive to be used in SHM while they have better approaches for conditions where the high rate of reliability is required. In the case of conditions where/when the lack of monitoring system could result in serious failure and catastrophic the price is not the selection criteria. In commercial applications when the fiber optic sensors are used in numerous locations they can even become cost effective. Application of optical sensors is sometimes the

only solution for performing a long term as well as reliable monitoring systems (Glisic and Inaudi 2007). With the rapid developments in the optical telecommunications market the expenses corresponding to the optical fibers and their associated optical components have dramatically reduced (Glisic and Inaudi 2007).

In Fig. 1.6, Glisic and Inaudi (2007) classified the fiber optic sensing technologies and Table 1.1 summarizes the main characteristics of these technologies. Since in the current thesis only the Fiber Bragg Grating (FBG) and Brillouin based distributed sensing were experimentally used, the details are discussed in the following. For the details regarding the rest of fiber optic sensors it is referred to Glisic and Inaudi (2007).
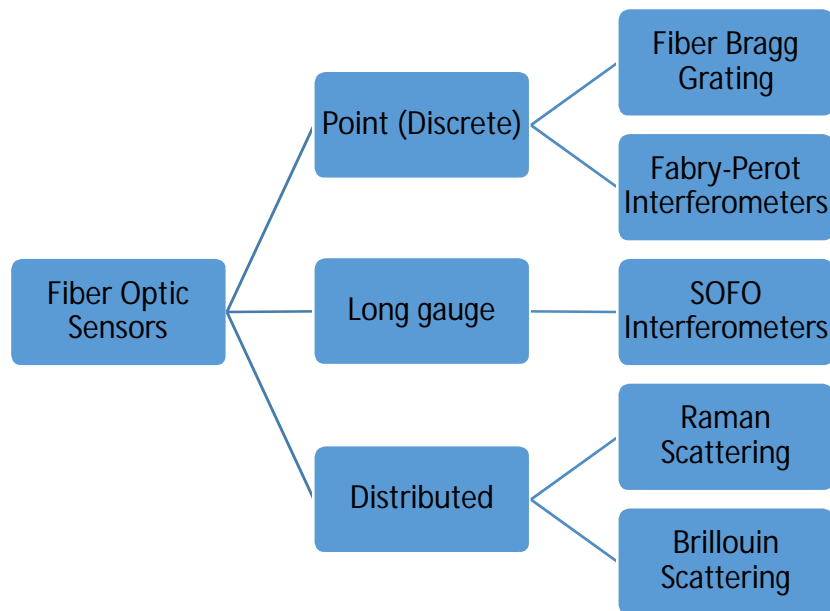
Figure 1.6 Classification of fiber optic sensors (Glisic and Inaudi 2007)

Table 1.1 Summary of fiber optic sensing types and typical performances (Glisic and Inaudi 2007)

		Point (Discrete Sensing)		Long gauge	Distributed Sensing	
		Fabry-Perot interferometric	**Fiber Bragg Grating**	**SOFO Interferometers**	**Raman Scattering**	**Brillouin Scattering**
Sensor Type		Point	Point	Long gauge (integral strain)	Distributed	Distributed
Measurable Parameters		Strain	Temperature	Deformation	Temperature	Temperature
		Temperature	Acceleration	Strain		Strain
		Pressure	Water Level	Tilt		
				Force		
Multiplexing		Parallel	In line and Parallel	Parallel	Distributed	Distributed
Measurement points in one line		1	10-50	1	10000	30000
Typical Accuracy	**Strain (με)**	1	1	1		20
	Deformation (μm)	100	1	1		
	Temperature (°C)	0.1	0.1		0.1	0.2
	Tilt (μrad)			30		
	Pressure (% full scale)	0.25				
Range				20 m gauge	8 km	30-150 km
Fiber Type		Multi Mode	Single Mode	Single Mode	Multi Mode	Single Mode

1.5.1. Discrete Sensing-FBG sensors

Discrete sensors have been widely employed in monitoring of structures (Glisic and Inaudi 2007). These sensors are built in two different shapes, namely Fiber Bragg Grating (FBG) and Fabry-Perot interferometric. FBG is the one achieving better performance, since it is capable of being multiplexing in one line of fiber optic line as well as higher strain resolution. The Bragg gratings are created by periodic alterations in the of refraction index of optical fiber's core. By adequately exposing the fiber to intense UV light these alteration can be produced. In the case of injecting a tunable light through an optical fiber with grating, all the wavelength levels will pass throughout the fiber except the one matching with the grating pitch specific wavelength. Therefore, based on the wavelength variation of the reflected light it is possible to measure the

induced temperature and/or strain along the fiber (Glisic and Inaudi 2007). A spectrometer or a tunable laser with wavelength filter (e.g. Fabry–Perot cavity) has been implemented for measurement. To separate the strain and temperature values from the measurements, a free fiber is used to calculate the sole effects of temperature and then, it will be used for temperature compensation as well as obtain the strain values. The other main interest with FBG is its capability in multiplexing potential. This capability enables to measure the strain at multiple sections along the optical fiber, as shown in Fig. 1.7. Typically, 4–16 grating sensors can be installed along a single line of an optical fiber (Glisic and Inaudi 2007).
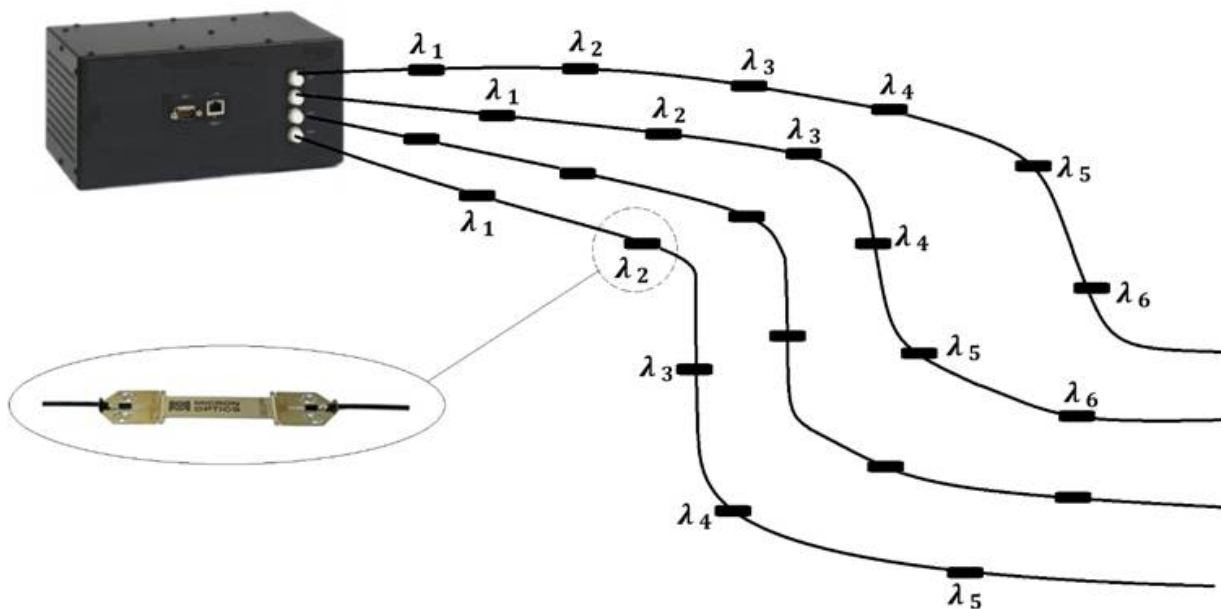
Figure 1.7 Parallel and in-line multiplexing of FBG sensors

1.5.2. Distributed Sensing- Brillouin scattering

Discrete sensors, such as FBGs, have been widely employed in monitoring of structures due to high measurement resolutions, and capability for serial multiplexing (Chen et al. 2000; Bao et al. 2015). Localized sensor based methods of detection of cracks in

structural materials reveal several significant short comings. Discrete sensors either electrical resistance type strain gages, vibrating wire, or fiber optics, i.e. FBG or Fabry Perot require use of multitudes of sensors even in a small to medium sized structures, multi-channel data acquisition systems and installation of many lead-lines to access the sensors. Bandwidth limitations and the dynamic range requirements in civil structures do not allow for more than a few sensors to be connected in one line and to address the measurement issues. Point sensing only yields information for its specific location and requires many points (locations) along the structure. Additionally, discrete or point sensors in structural monitoring require an added level of networking complexity to coordinate the location of perturbations.

Latest technological developments in distributed sensing with optical fibers will have transformative effects on various aspects of structural health monitoring (Meng et al. 2015; Nazarian et al. 2015b). Distributed sensing provides opportunities for development of innovative approaches in civil structures as it enables the monitoring units to acquire all the information associated within the entire structures' lengths using only a single line of an optical fiber (Liu et al. 2015). It will do away with the need to install multitude of sensors, lead lines, as well as multi-channel data ports with direct impact on labor, cost and ease of use (Fig. 1.8). Distributed sensing measures strain and or temperature along the entire length of the optical fiber with measurement range capabilities of more than 30 kilometers. The spatial resolution of these sensors varies depending on the interrogation technology type and generally between 2 cm to one meter with strain resolution capabilities of 5 to 15 micro strains. Examples of recent applications include monitoring of main girder strains of bridges (Zhang and Ansari

2006), multiple cracks in steel beams (Glisic and Inaudi 2011; Motamedi et al. 2012; Feng et al. 2013); crack detection in fiber reinforced concrete (Imai et al. 2010); monitoring ground displacement, and in geotechnical and tunneling applications (Shi et al. 2003; Klar et al. 2014; Mair 2008), monitoring of gas and oil pipelines (Yan and Chyan 2010).
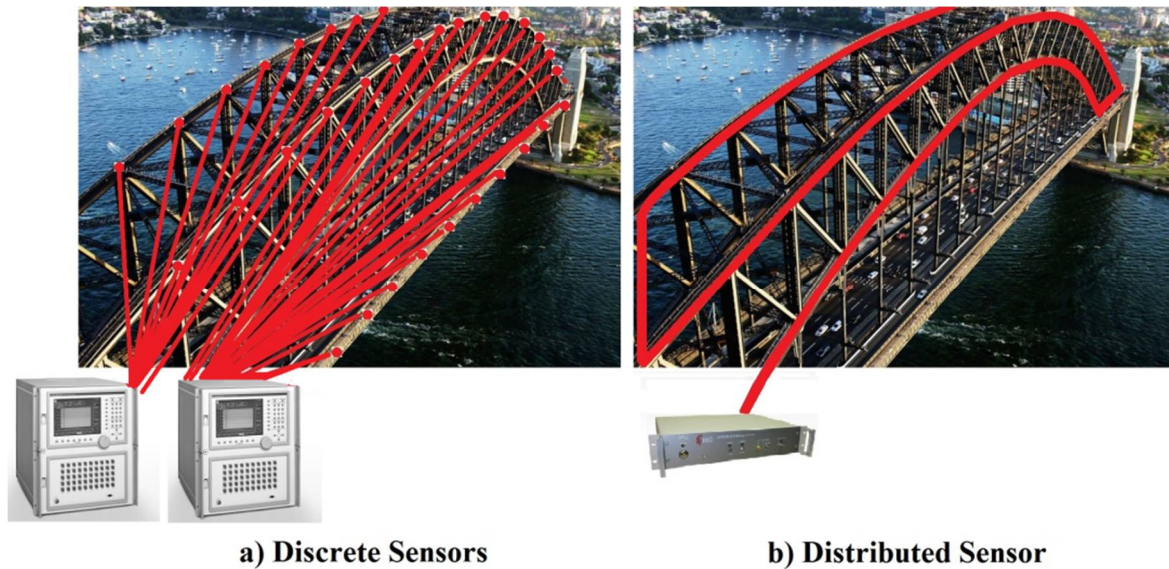
Figure 1.8 Distributed sensor in (b) is contrasted against the arrays of discrete sensors in (a) photo credits (www.abc.net.au)

The distributed fiber optic-based sensors are created by different scattering phenomena such as Rayleigh, Raman and Brillouin. Brillouin sensors are the ones achieving better performance, since they are capable of measuring over 100-km long fibers at near meter spatial resolutions (Zornoza 2014; Bao 2009). Brillouin scattering phenomenon is induced when the injected light within the optical fiber interacts with the time-dependent density variations of the optical fiber's core causing a shift in the frequency domain of injected light (Motamedi et al. 2012). The Brillouin frequency shift (BFS) in single mode optical fiber is proportional to strain and temperature variations, and therefore, it is used in distributed strain and temperature monitoring. Brillouin Optical Time Domain Analysis

(BOTDA), Brillouin Optical Frequency domain analysis (BOFDA), Brillouin Optical Time Domain Reflectometry (BOTDR), and Brillouin optical correlation domain analysis (BOCDA) are methods developed on the basis of Brillouin scattering. In BOFDA, the spectral characterization of the fiber is obtained (Garus 1996). In BOCDA, the correlation of pump and probe waves in each location of the fiber is used (Hotate 2000). In BOTDR, the spontaneous Brillouin scattering is characterized along the fiber (Horiguchi 1995). In BOTDA, the convolution of pump and probe waves in each location of the fiber is used (Diaz et al. 2008). It was concluded that BOTDA simultaneously could produce stronger signals with smaller range of spatial resolutions as well as wider distances compared with the rest of techniques (Guo et al. 2009). BOTDA sensing is one of the most popular Brillouin based sensors which was commercialized and numerously applied in the area of SHM (e.g. Neubrex Co. Ltd). The spatial resolution (SR) of the BOTDA system depends on the duration of the pump signal. In order to stimulate enough phonons for measurements, the duration of the pump signal needs to be 10 nano-seconds (ns) or more, which limits the SR of the BOTDA to one meter (Bao and Chen 2011). It is shown that SR of one meter is not sufficient for detection of crack locations directly (Feng et al. 2013) and other post processing signal analysis techniques such as wavelet transform (Feng et al. 2014) or multiple peak fittings (Ravet et al. 2000) are necessary to enhance the signals. Recently, different types of BOTDA techniques have also been developed to address the existing issues. Pre-Pump-Pulse-BOTDA (PPP-BOTDA) (Kishida 2005a), Leakage-BOTDA (Bao 1999; Kalosha 2006), Dark Pulse-BOTDA (Brown 2007), Double Pulse-BOTDA (Bao et al. 2004; Li et al. 2008), and Phase Shift-BOTDA (Foaleng 2010) have focused in order to improve the

SR level of BOTDA. In addition, Raman Distributed Amplification-BOTDA (Angulo 2012), Simplex Coded-BOTDA (Taki 2013), and Self heterodyne-BOTDA (Zornoza 2012) have also tried to extend the measurement distances. With the advent of new BOTDA based techniques, such as PPP-BOTDA, it is then possible to achieve centimeter level SR useful for over 1 km length monitoring (Kishida et al. 2009). In prevalent BOTDA-based techniques (e.g. PPP-BOTDA), one of the counter-propagating waves is swept in frequency domain to find the target frequency with maximum energy mediation (Voskoboinik et al. 2011a). As mentioned, this frequency is called BFS. Fig. 1.9a represents the final constructed Brillouin gain spectra (BGS) shape form BOTDA measurements. It is clear that the maximum BFS changed for some particular locations of the instrumented structure is indicating the corresponding strain or temperature has changed over those specific locations. Once the maximum BFS for each individual sensing points of fiber has been located, the associated BFS is recorded as the Brillouin scattering central frequency denoted by ν_B. Fig. 1.9b represents the schematic view of BOTDA device. The relationship between the Brillouin scattering frequency shifts, measured by BOTDA sensing device, with strain or temperature being considered linear, expressed as (Bao et al. 2001, 1996):

$$\nu_B(T, \varepsilon) = C_\varepsilon(\varepsilon - \varepsilon_0) + C_T(T - T_0) + \nu_{B0}(T_0, \varepsilon_0) \tag{Eq. 1}$$
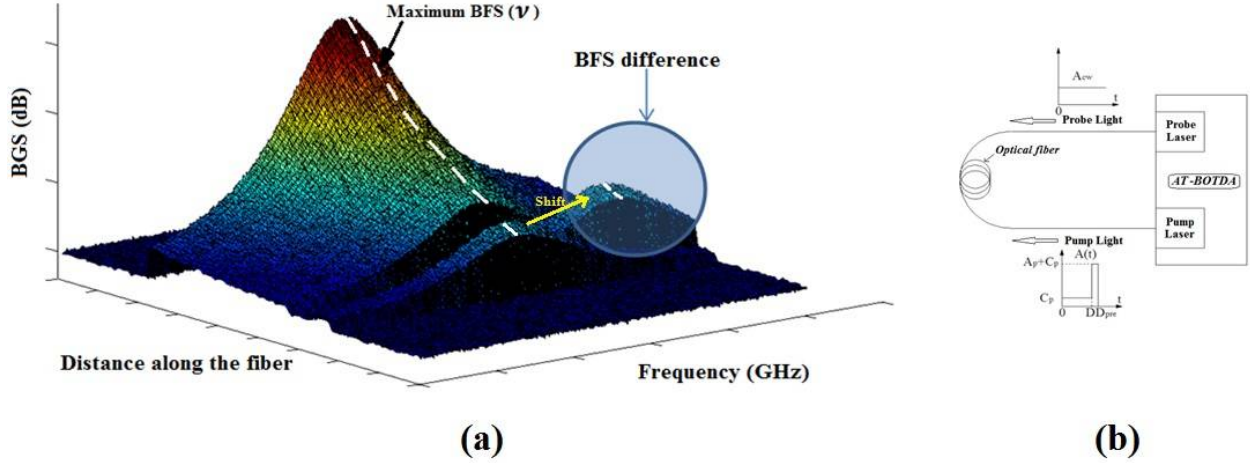
Figure 1.9 a) Reconstruction of the spectra along the fiber after the sweep, b) Schematic representation of AT-BOTDA (Zornoza 2014)

where T and ε respectively denote the temperature and strain at different sections along the optical fiber averaged over the SR. C_T and C_ε are the temperature and strain coefficients, respectively, and determined by calibration. T_0 and ε_0 are the strain and temperature, respectively, corresponding to the reference Brillouin frequency, ν_{B0} (Brown et al. 2005). However, all the above mentioned BOTDA-based methods still need over minute time period in order to conduct the measurements. For a fiber length of 100 m, it usually takes 5-10 minutes to complete the test with higher levels of accuracy and repeatability. As pinpointed by Voskoboinik et al. (2011a), running consecutive frequency sweeps for acquiring the BGS map as well as locating its maximum may potentially limit the ability to resolve fast, dynamic changes in the BFS distribution. This makes the monitored structure has to be statically loaded and remained constant during the measurement process, which is practically impossible for dynamically exposed structures.

To overcome such problem, there are ongoing efforts to develop techniques to perform dynamic measurements with higher sampling rate (Zornoza 2014; Bernini et al. 2009;

Cui et al. 2011; Peled et al. 2011; Chaube et al. 2008; Voskoboinik et al. 2011a; Voskoboinik et al. 2011b). Recently, Li et al. (2010) has invented and patented a new BOTDA technique (called Amplitude Transfer (AT) BOTDA) which is capable to be used in dynamic conditions. They derived technique in which measuring the single frequency will be sufficient to estimate the central frequency, v, decreasing the measurement time to the order of 10 ms. In other words, instead of using swept frequency, it uses a pump pulse and a probe wave at fixed optical frequency individually. AT mode, based on Brillouin variation at a fixed swept frequency, was adapted to scan the frequency shift. This method relies on the two assumptions, namely, that the shape of BGS spectrum does not substantially change while strain is induced, and those measurements need to hold the receiver level (i.e. BGS level). The first assumption enforces limit that strain change must be relatively small, corresponding up to 6 dB value, while the second is essential for center frequency estimation procedure (Li et al. 2010). Using the AT-BOTDA technique, they were able to measure 100 m of sensing fiber length with the spatial resolution of 20 cm (or even less) with over 1 KHz rate of sampling. Fig. 1.10 represents the Neubrescope (NBX#6055) device recently developed by Neubrex Company for dynamic BOTDA measurements.
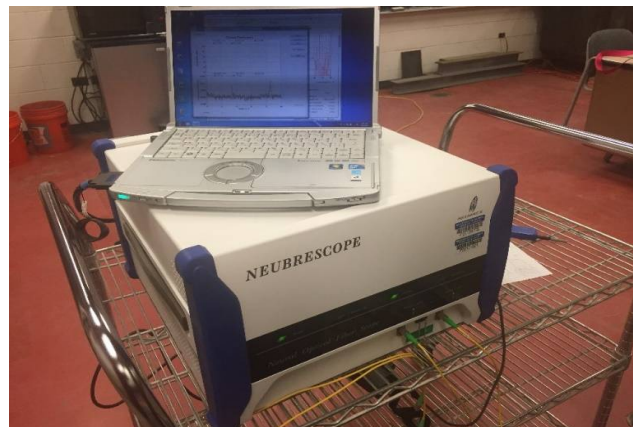
Figure 1.10 Neubrescope device (NBX#6055)

1.6. Research Outlines

In the current thesis, it is attempted to focus on analyzing both of the action and reaction characteristics of bridges in order to provide a comprehensive SHM package for their in-service monitoring. To do so, the thesis has been divided into two main phases. In the first phase, a new concept of Weigh in Motion technique has been proposed in order to specify the actions subjecting the bridge. The developed Bridge WIM (BWIM) is based on the measurement of the shear strain of an instrumented bridge to estimate the attributes of passing traffic (González et al. 2008). In other words, the proposed BWIM provides the axle loads of moving vehicles as well as calculates vehicle information such as vehicle class, velocity, and axle spacing. All these information could be efficiently used for design and assessment, statistical, transportation, commercial, and weight enforcement purposes. Chapter 2 addresses the developed methodology as well as the experimental program details and then focuses on the analysis of the results.

In the second phase of thesis, it is focused on observing the behavior of a structure (reaction) mainly by distributed strain monitoring of the structure. For this aim, distributed sensing is used to monitor the strain profile in the structures subjected to vibration loading. The proposed methodology is reference free and locates the defects as small as 50 microns along the structures' surfaces. Chapter 3 addresses the developed methodology as well as the experimental program details and then focuses on the analysis of the results. Further in the thesis, a defect quantification method is also developed in order to magnify the level of detected defects. The main objective pertains to the accurate quantification of local defects sizes based on distributed monitoring of strains in large structural systems. A theoretical model is investigated to

analysis the strain transfer mechanism from the structure surface to the distributed optical fiber components in the presence of local defects. The theoretical formulation simulated the strain distribution within the components of an optical fiber crossing over a single crack opening. The proposed model was formulated in a manner to quantify defects in the presence of structural vibration. Chapter 4 addresses the developed methodology as well as the experimental program details.

Finally, in Chapter 5, the results and discussions have been summarized and new ideas have been introduced for new routes of future research efforts.

Chapter II: Generalized Formulation for Shear Strain Based Bridge Weigh in Motion

The materials of current chapter are partially derived from my published paper with the following citation: "Generalized Method and Monitoring Technique for Shear Strain Based Bridge Weigh in Motion" by Bao, T., Babanajad, S.K., Taylor, T., and Ansari, F., Journal of Bridge Engineering, ASCE, 04015029, 2015, 1-13
Please refer to the authors' contributions in page iv in the beginning of this document for details of contributions.

2.1. Introduction

The objective for the work in presented chapter was to develop an alternative BWIM approach for accurate estimation of axle weights, axle spacing, and gross weights of the trucks as they travel over the bridges. The details regarding the different types of WIM as well as BWIM systems and their advantages/disadvantages were already discussed in the Chapter 1 in more details. The proposed technique is based on the measurement of shear strains near the bridge abutments, which is different from the traditional flexural strain based systems. The measurements are achieved by use of shear strain rosettes sensors on the girder webs. In doing so, the trucks' axle weights could be acquired at the bridge abutments, where due to the immediacy of the force path to the bridge supports, the effects of traffic configurations as well as bridge structural parameters on the measurements are dramatically reduced. As demonstrated by the typical shear and moment influence lines in Fig. 2.1, in contrast to flexural response, the shear influence line is discontinuous at the location of the load. Since the flexural strains embody the combined effects of all axles on the bridge, no strain reversals are observed in the moment influence line. Truck axles produce pronounced peaks in the shear strain response of the bridges, which in turn are used for detection of axles, measurement of axle weights, axle spacing, and truck speeds. Because of the sharp peaks in shear

strain response, the method is less susceptible to dynamic effects. The shear force based method for BWIM was previously introduced for application in statically determinate bridges (Helmi et. al 2014). The approach in the previous study relied on the linearity of the shear influence lines in statically determinate structures and could not accommodate the more complex cases involving statically indeterminate structures. The present approach is generalized for application in both statically determinate as well as indeterminate bridges. The method is introduced next followed by validation of the methodology based on the results from calibrated truck tests on three different types of bridges.
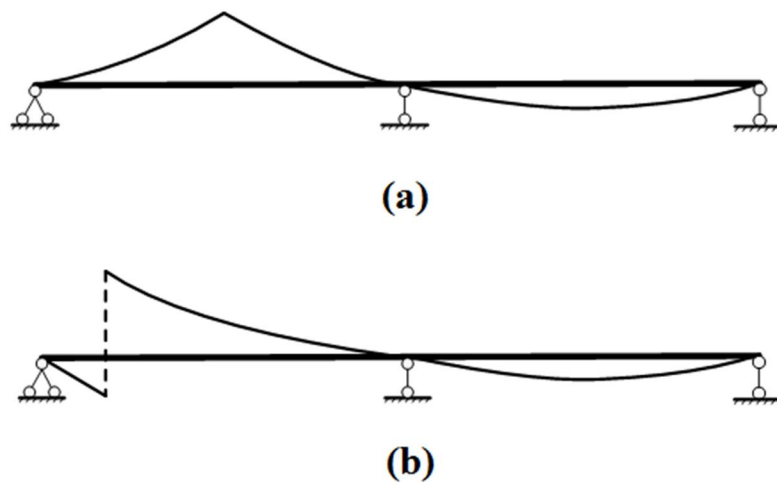
Figure 2.1 Schematic diagram of influence lines: (a) bending moment influence line; (b) shear force influence line

2.2. Methodology

As known, the shear strain cannot be directly measured using a single strain gauges. Therefore, shear strain rosettes were previously developed in order to measure the corresponding shear strain within different structural elements (Dally and Riley 1991; Helmi et al. 2014). Implementation of the method involves use of two sets of strain

rosette sensors for acquisition of truck speed, axle spacings and shear strain response of the bridge. Strain rosettes are effective in discerning the state of strain at a point by use of two or more strain gauges (Gere and Timoshenko 1990). Generalized Mohr circle transformation equations were expanded for the determination of strains in any arbitrary directions using principal strains. A two-strain-gauge rosette was employed in this study for monitoring the shear strain. The strain rosette was arranged in an inverted delta configuration as shown in Fig. 2.2. Generalized strain transformation equations (Eq. 3 and Eq. 4) are then employed for the determination of strains along any directions.

$$\varepsilon_1 = \varepsilon_x.\cos^2\theta + \varepsilon_y.\sin^2\theta + \gamma_{xy}.\sin\theta.\cos\theta \qquad \text{(Eq. 1)}$$

$$\varepsilon_2 = \varepsilon_x.\cos^2\theta + \varepsilon_y.\sin^2\theta - \gamma_{xy}.\sin\theta.\cos\theta \qquad \text{(Eq. 2)}$$

Subtracting Eq. 2 from Eq. 1 results in:

$$\gamma_{xy} = \frac{\varepsilon_1-\varepsilon_2}{2\sin\theta\cos\theta} \qquad \text{(Eq. 3)}$$
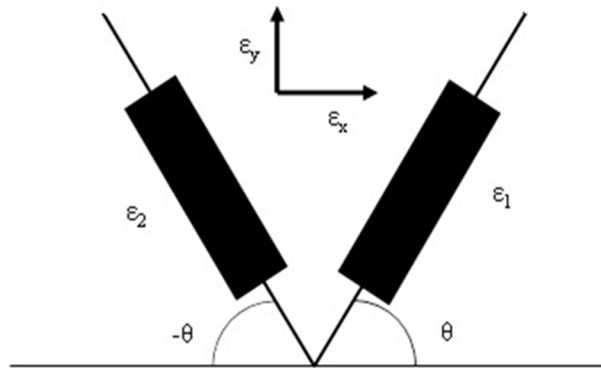
Figure 2.2 Shear strain rosette

In this case, the shear strain, γ_{xy} is obtained from the strain gauges, ε_1, and ε_2 in the rosette oriented at an angle of θ with respect to the horizontal. Since the calculations include the subtraction of two strains at the same location any shifts that occur due to

temperature change cancel each other, and therefore, the strain rosette is self temperature compensating (Helmi et al. 2014).

The shear stress-strain relationship is used for conversion of measured strains to stresses from which shear force response of the bridge is computed. For linear systems, the effect of truck axle weights on the shear force response follows the superposition principle. The superposition principle is employed in order to relate the measured shear response of the bridge to the summation of truck axle weights by using the influence line of the bridge:

$$\gamma = \sum_{i=1}^{n} P_i . IL_{(x)} \tag{Eq. 4}$$

$$GVW = \sum_{i=1}^{n} P_i \tag{Eq. 5}$$

Where, γ is shear strain, P_i are axle loads, n is total number of truck axles, and $IL_{(x)}$ is the shear strain influence line. Solution to the system of equations that is formed by using the superposition principle for truck axles crossing over the strain rosettes yields the axle weights from which GVW is computed.

The stress strain relationship is used for the computation of shear stress, τ :

$$\tau = G\gamma \tag{Eq. 6}$$

Where, τ is the shear stress, and G is the shear modulus. Shear force V is computed from the relationship between shear force and shear stress:

$$\tau = \frac{QV}{It} \tag{Eq. 7}$$

Where, I is the moment of inertia of the cross section, t is the girder thickness (at rosette level), and Q is the first moment of the cross-sectional area above the section at

which shear is being computed (rosette level). Shear is maximum at the neutral axis, and higher resolution measurements are achieved when the shear rosettes are installed at the neutral axis level. For the slab on girder composite type bridges, the cross section is a T-section with neutral axis very close to the flange. For the concrete box girder type bridges, it is above the centerline of the cross section varying according to the sizes of upper and lower flanges of the box. Prior to finalizing installation of the sensor systems, a series of rosette gauges along the depth of cross section were employed in order to verify the location of computed neutral axis. Fig. 2.3 demonstrates a schematic view of concrete box girder as well as slab on girder composite type bridges instrumented by three rosette sensors along three levels of each flange. The results indicated that the shear strain is maximum at the location of R2 and R4 sensors corresponding to the location of neutral axis. By combining Equations (6) and (7), the shear force can be estimated in terms of the measured shear strain:

$$V = \frac{GIt}{Q}\gamma \qquad\qquad (Eq. 8)$$

Since Q, I, t, and G are only related to the geometric characteristics of the section and the material properties of the bridge, shear force can be re-written in the following form:

$$V = \alpha\gamma \qquad\qquad (Eq. 9)$$

Where, $\alpha = \frac{GIt}{Q}$ and is a constant signifying the proportionality of the shear force and the measured shear strain.
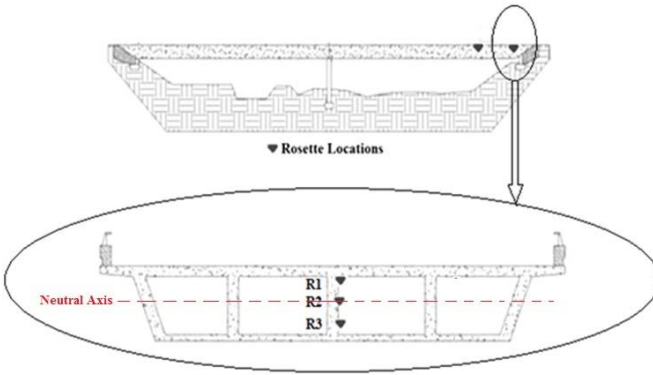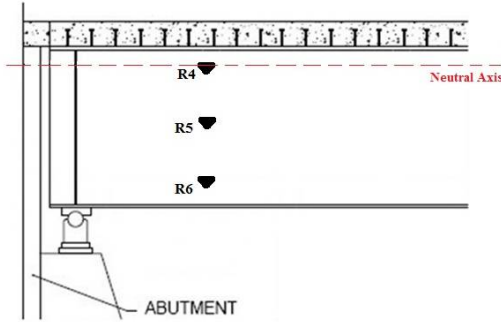
Figure 2.3 Typical rosette sensor arrangements along the flange depth: a) concrete box girder (schematic view), b) concrete box girder (actual instrumentation), c) slab on steel girder composite (schematic view), and d) slab on steel girder composite (actual instrumentation)

2.2.2. Axle Spacing, Axle Loads, and GVW

Fig. 2.4 pertains to the general case of a truck crossing over a bridge with shear strain rosettes B and A installed near the abutment at the exit end of the bridge. The truck has n axles with axle weights and spacings represented by $P_1, P_2, \dots, P_n$ and $L_1, L_2, \dots, L_{n-1}$, respectively. Shown in the inset of Fig. 2.4a are two series of shear strain response

data acquired by rosette sets B and A as the individual truck axles cross over them. First, let's consider the case where the first axle of the truck is at a general distance x away from the abutment. In this case, shear force can be expressed by the following equation:

$$V_{(x)} = P_1 IL'_{(x)} + P_2 IL'_{(x+L_1)} + , \dots , + P_n IL'_{(x+L_1+L_2+,\dots,+L_{n-1})} \tag{Eq. 10}$$

Where, $IL'_{(x)}$ is the influence line for the shear force, and by using Eq. (7), influence line for shear strain, $IL_{(x)}$ can be expressed in terms of $IL'_{(x)}$, and therefore Eq. (9) is converted to:

$$IL'_{(x)} = \alpha . IL_{(x)} \tag{Eq. 11}$$

and $$\gamma_{(x)} = P_1 IL_{(x)} + P_2 IL_{(x+L_1)} + , \dots , + P_n IL_{(x+L_1+L_2+,\dots,+L_{n-1})} \tag{Eq. 12}$$

The truck axles reach rosette B first, and then rosette A for which their times of arrivals are denoted by $t_{B1}, t_{B2},\dots, t_{Bn}$ and $t_{A1}, t_{A2},\dots, t_{An}$, respectively.

(a) General View
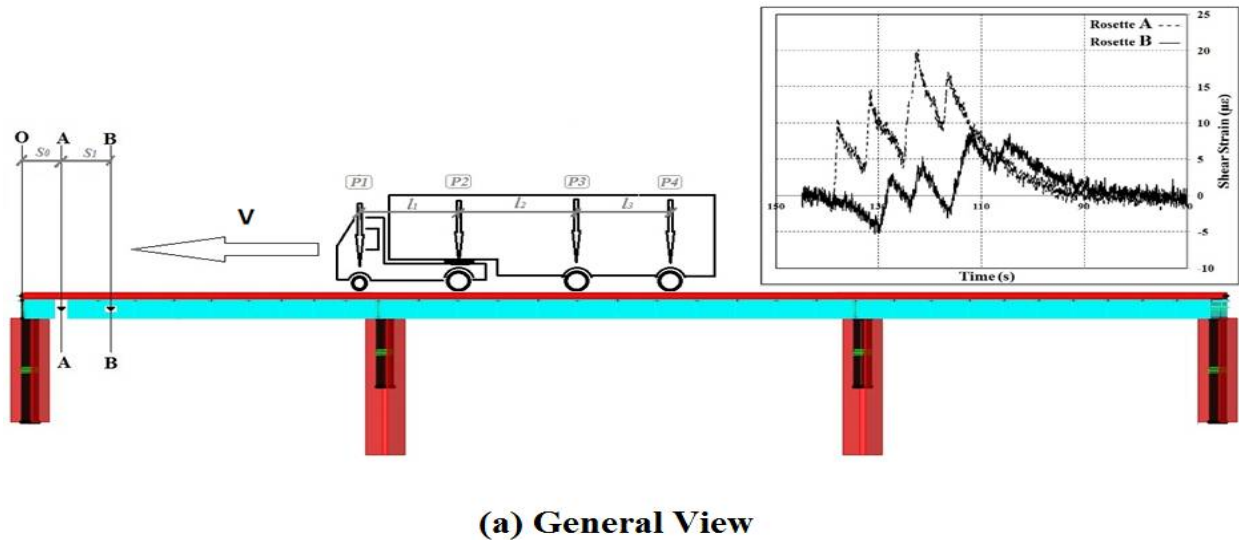
Figure 2.4 Truck location and measured shear strains *(to be continued)*
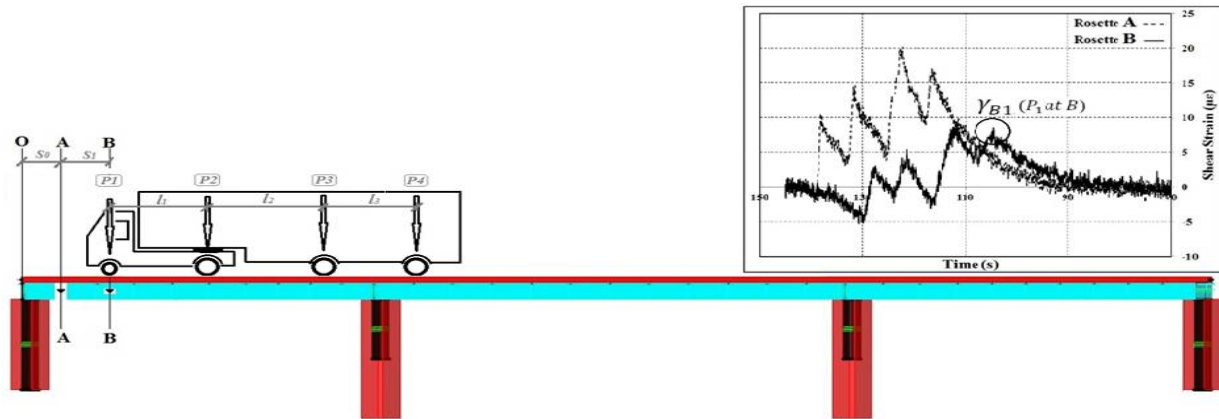
(b) t = t$_{B1}$
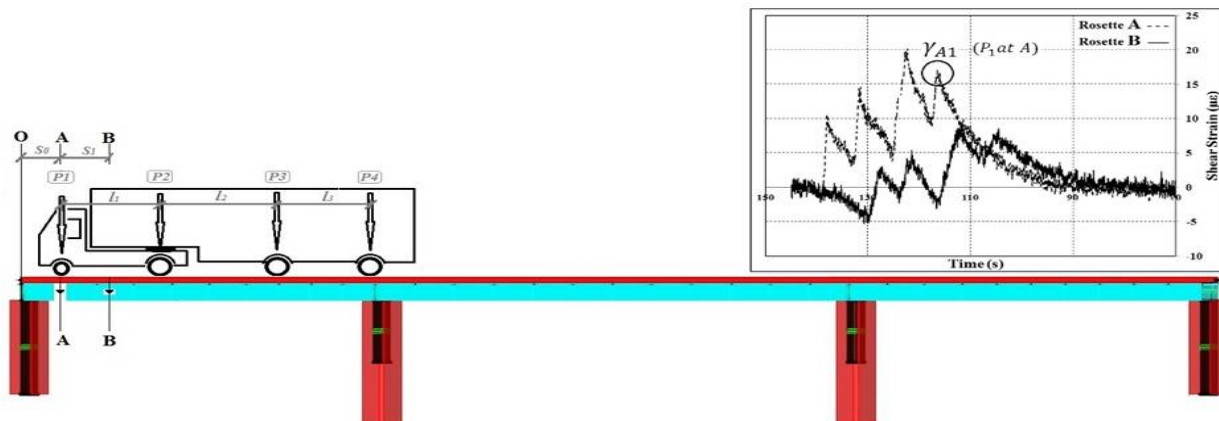
(c) t = t$_{A1}$
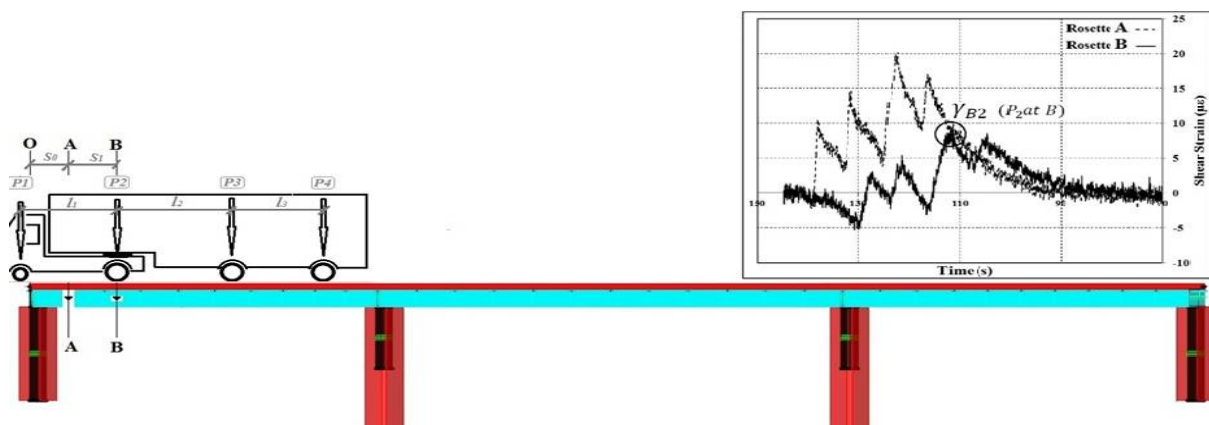
(d) t = t$_{B2}$

Figure 2.4 Truck location and measured shear strains *(to be continued)*
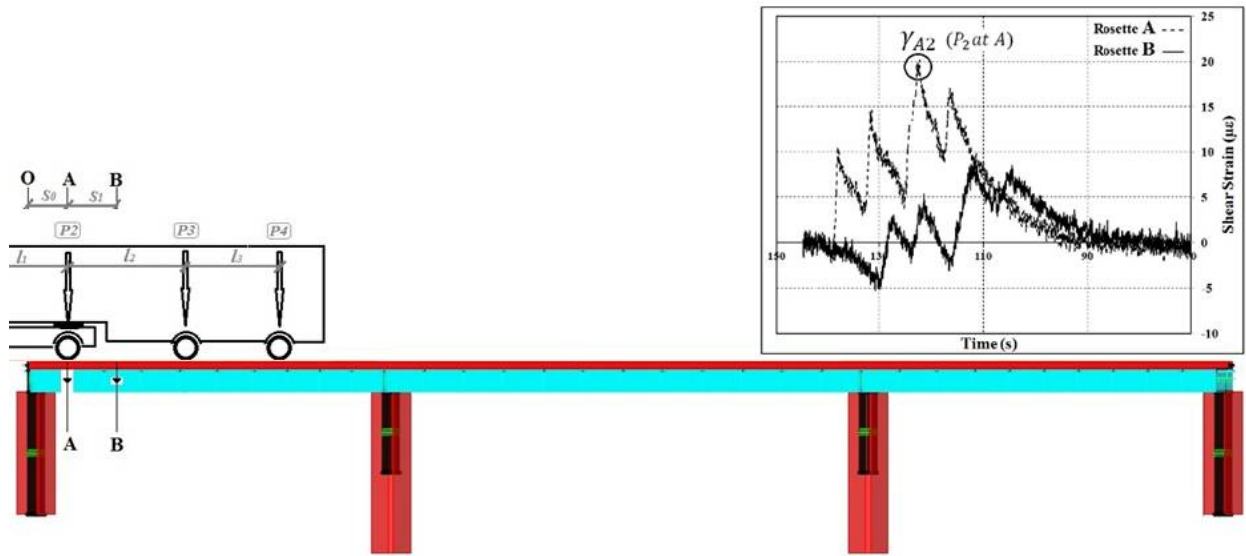
(e) t = t_{A2}
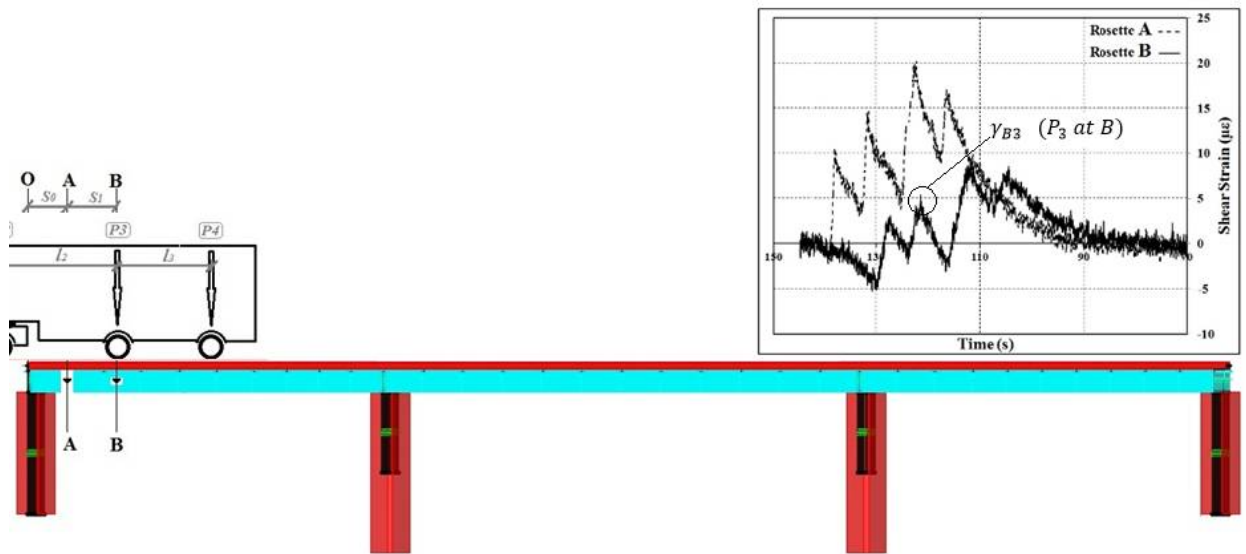
(f) t = t_{B3}

Figure 2.4 Truck location and measured shear strains *(to be continued)*

38
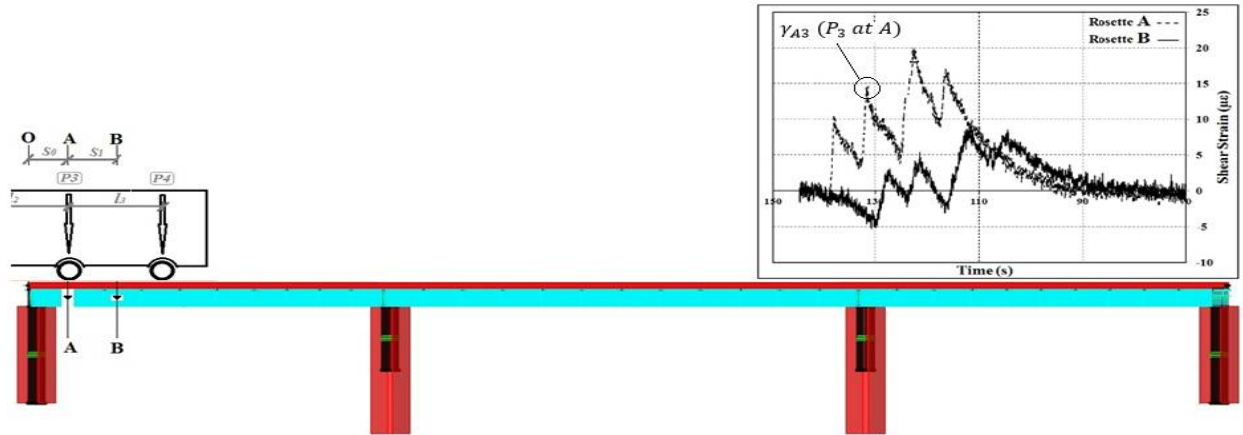
(g) t = t$_{A3}$
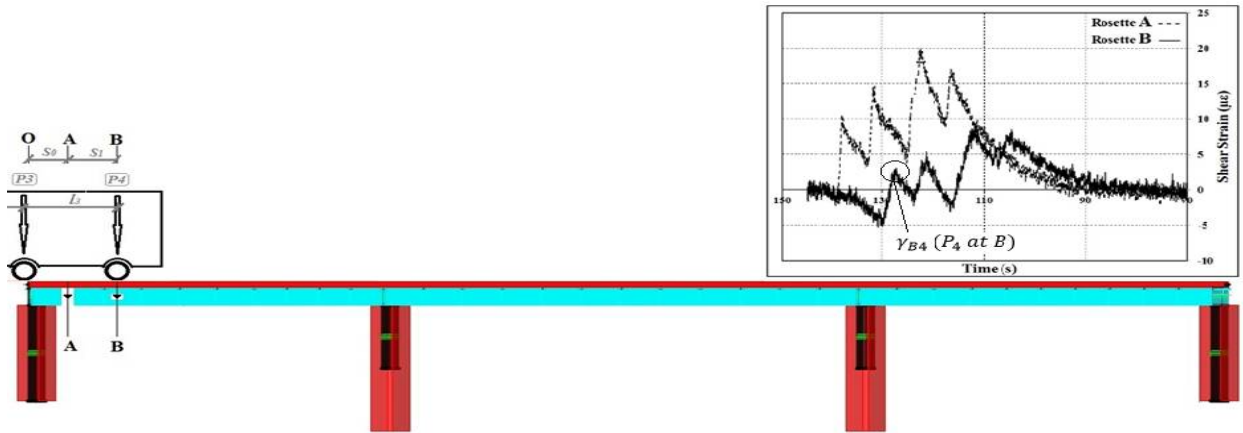
(h) t = t$_{B4}$
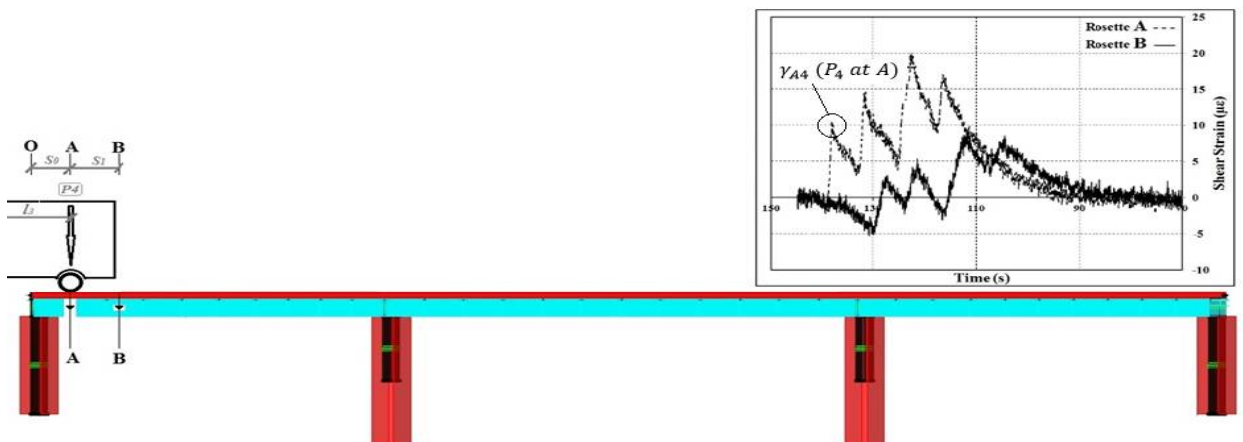
(i) t = t$_{A4}$.

Figure 2.4 Truck location and measured shear strains

Therefore, at time $t = t_{B1}$, shear strain is expressed by the following equation(Fig. 2.4b):

$$\gamma_{B1} = P_1 IL_{(S_0+S_1)} + P_2 IL_{(S_0+S_1+L_1)} +, \dots, +P_n IL_{(S_0+S_1+L_1+L_2+,\dots,+L_{n-1})} \qquad \text{(Eq. 13)}$$

Where, S_0 is the distance of rosette A to the abutment, and S_1 is the distance between rosettes A and B. At $t = t_{A1}$, the first axle is on rosette A, and shear strain response can be expressed by (Fig.3c):

$$\gamma_{A1} = P_1 IL_{(S_0)} + P_2 IL_{(S_0+L_1)} +, \dots, +P_n IL_{(S_0+L_1+L_2+,\dots,+L_{n-1})} \qquad \text{(Eq. 14)}$$

The time difference for the first axle passing over rosettes B and A is:

$$\Delta t_1 = t_{A1} - t_{B1} \qquad \text{(Eq. 15)}$$

Then, the truck speed during this time interval can be estimated as:

$$v_1 = S_1/\Delta t_1 \qquad \text{(Eq. 16)}$$

This process is repeated for all the axles crossing over rosettes B and A. For instance, at $t = t_{B2}$, and as shown in Fig. 2.4d, the shear strain is expressed by:

$$\gamma_{B2} = P_2 IL_{(S_0+S_1)} +, \dots, +P_n IL_{(S_0+S_1+L_2+,\dots,+L_{n-1})} \qquad \text{(Eq. 17)}$$

At $t = t_{A2}$, and as shown in Fig. 2.4e, shear strain is expressed by:

$$\gamma_{A2} = P_2 IL_{(S_0)} +, \dots, +P_n IL_{(S_0+L_2+,\dots,+L_{n-1})} \qquad \text{(Eq. 18)}$$

The spacing between the first and second axles is estimated as:

$$L_1 = v_1(t_{A2} - t_{A1}) \quad \text{or} \quad L_1 = v_1(t_{B2} - t_{B1}) \qquad \text{(Eq. 19)}$$

Similarly for the third axle (see Fig. 2.4f and Fig. 2.4g):

$$\gamma_{B3} = P_3 IL_{(S_0+S_1)} +, \dots, +P_n IL_{(S_0+S_1+L_3,\dots,+L_{n-1})} \qquad \text{(Eq. 20)}$$

$$\gamma_{A3} = P_3 IL_{(S_0)} +, \dots, +P_n IL_{(S_0+L_3+,\dots,+L_{n-1})} \qquad \text{(Eq. 21)}$$

$$\Delta t_2 = t_{A2} - t_{B2} \qquad \text{(Eq. 22)}$$

$$v_2 = S_1/\Delta t_2 \qquad \text{(Eq. 23)}$$

$$L_2 = v_2(t_{A3} - t_{A2}) \text{ or } L_2 = v_2(t_{B3} - t_{B2}) \qquad \text{(Eq. 24)}$$

and continuing to the last axles (see Fig. 2.4h and Fig. 2.4i):

$$\gamma_{B(n-1)} = P_{n-1}IL_{(S_0+S_1)} + P_nIL_{(S_0+S_1+L_{n-1})} \tag{Eq. 25}$$

$$\gamma_{A(n-1)} = P_{n-1}IL_{(S_0)} + P_nIL_{(S_0+L_{n-1})} \tag{Eq. 26}$$

$$\Delta t_{n-1} = t_{A(n-1)} - t_{B(n-1)} \tag{Eq. 27}$$

$$v_{n-1} = \frac{S_1}{\Delta t_{n-1}} \tag{Eq. 28}$$

$$L_{n-1} = v_{n-1}(t_{An} - t_{A(n-1)}) \text{ or } L_{n-1} = v_{n-1}\left(t_{Bn} - t_{B(n-1)}\right) \tag{Eq. 29}$$

$$\gamma_{Bn} = P_nIL_{(S_0+S_1)} \tag{Eq. 30}$$

$$\gamma_{An} = P_nIL_{(S_0)} \tag{Eq. 31}$$

It is then possible to form two systems of equations either based on the shear strain response data of rosette B corresponding to Eqs. (13), (17), (20), (25), and (30), or rosette set A pertaining to Eqs. (14), (18), (21), (26), and (31). Only one set is needed for the computation of axle weights. Since shear strains are larger near the supports, they yield higher resolution measurements, and therefore are preferred for use in the computations. In this case data from rosette set A is the preferred set and employed in forming the systems of equations. After calibration of α value the procedure for computing the GVW involves: (a) Detection of axle peaks from shear strain rosette data; (b) Computation of intra-axle time intervals, Δt_1, Δt_2,..., Δt_{n-1}; (c) Estimation of intra-axle speeds, v_1, v_2, ..., v_{n-1}; (d) Determination of axle spacings, L_1, L_2, ..., L_{n-1}; (e) Solving for the axle weights by using the system of strain-load equations (Eq. (32)): the axle weights are estimated in reverse order. First, Eq. (31) is used to calculate P_n, then Eq. (26) and calculated P_n are used to obtain P_{n-1}, and continuing to the last axles, P_{n-2},

P_{n-3}, ..., P_3, P_2, P_1 are obtained successively; and (e) Computation of the GVW by summing the axle weights (i.e., $GVW = \sum_{i=1}^{n} P_i$).

$$
\left\{
\begin{aligned}
\gamma_{An} &= P_n IL(S_0) \\
\gamma_{A(n-1)} &= P_{n-1} IL(S_0) + P_n IL(S_0 + L_{n-1}) \\
\gamma_{A(n-2)} &= P_{n-2} IL(S_0) + P_{n-1} IL(S_0 + L_{n-2}) + P_n IL(S_0 + L_{n-2} + L_{n-1}) \\
&\dots \qquad\qquad\qquad\qquad \dots \\
\gamma_{A2} &= P_2 IL(S_0) +, \dots, + P_n IL(S_0 + L_2 +, \dots, + L_{n-2} + L_{n-1}) \\
\gamma_{A1} &= P_1 IL(S_0) + P_2 IL(S_0 + L_1) +, \dots, + P_n IL(S_0 + L_1 + L_2 +, \dots, + L_{n-2} + L_{n-1})
\end{aligned}
\right. \qquad (Eq.\,32)
$$

2.2.3. Shear Strain Influence Line

Shear strain influence line is the function defining the response of the shear strain to the axle loads. It can be obtained by determining the shear force influence line ($IL'_{(x)}$ shown in Fig. 2.5) from either classical mechanics or finite elements analysis of the bridge, and computation of α from the geometric and materials properties of bridge. Then, the shear strain influence line is obtained by using the relationship between the shear force and shear strain, i.e. Eq. (11). Accuracy of results will be dependent on the accurate determination of α. Although α can be determined from the geometric and material properties of the bridge, a more realistic approach is to compute α during the calibration process at the bridge site. This assures that α portrays changes in the materials properties and geometrical characteristics as well as composite action of the girder in the bridge. During the calibration process, known axle weights of the calibrated trucks, shear force influence line and the response of the shear rosette sensor to the axle weights is employed in order to obtain α. Once α is computed during the calibration process, the shear strain influence line, $IL_{(x)}$ can be determined from Eq. (11).
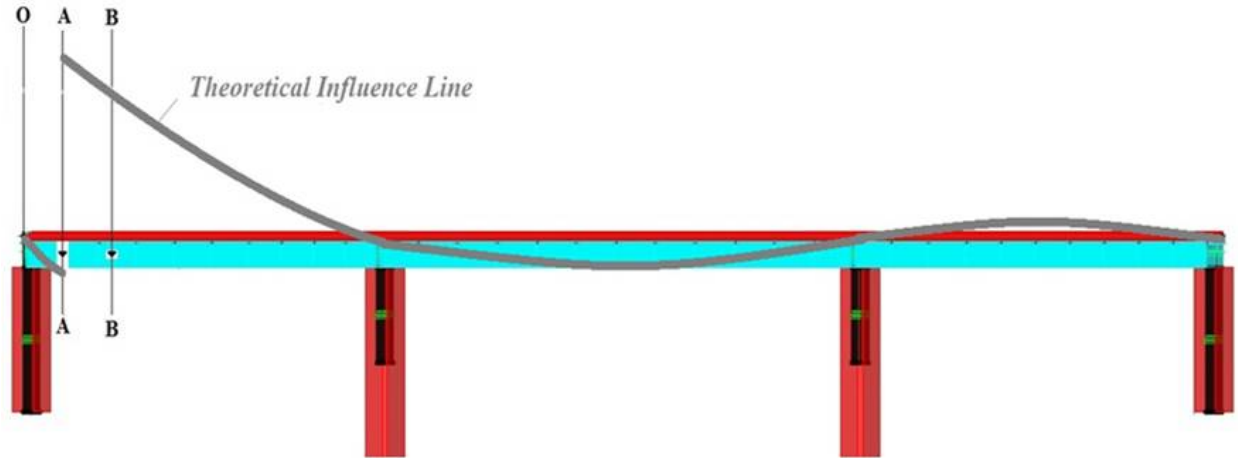
Figure 2.5 Theoretical shear force influence line ($IL'_{(x)}$)

2.3. Field Tests

Shear strain rosette sensors were installed in three bridges: a prestressed concrete box girder bridge in California (called Lambert Road Bridge), and two concrete slab on steel girder bridges with different span lengths in Illinois (called Lock Street Bridge and Salt Creek Bridge). Following the installation of sensors the BWIM system was calibrated and its performance was evaluated by a series of tests involving pre-weighed trucks.

All three bridges were instrumented with optical Fiber Bragg Grating (FBG) rosettes. Each rosette was constructed with two FBG strain sensors. FBG sensors transduce the strains through wavelength shifts of an optical signal. Detailed description of FBG sensors is given in Ansari (2007). The sensors installed inside the concrete box girder of the Lambert Road Bridge had gauge lengths of 75 mm, sensitivity of 1.4 pm/με, and strain limits of ±2500 με. Fig. 2.6a corresponds to the long sensor used in concrete box girder bridges, e.g. Lambert Road Bridge, because of their long web height. The FBG strain sensors which were installed on the steel girders of the Salt Creek and Lock Street Bridges were similar to those that were installed inside the box girders of the

Lambert Road Bridge but with a shorter gauge length of 22 mm. Fig. 2.6b corresponds to the short sensor used in slab on steel girder bridges, e.g. Lock Street and Salt Creek Bridges, because of their short web height. The individual strain sensors were manufactured by Micron Optics, Inc. These sensors are operational over a temperature range of -40 to 120 °C with a sensitivity of 29 pm/°C. All the sensors were protected against adverse environmental and physical elements with steel enclosures. Armored sensor cables were routed to the FBG interrogator data acquisition system through PVC conduits. Rubberized coating as well as a steel box enclose protected the sensors from the possible damages. Fig. 2.7 depicts the rosette sensor covered with rubberized and protected inside a steel box.

(a)

(b)
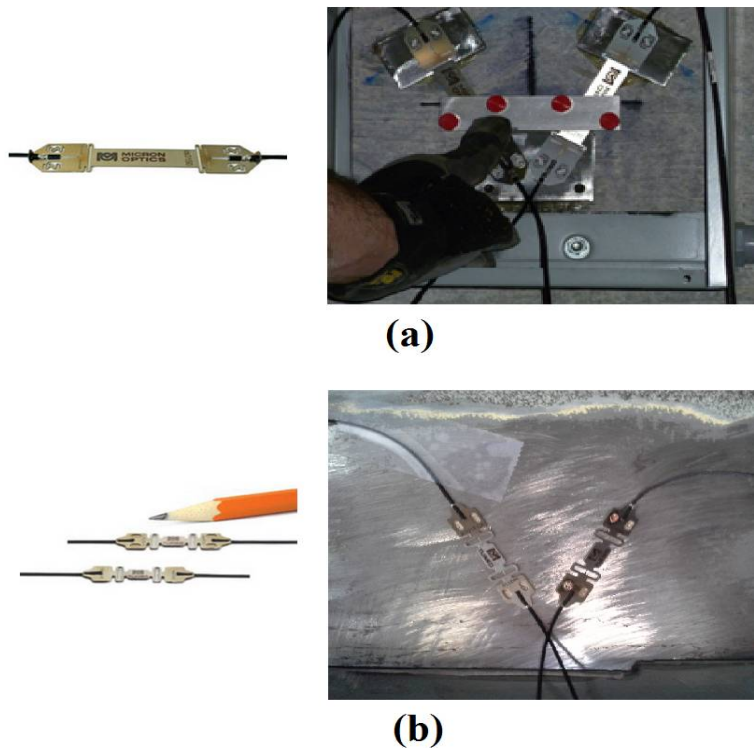
Figure 2.6 FBG Strain Gauge: a) Long gauge, b) Short gauge (www.micronoptics.com)
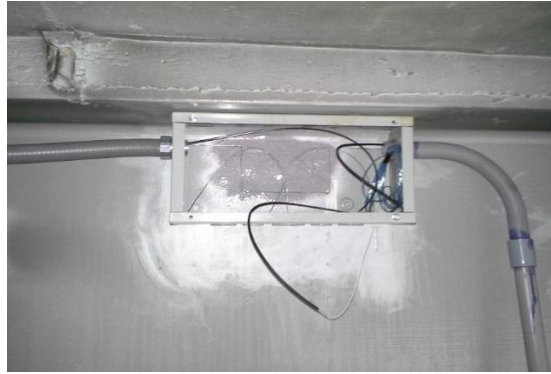
Figure 2.7 A schematic view of rosette sensor installed on the web of steel girder

A steel NEMA enclosure was employed for housing the four channel FBG interrogator data and the solid state field computer as well as the cellular wireless antenna that was used for remote data transmission at the bridge sites. The optical interrogation unit is a Micron Optics sm130 dynamic sensing module and operates within a wavelength range of 1510–1590 nm and has the capability to conduct measurements at a maximum sampling frequency of 500 Hz. Through an Ethernet connection the module was connected to the field computing processor unit for data acquisition purposes. The NEMA enclosure and typical rosette installations for the concrete and the steel girders are shown in Fig. 2.8.
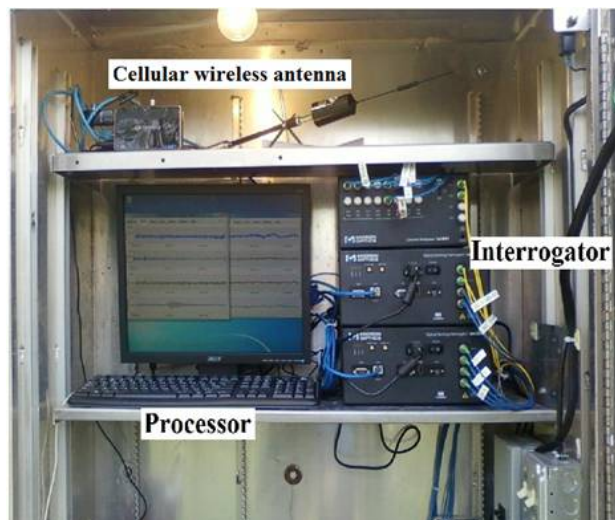
Figure 2.8 a) Site interrogation unit, processor, and cellular antenna within the NEMA enclosure

45

2.3.1. Lambert Road Bridge

The Lambert Road Bridge is located 48 km south of Sacramento and carries the southbound traffic of Interstate 5 over Lambert Road in the city of Elk Grove. The bridge is comprised of two spans, each 39.3 m long for a total structure length of 78.6 m. A diaphragm is located in the middle of each span. The bridge has four inner cells, and access holes were available in the bottom flange and the diaphragms to allow for instrumentation of the inner and outer western cells. The rosette sensors were installed on the webs at a distance of 1.7 m from the south abutment. The second set of sensors was installed at a distance of 9 m from the south abutment. The bridge schematic elevation drawings with the location of the BWIM rosette sensors are shown in Figs. 2.9.
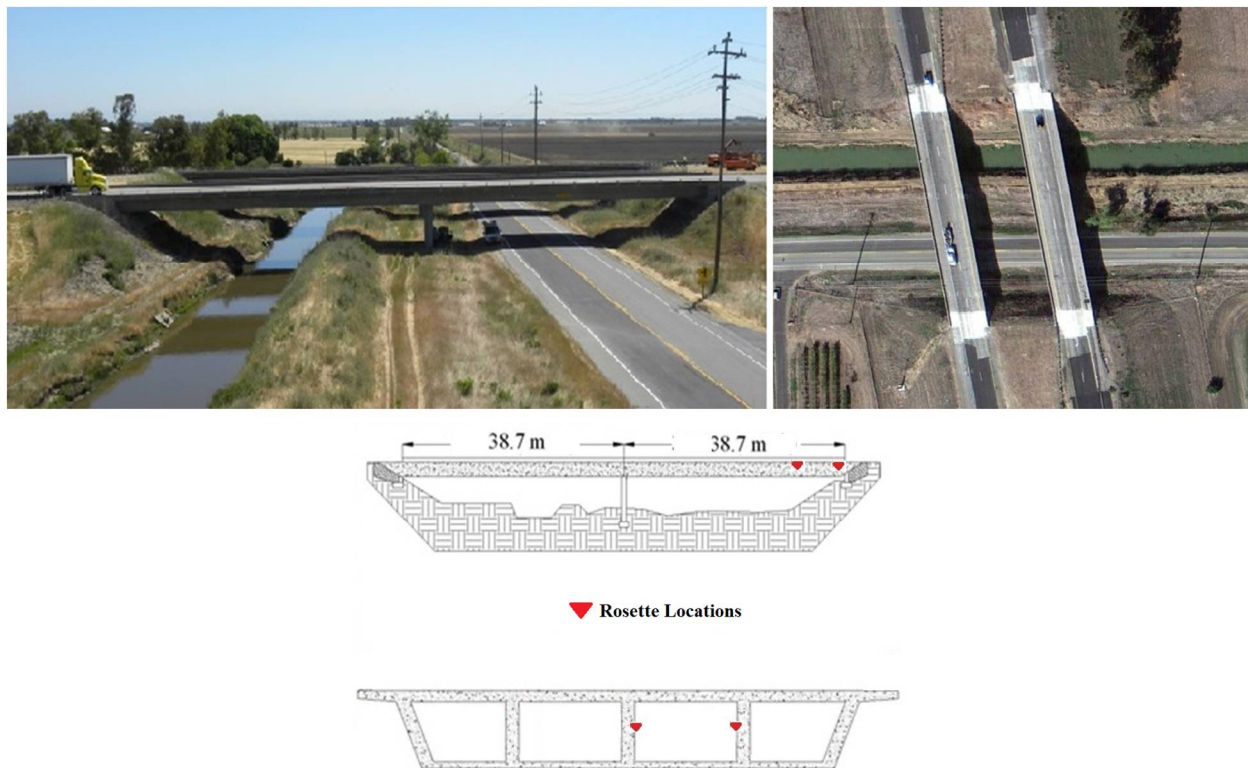
Figure 2.9 Lambert Road Bridge

Field tests involved calibration for the estimation of bridge parameters, α and $IL(x)$, as well as verification tests to examine the accuracy of the proposed approach. A dump

46

truck with a trailer was employed for the evaluation of the BWIM system for the Lambert Road Bridge. The truck and trailer had a combined weight of 36080 kg. Fig. 2.10b shows the dump truck dimensions and weights of the different axles. Table 2.1 shows a summary of the ten runs of the test truck. Moreover, the test runs were conducted in four different paths also shown in Fig. 2.10a. To eliminate the effects of I-5 traffic on the controlled tests, live load tests were performed at night with short periods of highway closures. This limited time available for the tests, and therefore, the same truck was employed both for calibration as well as verification tests in order to hasten the process and limit the number and duration of highway closures. Eight of the truck runs (test Numbers 1-8) were conducted at a slow speed of approximately 5 km/h. The two higher speed tests were conducted at normal highway speed of 84-90 km/h (test numbers 9-10). Load paths 1, 2, and 4 were selected in order to examine the response of the system to the various positions of the truck axles on the lanes over the cell with the shear rosettes. Load path 3 was selected to monitor the effect of truck axles on lanes far away from the instrumented cell. Data from the FBG rosette sensors were acquired at sampling rates of 50 and 500 Hz for the slow and fast speed tests, respectively.

Table 2.1 Details of load test runs for Lambert Road Bridge

Run numbers	Speed of test	Load path
1, 2, 3	Slow	1
4, 5, 6	Slow	2
7, 8	Slow	3
9, 10	Road speed	4
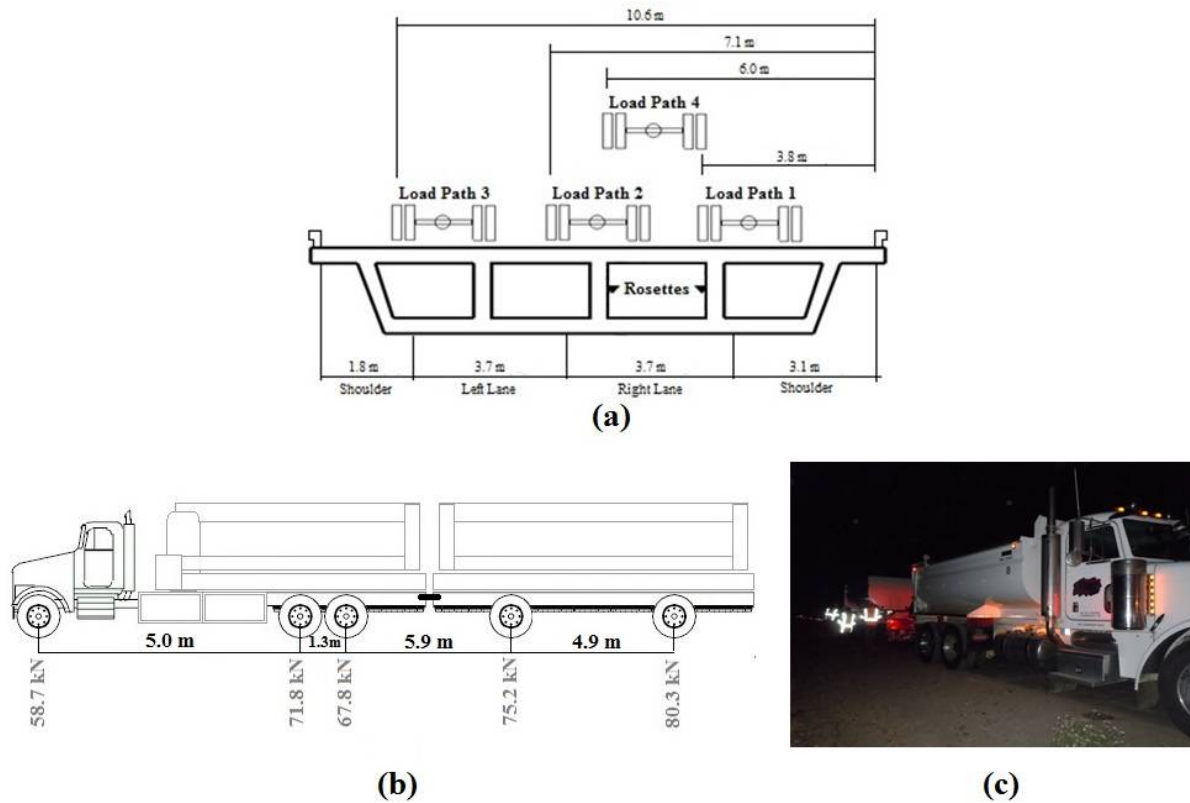
Figure 2.10 a) Loading paths, b) Schematic view of truck and trailer axle load configurations, c) Actual view of truck and trailer

2.3.2. Salt Creek Bridge

The Salt Creek Bridge carries the traffic of Route 83 over the Salt Creek in Elmhurst, Chicago. This bridge is a three-span, continuous steel girder bridge with side spans of 11 m and middle span of 14 m in length. The bridge supports the north and southbound traffic on separate superstructures. The substructure consists of two pier walls and two abutments on the far sides. The maximum width of the bridge at the slab elevation is 13 m and the thickness of the concrete deck is 20 cm. The southbound section of the bridge was selected for this study since it is located at the exit ramp of a truck weigh station which was utilized for weighing the trucks prior to entering the bridge. The first

set of rosette sensors was installed on the webs at a distance of 0.6 m from the south abutment and the second set of sensors was installed on the webs of the girder at a distance of 2.6 m. The bridge schematic elevation drawings with the location of the BWIM rosette sensors are shown in Figs. 2.11.
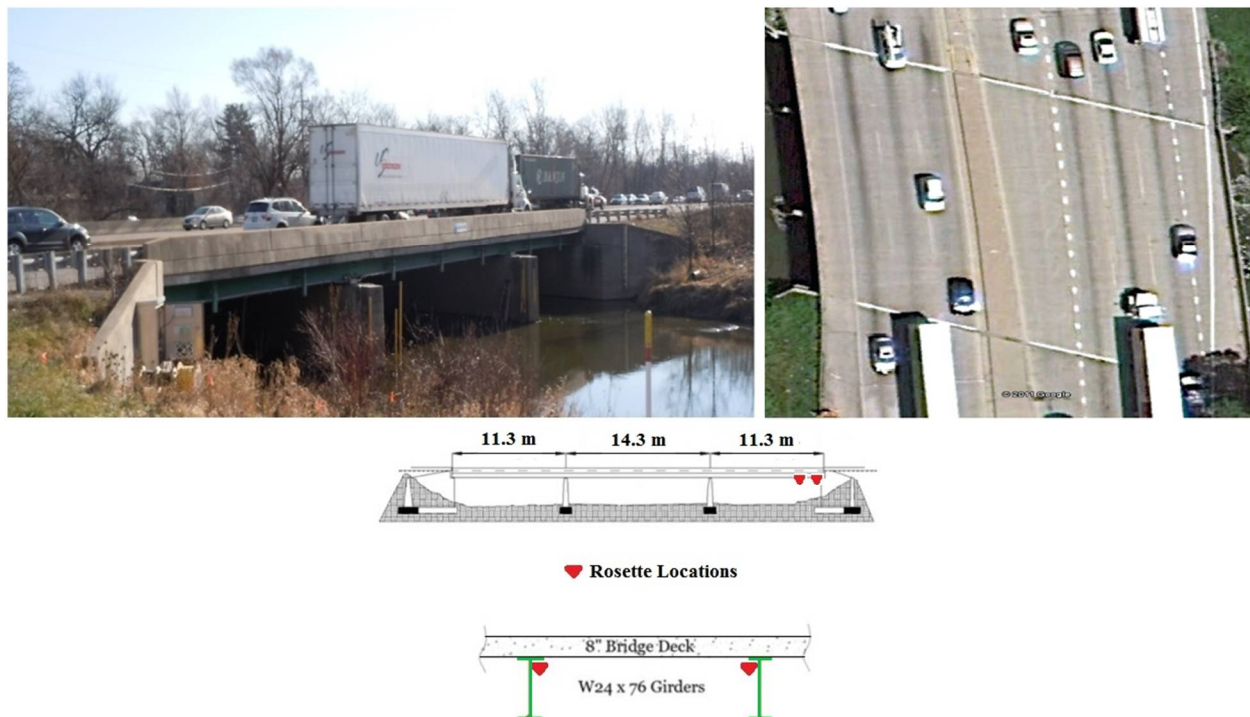
Figure 2.11 Salt Creek Bridge

The Salt Creek Bridge is located within close proximity of the exit of the truck weigh station which is operated by law enforcement agencies. For this bridge, it was convenient to use a number of different commercial trucks as they were pulled to the weigh station for inspections. Samples of the used trucks are shown in Fig. 2.12. Tests involved selection of weighed trucks from the weigh station and acquisition of data during their passage over the bridge. Table 2.2 shows a summary of the truck runs over the bridge. Axle weights and spacing for each truck were measured at the weigh station before the test runs and they are also shown in Table 2.2. The tests were performed

during the daytime with normal car traffic and no other trucks on the bridge. All the test runs were performed over the lane under which the girder was instrumented with the rosette sensors. Tests were performed at slower speeds of 16 km/h to 52 km/h since the bridge entrance was within close proximity of a traffic signal and the weigh station. For these tests, data from the FBG rosette sensors were acquired at sampling rates of 35 Hz.

Figure 2.12 Samples of used trucks: a) two-axle on the weigh station, b) two-axle on the road, c) five-axle on the weigh station, d) five-axle on the road

Table 2.2 Truck weights and axle spacing as measured at the weigh station at the Salt Creek Bridge

Run number	Velocity (km/h)	Number of axles	Axle weights (kN)	Axle spacing (m)
1	45	3	P_1: 47.2 P_2: 73.8 P_3: 45.0	L_1: 4.7 L_2: 9.8
2	45	3	P_1: 41.1 P_2: 48.5 P_3: 29.6	L_1: 3.5 L_2: 8.5
3	52	3	P_1: 43.2 P_2: 124.5 P_3: 113.1	L_1: 3.5 L_2: 3.8
4	24	2	P_1: 58.4 P_2: 122.6	L_1: 4.6
5	37	2	P_1: 58.4 P_2: 122.6	L_1: 4.6
6	45	2	P_1: 58.4 P_2: 122.6	L_1: 4.6
7	39	2	P_1: 58.4 P_2: 122.6	L_1: 4.6
8	16	2	P_1: 35.3 P_2: 50.1	L_1: 3.8
9	19	2	P_1: 35.3 P_2: 50.1	L_1: 3.8

2.3.3. Lock Street Bridge

The Lock Street Bridge crosses the Lock Street and carries the north and south bounds traffic of I-55 (Stevenson's expressway) in separate superstructures. The bridge is located approximately 10 miles southwest of downtown Chicago. This bridge is a three-span, continuous steel girder bridge with side spans of 18.4 m and middle span of 21.1 m in length. The substructures for the north and south bounds consist of two pier walls and two abutments on the far sides and carry four driving lanes. The maximum width of the bridge at the slab elevation is 20 m and the thickness of the concrete deck is 21.6 cm. For north bound, the first and second rosette sensors sets were respectively

installed on the webs at a distance of 2.7 m and 6.1 m from the north abutment. For the south bound, the similar sets of rosette sensors were installed at a distance of 2.7 m and 6.1 m from the south abutment. The bridge schematic elevation drawings with the location of the BWIM rosette sensors are shown in Figs. 2.13.
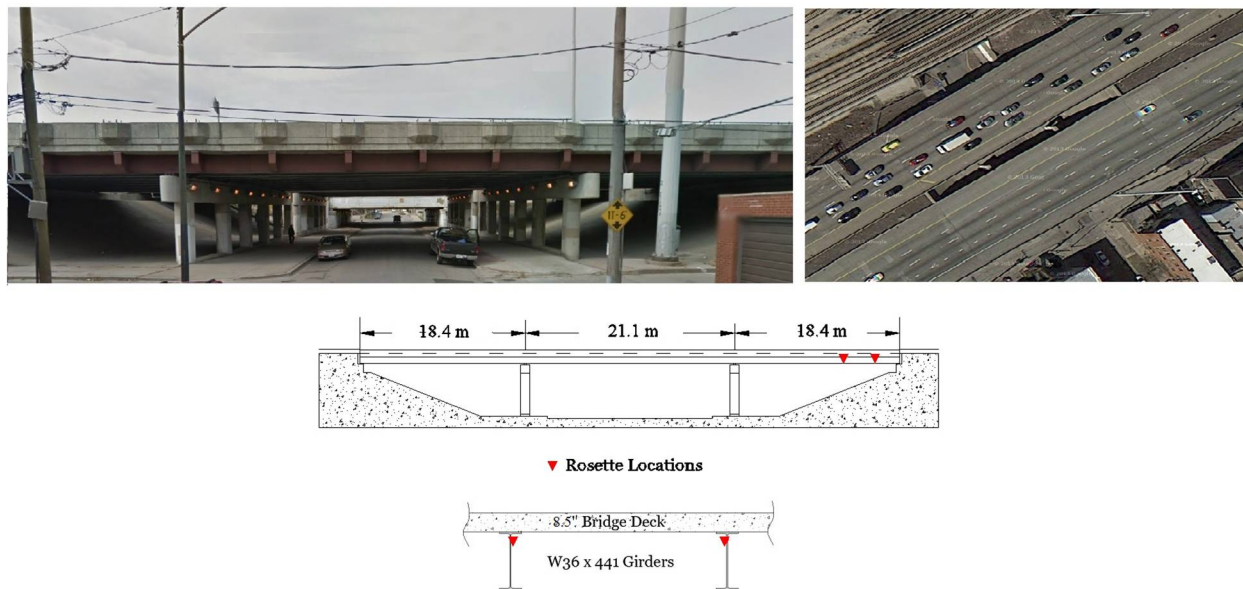

Figure 2.13 Lock Street Bridge

For the Lock Street Bridge, a two-axle truck (including one tandem axle), shown in Fig. 2.14, was used for test runs. The pre-weighed truck was employed for calibration as well as verification tests because there were no weigh stations close to the testing area. The bridge carried a large volume of traffic, and instead of closing the road, designated small marked trucks with warning signs were employed as escorts to move and divert the traffic in front and behind the calibration truck. The truck lanes (slower lanes) from each of the north and south bounds of the bridge were instrumented with the BWIM sensors (Fig. 2.15). Table 2.3 provides a summary of test speeds and the bridge lanes involved in the tests. Data from the FBG rosette sensors were acquired at 100 Hz.

Figure 2.14 Truck configurations
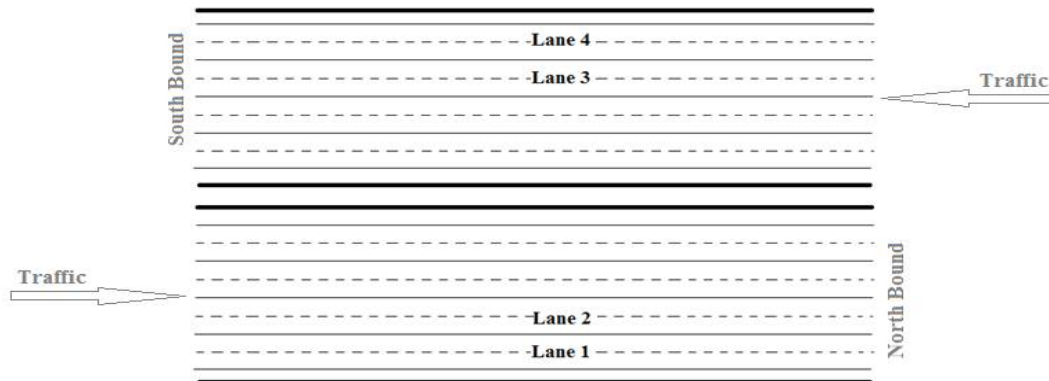
Figure 2.15 Loading paths

Table 2.3 Details of load test runs for Lock Street Bridge

Run number	Velocity (km/h)	Testing lane
1	57	4
2	53	4
3	61	4
4	53	4
5	79	3
6	80	3
7	79	3
8	78	3
9	77	3
10	72	2
11	43	2
12	52	2
13	72	1
14	52	1
15	52	1

2.4. Field Tests Results

The system of equations, Eq. (32), was employed for calibration as well as for verification and evaluation of BWIM system. Truck tests were performed both for calibration as well as verification of the method. During the calibration tests, data from the measured peak shear strains, γ_{A_i}, axle weights and axle spacings from the calibrated trucks and the shear force influence line, $IL'(x)$ were employed as known input to these equations for the computation of bridge parameters, α, and the shear strain influence line, $IL(x)$. α, and $IL(x)$ are unique for each lane. α is termed as the bridge parameter and influences accuracy of the BWIM system throughout the service life of the bridge. It is a function of the section and materials properties as demonstrated in Eq. (8). From the practical point of view, however α varies along the cross section of the bridge depending on the location (lane), elevation in the cross section and the geometrical characteristics of the section. Following calibration tests, with the known bridge parameters, α, and $IL(x)$, the above-mentioned equations were utilized again, this time for estimation of truck weights in order to evaluate the efficacy of the proposed BWIM system.

In addition to ambient noise at higher sampling rates, the dynamic interaction of the bridge with the trucks at highway speeds generates additional signal oscillations to the static response. Accurate detection of signal peaks requires removal of the dynamic and noisy parts of the recorded signals. Amongst the methods that were previously developed and yielded successful results include the Moving Force Identification (MFI) method. While MFI is promising and results have indicated that the method is capable of filtering the dynamic effects from the measurements, it requires further development

54

for real time applications (Brown 2011; Law et al. 1997; Law et al. 1999; Yu and Chan 2003, 2007; Chan et al. 1999). Review of technical literature indicates successful application of the wavelet based filters to the signals generated from the moving of multiple axles in bridges. For instance, Chatterjee et al. (2006) employed an "rbio2.4" mother wavelet for such signals and reported that they could clearly identify the number and relative positions of the axles. Later, Lechner et al. (2010) used a fast wavelet transform algorithm and demonstrated the computing efficiency of the wavelet filter in BWIM applications.

A number of different mother wavelets were investigated and tested for the shear strain response signals acquired in this study. The requirements for the wavelet filter were accuracy in terms of axle shear strain peak detection capability, and real time analysis of signals. Results from analysis of the signals indicated that the mother wavelets "sym3" and "db2" were most computationally efficient in filtering the noise and dynamic effects for the present application. A typical shear strain response of the strain rosette to the four axle group (one of the axles being tandem) truck-trailer combination on the concrete box girder bridge is shown in Fig. 2.16. Strain response data shown on the insets of Fig. 2.16 correspond to the signals filtered by the wavelet filters employed in the present study. As demonstrated in Fig. 2.16, the wavelet filter is effective in enhancing the signal. Moreover, the wavelet filter further improves the axle and peak detection capabilities in real time monitoring of signals (Chatterjee et al. 2006).
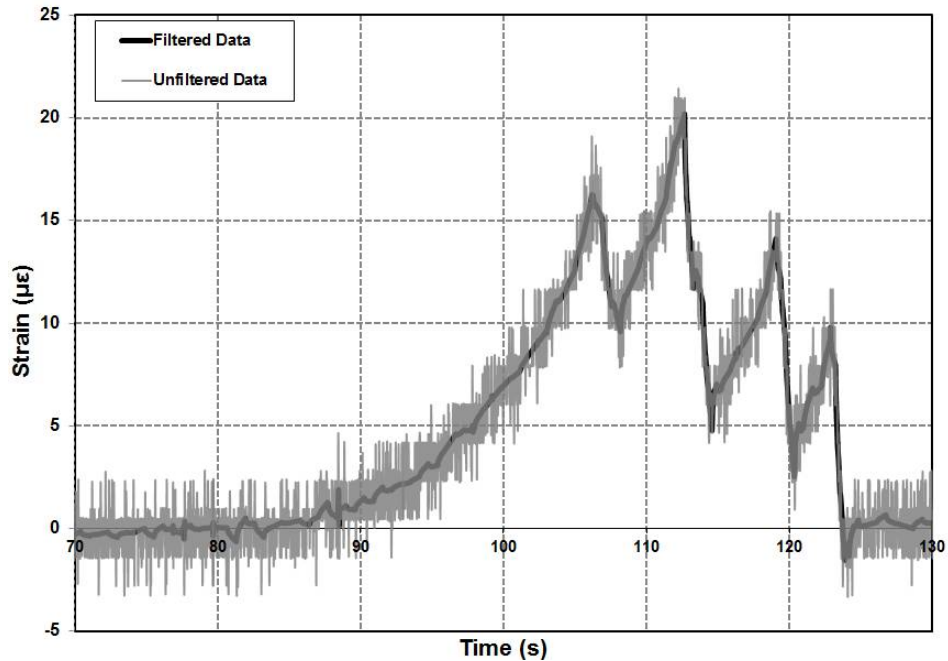
Figure 2.16 Shear strain response of the strain rosette with and without filtering

2.4.1. Lambert Road Bridge Results

Shear and flexural response of the Lambert Road Bridge to the four axle group truck are compared in Figs. 2.17 through 2.18. As shown in these figures, the difference between the flexural and shear responses is that the flexural strain represents the overall response of the bridge to truck weight, whereas, the shear strain provides details about the number of axles based on the shear strain peaks.
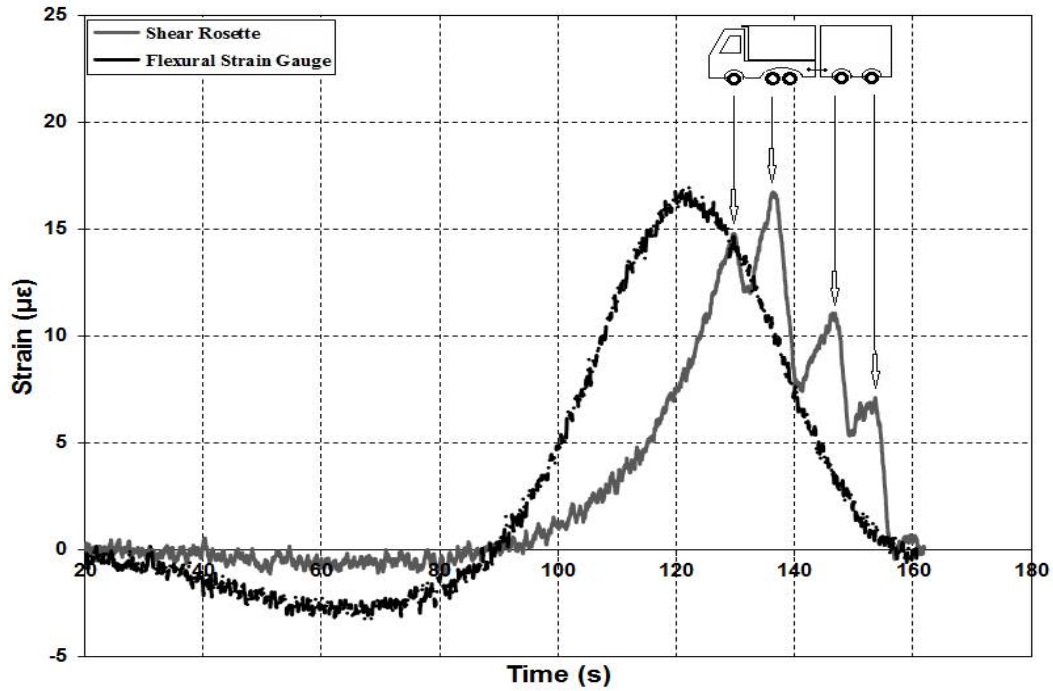
Figure 2.17 Shear and flexural response of the Lambert Road Bridge
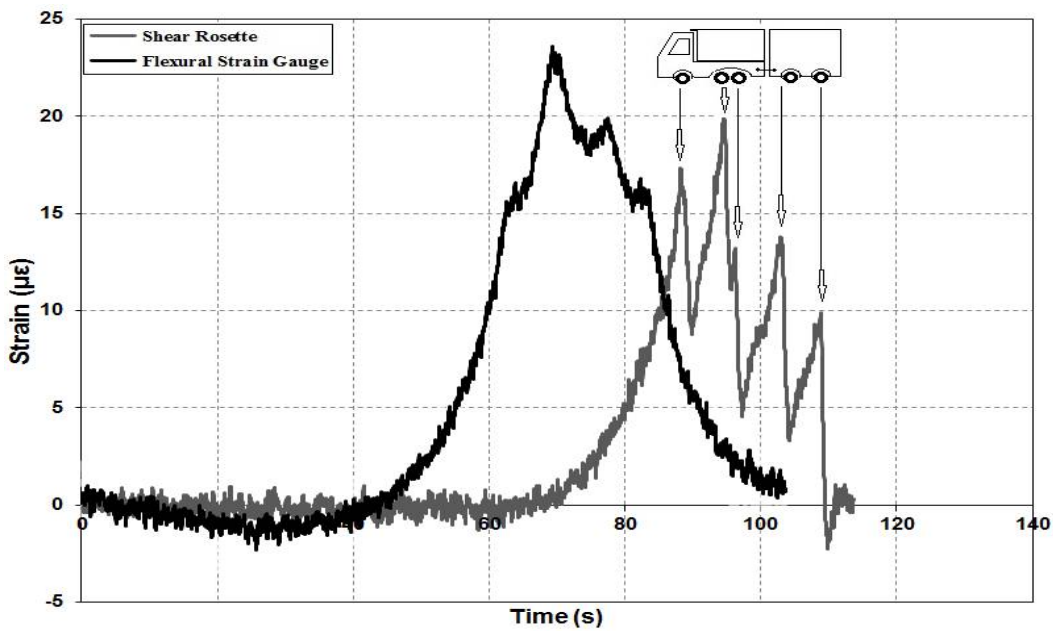
Figure 2.18 Shear and flexural response of the Lambert Road Bridge

For the Lambert Road Bridge truck run numbers 1, 3, 4, 6, and 10 were employed for calibration and determination of bridge parameter α. As discussed earlier, considering

57

the difficulties in halting the traffic on I-5 for long periods of time, only one type of truck was employed with limited number of tests on two instrumented lanes. Table 2.4 pertains to the results from the calibration tests from which the α values were obtained for the Lambert Road Bridge. Run numbers 1, 3, and 10 were employed for the calibration of the lanes sharing the same geometric characteristics in cross section (load paths 1 and 4 in Table 2.1). The average and standard deviation are 13313.3 N-m/m and 632.5 N-m/m, respectively. Run numbers 4 and 6 corresponded to load path 2. The average and standard deviation are 9932 N-m/m and 394.6 N-m/m, respectively. The average values of α for each path were considered for the estimation of the truck weights in the validation tests.

As an example, Table 2.5 describes the mathematical formulation used during the calibration process in order to calculate the value of α for Run#1. As the first step, the shear strain peaks (rosette A) corresponding to the individual or tandem axles were extracted from the recorded shear strain response (see Fig. 2.4a). It should be noted that the filtering was already implemented on the recorded shear strain response (see Fig. 2.16). In the second step, the shear force influence line, $IL'(x)$, has been calculated using the conventional structural analysis theories (see Fig. 2.5). In the third step, for given S_0 and S_1 and known values of axle spacing and weights the system of strain-load equations were generated as explained in Eq. (33) to calculate the α. It is obvious that each equation releases a unique value of α, however, since these values are close together the average of them was finally selected as the α value.

$$
\begin{cases}
\gamma_{A4} = \dfrac{1}{\alpha_4}\left[P_4 IL'(S_0)\right] \\[2mm]
\gamma_{A3} = \dfrac{1}{\alpha_3}\left[P_4 IL'(S_0 + L_3) + P_3 IL'(S_0)\right] \\[2mm]
\gamma_{A2} = \dfrac{1}{\alpha_2}\left[P_4 IL'(S_0 + L_3 + L_2) + P_3 IL'(S_0 + L_2) + P_2 IL'(S_0)\right] \\[2mm]
\gamma_{A1} = \dfrac{1}{\alpha_1}\left[P_4 IL'(S_0 + L_3 + L_2 + L_1) + P_3 IL'(S_0 + L_2 + L_1) + P_2 IL'(S_0 + L_1) + P_1 IL'(S_0)\right] \\[2mm]
\alpha = (\alpha_1 + \alpha_2 + \alpha_3 + \alpha_4)\big/ 4
\end{cases}
\tag{Eq. 33}
$$

Table 2.4 Calibrated values of α for the Lambert Road Bridge

Run	Run#1	Run#3	Run#4	Run#6	Run#10
α (N.m/m)	12646	13390	9653	10211	13904

Table 2.5 Calibration process used for Run#1

Step 1	Step 2	Step 3	Step 4
$\gamma_{A1} = 18.3\ \mu\varepsilon$	$IL'(X)$	$S_0 = 1.7\ \text{m},\ S_1 = 7.5\ \text{m},\ P_1 = 58.7\ \text{kN},\ L_1 = 5.7\ \text{m}$	$\alpha = \text{average}(\alpha_1, \alpha_2, \alpha_3, \alpha_4)$
$\gamma_{A2} = 19.1\ \mu\varepsilon$	$= 1 - 0.004X - 1.16$	$P_2 = 139.7\ \text{kN},\ L_2 = 6.6\ \text{m}$	$= 12646\ \text{N}.\dfrac{\text{m}}{\text{m}}$
$\gamma_{A3} = 10.5\ \mu\varepsilon$	$* 10^{-7} * X(49923 - X^2),$	$P_3 = 75.2\ \text{kN},\ L_3 = 4.9\ \text{m}$	
$\gamma_{A4} = 6.2\ \mu\varepsilon$	$X > S_0\ (= 1.7\ \text{m})$	$P_4 = 80.3\ \text{kN}$	

By using the computed parameters the efficiency of the proposed system was examined in all three of the bridges by a number of truck runs. For the Lambert Road Bridge, truck runs numbers 2, 5, and 9 (Table 2.1) were employed for evaluation of the BWIM system. Results for these tests are shown in Tables 2.6 through 2.7. Results shown in Tables 2.6 and 2.7 pertain to the estimated truck axle spacings and axle weights by the proposed BWIM system, respectively. Also shown in Tables 2.6 and 2.7, are the actual spacing and weights of the truck axles as measured at the weigh station. Except for run number 5, estimated truck weights compared well with the actual values measured at the weigh station. Results for axle spacing followed similar patterns. The tests on load path 3, i.e. truck runs 7 and 8 were conducted in order to examine the response of the rosettes to the axle weights on lanes further away from the instrumented girders. Shear

responses of the rosette to the axle weights directly above or further away from the instrumented girder are compared in Fig. 2.19. In compare to the effect of the trucks directly over the rosette sensors, the effects of trucks at far ends may be minimal but still sufficient to increase the error.

Table 2.6 Final axle spacing results for the Lambert Road Bridge

		Actual Axle Spacing (m)	Measured Axle Spacing (m)	Error (%)
Run#2	L1	5.7	5.9	4.0
	L2	6.6	6.1	-7.2
	L3	4.9	4.3	-11.9
	L total	*17.2*	*16.3*	*-4.8*
Run#5	L1	5.7	5.3	-6.2
	L2	6.6	6.5	-2.1
	L3	4.9	4.6	-5.0
	L total	*17.2*	*16.4*	*-4.3*
Run#9	L1	5.7	6.1	7.2
	L2	6.6	7.6	14.5
	L3	4.9	4.4	-10.0
	L total	*17.2*	*18.0*	*5.2*

Table 2.7 Final axle weight results for the Lambert Road Bridge

		Actual Weight (kN)	Measured Axle Weight (kN)	Error (%)
Run#2	P1	58.7	60.6	3.2
	P2	139.7	138.1	-1.1
	P3	75.2	83.1	10.6
	P4	80.3	74.3	-7.4
	GVW	*353.8*	*356.0*	*0.6*
Run#5	P1	58.7	69.6	18.5
	P2	139.7	129.6	-7.2
	P3	75.2	77.4	3.0
	P4	80.3	75.0	-6.5
	GVW	*353.8*	*351.7*	*-0.6*
Run#9	P1	58.7	60.9	3.7
	P2	139.7	150.6	7.8
	P3	75.2	75.5	0.4
	P4	80.3	72.1	-10.1
	GVW	*353.8*	*359.1*	*1.5*
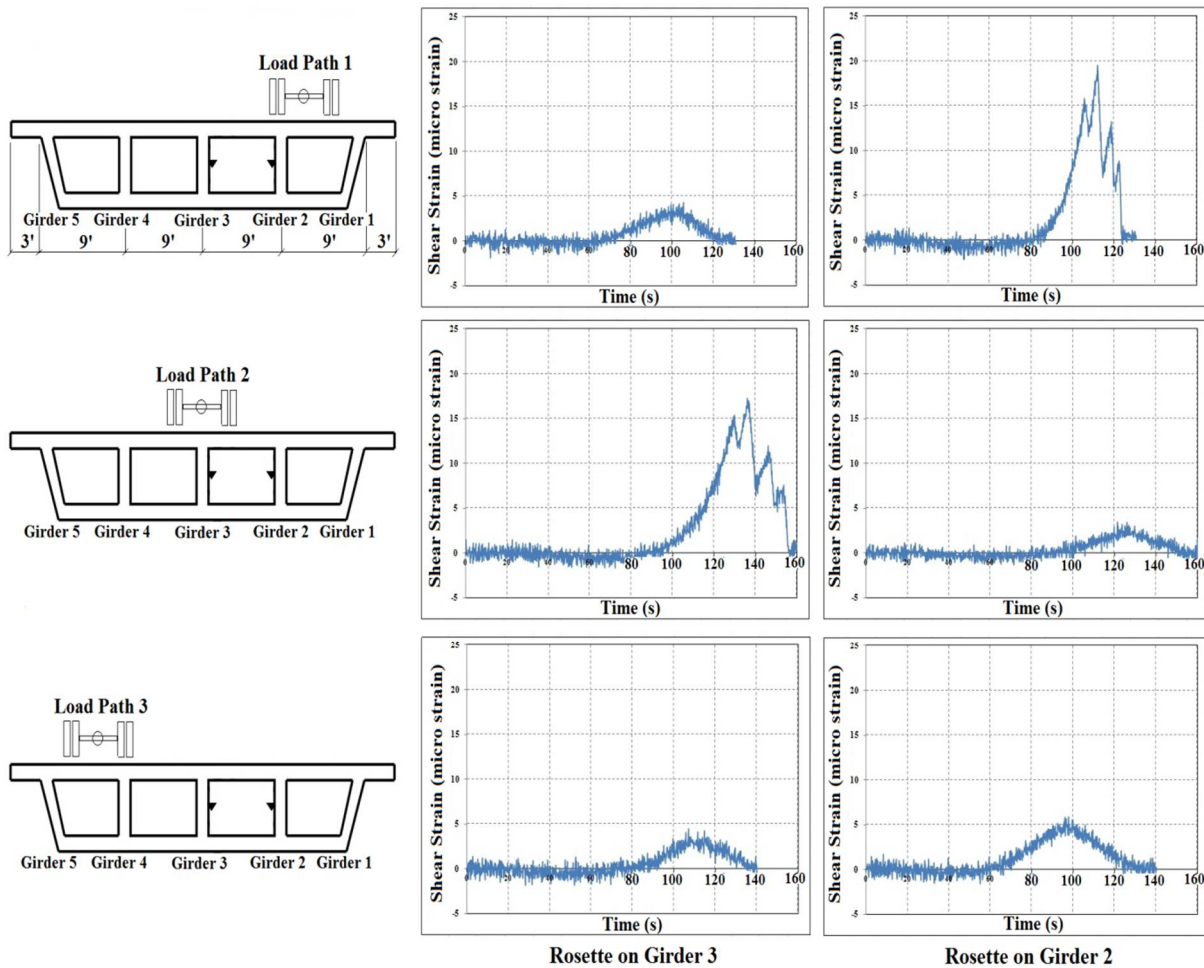
Figure 2.19 The responses of different loading paths regarding rosette sensors in two consecutive girders (Lambert Road Bridge)

Again as an example, this time for validation process, Table 2.8 describes the mathematical formulation used during the real time axle spacing and weight calculations for Run#2. As the first step, the shear strain peaks (rosette A) corresponding to the individual or tandem axles were extracted from the recorded shear strain response during Run#2 test. Noted that the filtering was already implemented on the recorded shear strain response. In the next steps (steps 2 through 3), the velocity has been achieved by using the time difference between the first axle (or other axles) crossing over rosette A and B. In the following step 4, by using the time difference between the

61

consecutive individual axle peaks crossing over rosette A (or B), the different axle spacings were calculated. Then, Using the same shear force influence line, $IL'(x)$, achieved on Calibration stage as well as the calibrated α (e.g. 12646 for Run#1) the shear strain influence line ($IL(x) = \frac{IL'(x)}{\alpha}$ $Eq.$ (11)) was formulated. Applying the given S_0 and S_1 and calculated values of axle spacing, the $IL(x)$ function is quantified and the general system of strain-load equations (Eq. 32) were reversely generated. Eq. (34) rewrites the general Eq. (32) for the Run#2 test specifications. As the last step, the individual axle spacing and weights were calculated. Finally, the total length of truck as well as the GVW were calculated by summation of all the calculated individual axle spacing and weights.

$$\begin{cases} \gamma_{A4} = P_4 IL(S_0) \rightarrow P_4 = 74.3\ kN \\ \gamma_{A3} = P_4 IL(S_0 + L_3) + P_3 IL(S_0) \rightarrow P_3 = 83.1\ kN \\ \gamma_{A2} = P_4 IL(S_0 + L_3 + L_2) + P_3 IL(S_0 + L_2) + P_2 IL(S_0) \rightarrow P_2 = 138.1\ kN \\ \gamma_{A1} = P_4 IL'(S_0 + L_3 + L_2 + L_1) + P_3 IL'(S_0 + L_2 + L_1) + P_2 IL'(S_0 + L_1) + P_1 IL'(S_0) \rightarrow P_1 = 60.6\ kN \end{cases} \quad (Eq.\,34)$$

Table 2.8 Validation process used for Run#2

Step 1	Step 2	Step 3	Step 4	Step 5	Step 6
γ_{A1} $= 19.2~\mu\varepsilon$	t_1 $= 87.66~s$	$V_1 = 3.1~kmh$	$L_1 = 5.9~m$	IL($S_0 = 1.7$ m) $= 333*10^{-6}$, IL($S_0 + L_1 = 7.4$ m) $= 270*10^{-6}$, IL($S_0 + L_1 + L_2 = 14$ m) $= 200*10^{-6}$, IL($S_0 + L_1 + L_2 + L_3$ $= 18.8$ m) $= 151*10^{-6}$	$P_1 = 60.6$ kN
γ_{A2} $= 18.7~\mu\varepsilon$	t_2 $= 94.56~s$	$V_2 = 2.9~kmh$	$L_2 = 6.1~m$	IL($S_0 = 1.7$ m) $= 333*10^{-6}$, IL($S_0 + L_2 = 8.3$ m) $= 260*10^{-6}$, IL($S_0 + L_2 + L_3$ $= 13.2$ m) $= 208*10^{-6}$	$P_2 = 138.1$ kN
γ_{A3} $= 10.9~\mu\varepsilon$	t_3 $= 102.24~s$	$V_3 = 2.8~kmh$	$L_3 = 4.3~m$	IL($S_0 = 1.7$ m) $= 333*10^{-6}$, IL($S_0 + L_3 = 6.6$ m) $= 279*10^{-6}$	$P_3 = 83.1$ kN
γ_{A4} $= 5.6$	t_4 $= 107.84~s$			IL($S_0 = 1.7$ m) $= 333*10^{-6}$	$P_4 = 74.3$ kN
			$L_{Total} = 16.3~m$		GVW $= 356.1$ kN

2.4.2. Salt Creek Bridge Results

Similar to Lambert Road Bridge test results, the flexural and shear responses of the Salt
Creek Bridge to a two and three axle group trucks are compared in Figs. 2.20 and 2.21,
respectively. For the two axle group truck (that includes a tandem axle), it was possible
to also detect the effect of the tandem axle as double peaks in the shear response.
However, the effect of tandem axles was not observed on the shear response for the
three axle group truck. The effects of tandem axles were also not apparent on the shear
response of the Lambert Road Bridge. Recognition of tandem axles may be attributed to
a number of factors, including the intra-axle spacings within individual tandems, tandem
axle weight, bridge stiffness, bridge-vehicle interaction, and vehicle speed. However, a
tandem or tridem axle group can be detected as a whole. Also shown in Figs. 2.20 and

2.21 are the flexural responses of the Salt Creek Bridge to two and three axle group trucks, where the number of peaks does not correlate with the number of individual axles since the response to two and three axle trucks were only represented with one and two peaks, respectively.
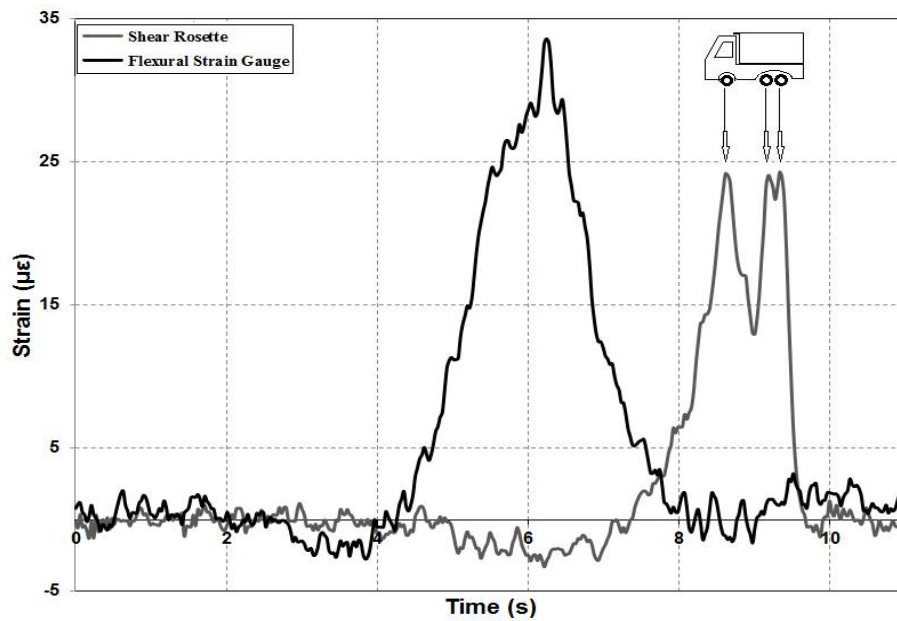
Figure 2.20 Shear and flexural response of the Salt Creek Bridge
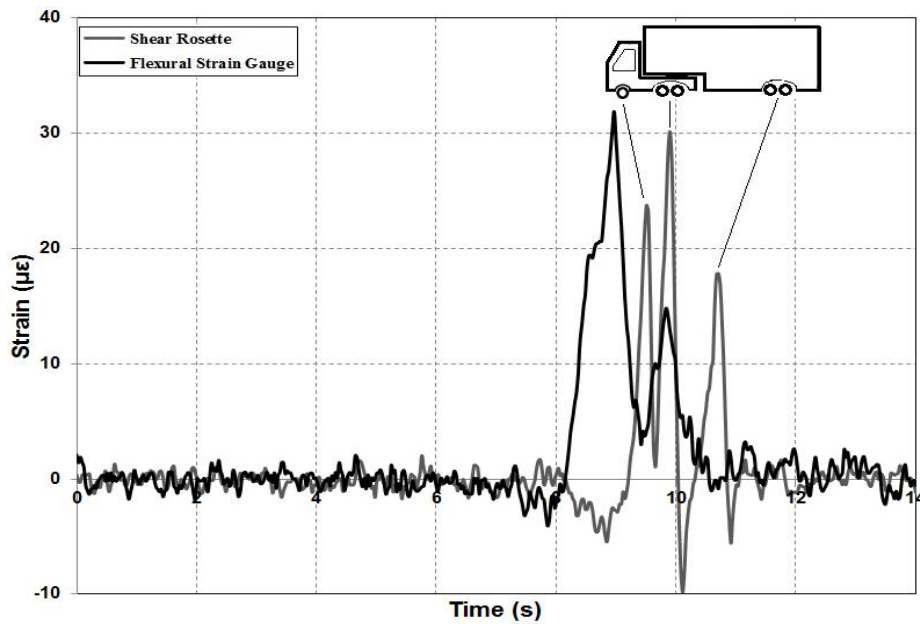
Figure 2.21 Shear and flexural response of the Salt Creek Bridge

64

For the Salt Creek Bridge, it was possible to conduct tests with several truck types and weights. These tests involved 9 runs all on the same lane. For this bridge truck runs 1, 2, 5, 6, 8, and 9 were selected for calibration and determination of α. Calibration test results for this bridge are shown in Table 2.9. The measured parameter, α for all the runs were sufficiently close so that it was possible to consider the average value as the bridge parameter for that instrumented lane. The average and standard deviation of the measurements shown in Table 2.9 are 2043.5 N-m/m and 122.6 N-m/m, respectively.

Table 2.9 Calibrated values of α for the Salt Creek Bridge

Run	Run#1	Run#2	Run#5	Run#6	Run#8	Run#9
α (N.m/m)	1900	2071	2035.1	1905	2173	2177

For the Salt Creek Bridge truck runs 3, 4, and 7 were employed for the prediction of truck weights and axle spacing. Results for these series of tests are shown in Tables 2.10 and 2.11. BWIM data in Tables 2.10 and 2.11 are compared with the actual axle spacing and weight of the test trucks.

Table 2.10 Final axle spacing results for the Salt Creek Bridge

		Actual Axle Spacing (m)	Measured Axle Spacing (m)	Error (%)
	L1	4.7	4.4	-7.7
Run#3	L2	9.8	9.8	0.6
	L total	*14.5*	*14.2*	*-2.1*
Run#4	L1	4.6	5.2	13.2
Run#7	L1	4.6	5.0	8.6

Table 2.11 Final axle weight results for the Salt Creek Bridge

		Actual Weight (kN)	Measured Axle Weight (kN)	Error (%)
Run#3	P1	47.2	47.5	0.6
	P2	73.8	75.9	2.8
	P3	45.0	45.5	1.0
	GVW	*166.1*	*168.9*	*1.7*
Run#4	P1	58.4	61.2	4.7
	P2	122.4	115.2	-5.9
	GVW	*180.9*	*176.4*	*-2.5*
Run#7	P1	58.4	61.2	4.7
	P2	122.4	127.2	3.9
	GVW	*180.9*	*188.4*	*4.2*

BWIM results at Salt Creek Bridge provide better correlation with the actual weights. In the majority of test runs, the errors are within 6%. The main reason for better accuracy in this case was the fact that calibration was more rigorous and the bridge parameter obtained was based on several tests. As noted earlier, it was not possible to do the same at Lambert Road Bridge. Other factors may be attributed to the effect of bridge type and stiffness as well as bridge width, girder spacings, span lengths and skew.

2.4.3. Lock Street Bridge Results

For the Lock Street Bridge, it was possible to conduct multiple tests with only one pre-weighed truck in different lanes. Test run numbers 1,5,10, and 13 were employed for the determination of the bridge parameter, α, in lanes 4, 3, 2, and 1. Calibration test results for this bridge are shown in Table 2.12.

Table 2.12 Calibrated values of α for the Lock Street Bridge

Run	Run#1	Run#5	Run#10	Run#13
α (N.m/m)	2978	3070	2849	2992

Truck runs 2, 3, 4, 6, 7, 8, 9, 11, 12, 14 and 15 were employed for the verification tests as shown in Tables 2.13 and 2.14. The estimated GVW errors were less than 8% and except for few runs, estimated individual axle weights compared well with the actual values. The estimated axle spacings also were reported to have less than 10% error compared with the actual truck axle spacings.

Table 2.13 Final axle spacing results for the Lock Street Bridge

		Actual Axle Spacing (m)	Measured Axle Spacing (m)	Error (%)
Run#2	**L1**	6.2	6.03	-2.8
Run#3	**L1**	6.2	6.03	-2.8
Run#4	**L1**	6.2	6.24	0.6
Run#6	**L1**	6.2	5.69	-8.3
Run#7	**L1**	6.2	6.01	-3.1
Run#8	**L1**	6.2	5.95	-4.0
Run#9	**L1**	6.2	6.03	-2.7
Run#11	**L1**	6.2	6.20	0.0
Run#12	**L1**	6.2	6.11	-1.5
Run#14	**L1**	6.2	5.63	-9.2
Run#15	**L1**	6.2	5.63	-9.2

Table 2.14 Final axle weight results for the Lock Street Bridge

		Actual Weight (kN)	Measured Axle Weight (kN)	Error (%)
Run#2	**P1**	87.1	96.7	11.0
	P2	165.0	149.7	-9.3
	GVW	*252.1*	246.4	*-2.3*
Run#3	**P1**	87.1	84.3	-3.2
	P2	165.0	179.6	8.8
	GVW	*252.1*	265.2	*5.2*
Run#4	**P1**	87.1	102.1	17.2
	P2	165.0	138.1	-16.3
	GVW	*252.1*	240.3	*-4.7*
Run#6	**P1**	87.1	93.3	7.1
	P2	165.0	168.0	1.8
	GVW	*252.1*	260.7	*3.4*
Run#7	**P1**	87.1	92.1	5.7
	P2	165.0	171.5	3.9
	GVW	*252.1*	263.5	*4.5*
Run#8	**P1**	87.1	87.4	0.3
	P2	165.0	173.8	5.3
	GVW	*252.1*	261.7	*3.8*
Run#9	**P1**	87.1	80.7	-7.4
	P2	165.0	156.0	-5.5
	GVW	*252.1*	237.0	*-6.0*
Run#11	**P1**	87.1	89.3	2.5
	P2	165.0	166.0	0.6
	GVW	*252.1*	255.2	*1.2*
Run#12	**P1**	87.1	98.4	13.0
	P2	165.0	162.6	-1.5
	GVW	*252.1*	259.2	*2.8*
Run#14	**P1**	87.1	71.1	-18.4
	P2	165.0	161.2	-2.3
	GVW	*252.1*	232.2	*-7.9*
Run#15	**P1**	87.1	88.1	1.2
	P2	165.0	163.2	-1.1
	GVW	*252.1*	251.4	*-0.3*

2.5. Summary of the chapter

The method described in this article pertains to the development of a new type of BWIM based on the measurement of shear forces near the supports of the bridges. Fiber optic

FBG rosette sensors were employed for the implementation of this approach. The specific advantages of FBG rosette sensors for this application were high-resolution measurements and serial multiplexing. The shear based sensors are also self-temperature compensating and the effects of temperature variation will be eliminated due to the structure of the shear sensors. There is no need to calibrate the system for different temperatures. However, the flexural based BWIM system that uses the flexural sensors for calculations will need to calibrate their system with temperature variations. Moreover, the temperature effects must be compensated using temperature-sensors. Development of the method involved use of shear strain influence lines leading to the systems of equations in terms of truck axle weights and spacing. In the proposed shear based BWIM, sensors are installed near abutments while in the flexural based BWIM sensors much be attached in the middle of spans. As a result, very little local road traffic interruptions are required and provide improved accessible locations for installation or maintenance. The methodology introduced here is capable for application to determinate as well as indeterminate structural systems. Proper application of the method also requires calibration of the BWIM for the estimation of the bridge parameter α, which is a function of the cross sectional and materials properties of the bridge. Three different bridges, a box girder prestressed concrete, and two concrete slab on steel girder bridges with different span lengths were instrumented for the evaluation of the proposed BWIM system. Field implementation involved a series of truck runs for calibration and evaluating the efficiency of the BWIM system. Measured and actual truck axle weights, spacings, and axle speeds as well as the GVW yielded comparable results. More detailed studies will need to be conducted in order to consider a number

69

of parameters that would influence the performance of the BWIM system. For instance, the spread of the load from the surface of the deck to the rosette level is considered to be direct in relating the measurements to the computation of the axle weights. More detailed studies need to be performed to confirm the assumption, although the calibration parameter, α, may have already embodied the total effect. Other factors influencing the performance of the system are the bridge type and size as well as the stiffness of the bridge.

Chapter III: Virtual Reference Approach for Dynamic Distributed Sensing of Damage in Large Structures

The materials of current chapter are partially submitted with the following citation: "Virtual Reference Approach for Dynamic Distributed Sensing of Damage in Large Structures" by Babanajad, S.K., Zhan, Y., Taylor, T., and Ansari, F. Journal of Aerospace Eng, ASCE, under review
Please refer to the authors' contributions in page iv in the beginning of this document for details of contributions.

3.1. Introduction

As earlier discussed in Chapter 1, the advent of optical fiber sensors provided opportunities for large scale monitoring of structures. Among the fiber optic sensors, latest technological developments in distributed sensing with optical fibers based on Brillouin Scattering effect have provided new capabilities for enhancing the range and sensing capabilities on various aspects of structural health monitoring. Despite the obvious advantages, distributed sensing has not gained widespread usage in structural health monitoring. This is due to the fact that sensing with Brillouin sensors involves a two-step process, requiring two measurements capturing the before and after damage states of the structure. The difference between the two measurements reveals the location of the damaged sections. This requirement limits the practical application of the Brillouin technology only to circumstances: (a) where reference Brillouin data for the structure is available, i.e. acquired at the original undamaged state when the structure was just built; or (b) during load tests, where the Brillouin data at each load stage is compared with data from the previous stage. In essence, in the absence of reference measurements, the technology falls short in real time detection of existing structural defects.

The objective of the research in current chapter is to formulate a reference-free distributed detection method in order to locate the defects that occur in structures under in-service operating conditions. The proposed methodology was primarily established based on the Pulse-Pre-pump Brillouin Optical Time Domain Analysis (PPP-BOTDA) method. To sense the structural perturbations corresponding to the in-service operations, i.e. aircrafts vibration during flights or bridges subjected to traffic induced vibration, the dynamic measurement capability of the PPP-BOTDA has been employed. The advantage of the method developed in this study is that it enables the structure to be monitored at any stage during its service life without the need for prior reference data. Fundamentally, the method enables simultaneous detection of multitudes of over large sections of structural systems. Detailed description of the operational principles pertaining to dynamic distributed monitoring with PPP-BOTDA is already given in the Chapter 1.

3.2. Proposed Methodology

The method is described by considering the dynamic motion of the beam shown in Fig. 3.1. The beam could be represented as any structural component such as a bridge girder vibrated due to the traffic passage, or stiffening element of a fuselage during flight, etc. It is further considered that the beam has incurred damage in the form of two small defects. In the experiments the two defects were designed by splicing three wide flange sections to form a 15 meter long beam. The bolts in the spliced sections could be manipulated to show various magnitudes of displacements due to opening of defects under dynamic loads at either one or both joints. They could be also tightened to

represent an intact beam without defects. The beam dimensions and the locations of the two defects and support locations are schematically provided in Figs. 3.1a, 3.1b and 3.1c. Fig. 3.1d shows the actual beam in the loading frame. Beam oscillation is induced by releasing the beam mid-span after lifting it to a predefined height. As shown in Figs. 3.1c and 3.1d, the vertical movement of the beam at the two supports is prevented by the frame assembly. The optical fiber was pre-tensioned to a prescribed level and adhered along the entire 15-meter length of the beam. This procedure assures that the fiber remains in tension during load cycles. As shown in Fig. 3.1a and 3.1d, the sensor was placed on the top surface for ease of operations during the laboratory experiments. It was then connected to a AT-BOTDA device.
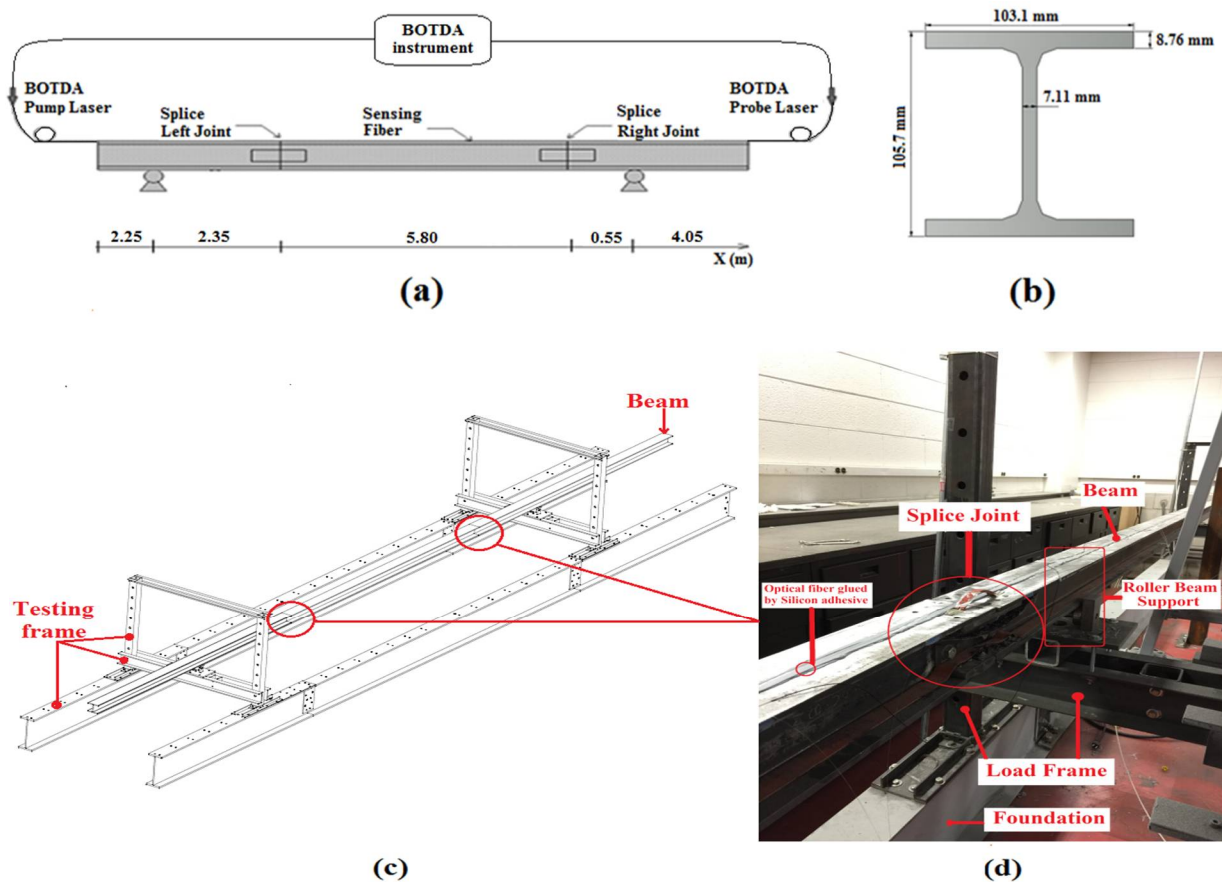
Figure 3.1 a) Beam layout, b) beam cross section details, c) schematic view, d) actual beam in the loading frame

The experimental program involved oscillating the beam and recording the distributed dynamic strain data along the length of the beam. Following acquisition of frequency shift data in distance and time domains, Eq. (1) from Chapter 1 was employed in order to convert the measured frequency shifts to strains. The BOTDA measured data pertained to spatial distribution of strain in time domain, providing a three dimensional (3-D) representation of the dynamic strain distribution of the structural system during the sampling period. Fig. 3.2 pertains to the response of the beam as acquired by the AT-BOTDA. In the 3-D response spectrum of Fig. 3.2, the vertical axis is the strain amplitude, the horizontal axis corresponds to the distance along the beam length, and the transverse axis represents time. As shown in Fig. 3.1a, fifty meters of optical fiber made a closed loop connection between instrumented beam and BTODA measurement unit. BOTDA was configured to measure the strain at 5 cm sampling intervals. Therefore, for the 15-meter length of the optical fiber attached to the beam, 300 points were measured at any instance of measurement. A sampling frequency of 13 Hz was employed by the BOTDA. Therefore, for one second of dynamic tests, 3900 data points were acquired. The time domain data is employed to extract and separate the base strain that pertains to the flexural response of the beam due to the dynamic load from the additional strain sensed at the defect locations. In essence, the segments of the optical fiber sensor that span over the defects are subjected to additional localized strain discontinuities. From the 3-D strain profile shown in Fig. 3.2, the location of any of the two existing defects could be located. In addition to the induced strain due to opening of the defects in the optical fiber, ε_C, the strain response of the beam with defects, ε_D, is influenced by the dynamic load, system noise, temperature, and the pre-

tensioning strain in the fiber. The strain response of the beam with a defect is generally described by the following relationship:

$$\varepsilon_D = \varepsilon_L + \varepsilon_{Tf} + \varepsilon_{Ts} + \varepsilon_{PT} + \varepsilon_N + \varepsilon_C \qquad \text{(Eq. 1)}$$

Where, $\varepsilon_L, \varepsilon_{Tf}, \varepsilon_{Ts}, \varepsilon_{PT},$ and ε_N pertain to the flexural strain in the beam due to dynamic load, temperature induced strain in fiber, temperature induced strain in structure, residual strain in the fiber due to pre-tensioning, and noise. As shown in Fig. 3.2, without the reference data, it will not be possible to detect the location of the defects from the strain profile. The other strain terms in Eq. (1), intrinsically mask the strain generated from the opening of the defects. Therefore, it will be necessary to eliminate as much the effects of the other strain components from the signal in order to differentiate the influence of the defects.
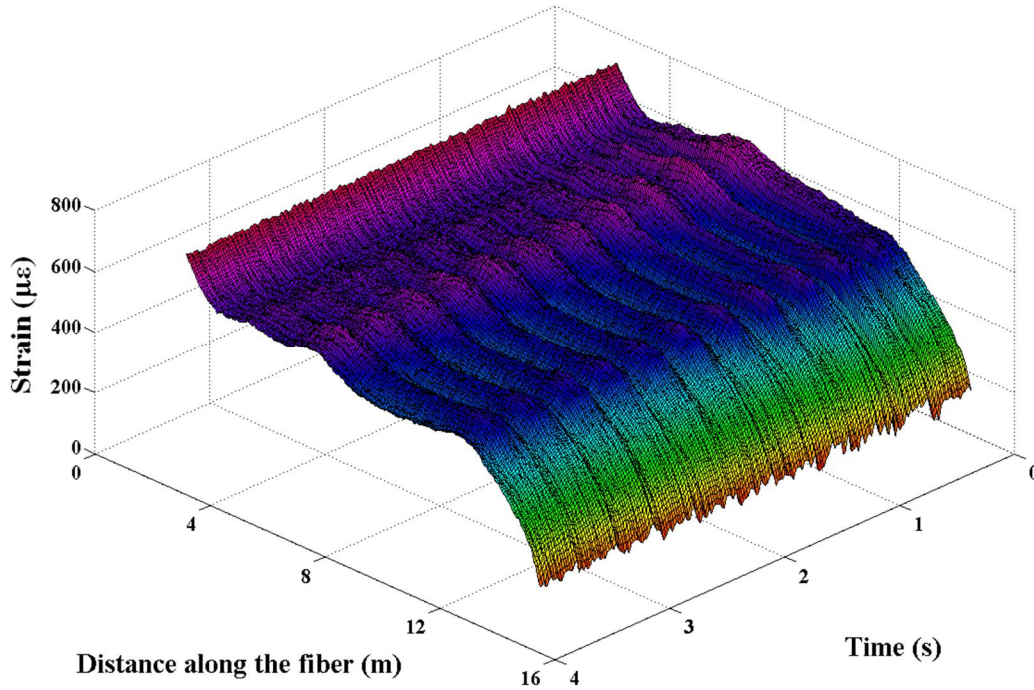
Figure 3.2 The 3-D time domain distributed strain response of BOTDA

In general, the effect of thermal strains in distributed fiber sensing (ε_{Tf}) is compensated by use of a loose fiber in parallel with the strain sensor. The same approach was

75

employed in the present experiments. For dynamic strains, however, the structure is not influenced by thermally induced strains (ε_{Ts}), since for all practical purposes, under normal conditions, the temperature does not change over a very short time interval. The effect of residual strain due to Pre-tensioning of the optical fiber is difficult to differentiate because of its non-uniformity along the beam length. The smooth curved shaped response of the strain signal in Fig. 3.2 is attributed to the non-uniform nature of this strain. It will influence the global dynamic shape of the beam oscillations. The system noise in the AT-BOTDA system is an inherent characteristic of the device. The noise level is larger at higher spatial resolution levels.

Flexural Strain caused by the Dynamic load (ε_L): the vertical oscillations of the beam generates distributed flexural strain (ε_L). For a continuous Euler-Bernoulli beam, the governing load-displacement equation of motion can be written as:

$$m_{(x)}\frac{\partial^2 u(x,t)}{\partial t^2} + EI_{(x)}\frac{\partial^4 u(x,t)}{\partial t^4} = F_{(x,t)} \qquad\qquad\qquad (Eq.\, 2)$$

Where, E and I are the Young's modulus, and the moment of inertia of the section, respectively. $u_{(x,t)}$ is the deflection profile for the neutral axis of the beam at each instance t, and m is mass of the structure per unit length. $F_{(x,t)}$, is the applied external dynamic force on the structure. Since solving Eq. (2) is complex for many structural elements, therefore, Multi Degree of Freedom systems have been introduced to descretize continuous systems in order to easily find the solution (Chopra 2011). Chopra (2011) has stated that discretized systems are ideal for computer implementation in order to solve the differential equations governing the motion of the structures. Eq. (2) is discretized and converted to a multi degree of freedom system.

Therefore, modal representation of Eq. (2) is given by the following relationship (Chopra 2011):

$$[M]\{\ddot{q}\} + [C]\{\dot{q}\} + [K]\{q\} = \{F_{(x,t)}\} \qquad \text{(Eq. 3)}$$

Where, [M], [K], [C], [F], and q, represent, the global mass, stiffness, damping, force and modal displacement terms. By using the Modal Expansion Method the displacement term can be individually calculated for each Degree of Freedom (DOF), n, which is expressed by:

$$\ddot{q}_n(t) + 2\xi_n. \omega_n. \dot{q}_n(t) + \omega_n^2. q_n(t) = \frac{F_n(x,t)}{M_n} \qquad \text{(Eq. 4)}$$

Where $q_n(t)$, ξ_n, ω_n, and M_n respectively correspond to n^{th} modal displacement, damping ration, angular frequency, and mass terms. It should be noted that n represents the total number of modes which is equal to total number of degree of freedoms. Alternatively, by using Euler-Bernoulli beam theory, displacement term can be defined as of Eq. (5), in which $Z(x)$ denotes the distance of calculated longitudinal strain from the neutral axis along the cross section of beam at the location of x along the structure length.

$$\varepsilon(x,t) = -Z(x). \frac{\partial^2 u(x,t)}{\partial x^2} \qquad \text{(Eq. 5)}$$

Where $\varepsilon(x,t)$ and $u(x,t)$ respectively denote the flexural strain and total displacement terms at the location of x along the structure length at the instance of t during vibration loading. By combining Eq. (4) and (5), the dynamic flexural strain of the beam is expressed by:

$$\varepsilon(x,t)_L = -Z(x). \left(\sum_{n=1}^{N} \{\varphi_n\}. \ddot{q}_n(t) \right)_x \qquad \text{(Eq. 6)}$$

φ is the matrix containing the modes. The flexural strain described in Eq. (6) does not embody the effect of defects along the length of the beam.

Strain caused by the opening of the defect (ε_C): the mechanism of strain transfer from the structure surface to the sensing fiber core has been examined in a number of studies. Ansari and Libo (1994) introduced a shear transfer model to analyze the development length of the sensing fiber considering interface characteristics. Wan et al. (2008) concluded that the analytical models are valid for small shear lag factors. Feng et al. (2013) introduced a crack into the shear lag model based on compatibility in the displacement field to calculate induced strain in the fiber core. Motamedi et al. (2012) quantified the effect of defect opening displacements on the distributed strains obtained from BOTDR measurements. Imai and Feng (2012) introduced a softening model for the surrounding materials including the polymeric coating of optical fiber and the adhesive, and the analytical model was confirmed by experimental results using different sensing fiber installations.

3.2.1. Reference Free Damage Detection Approach

Since it is not possible to make reference measurements for structures that have already developed defects, but still in-service, the goal will be to establish reference from the measured dynamic distributed signal. This necessitates differentiating the influence of other strains from the defect induced strains. Based on the aforementioned discussions, for small defect opening displacements, the amplitude of strain profile at any instant of time is responsible for the global flexural displacement of the beam. Fig. 3.3 represents the one second response (totally 13 measurements) of the oscillating

beam. The effect of the global dynamic behavior of the beam is comingled with the effect of fiber pre-tensioning. Considering that the thermal effects have been already eliminated, only the system noise and defect opening displacements are considered superimposed on the flexural response. Fig. 3.4 is the 2-D transformation of Fig. 3.3 for a typical instant of time. It pertains to strain distribution only over a small segment of the beam within the time duration of $\frac{1}{13} \approx 0.08$ seconds. The response shown in this figure refers to the data points inside a small segment of the beam, ΔL. Fig. 3.4a represents the beam in the damaged state, and Fig. 3.4b pertains to the same beam in undamaged state without a defect. As shown, the effects of small defects on strain distribution are very minute and ordinarily considered as system noise. It is however, possible to establish the reference base from this data by regression analysis even in the presence of the system noise and small defects. The dashed lines in Figs. 3.4a and 3.4b pertain to the results from regression analysis directly developed from the damaged and or undamaged states of the beam. Considering that the objective is to detect small defects (i.e., 50 microns), then it can be hypothesized that the regression lines for the flexural strain data acquired from undamaged and damaged states of the beam are sufficiently close to be considered the same. Then, in lieu of the reference signal, which is the regression line to the undamaged strain data, it is practically possible to consider the regression line for the beam with small defects in Fig. 3.4a as the reference signal. Both regression lines contain the effects of signal noise, but the regression line in Fig. 3.4a, also contains the effects of defects. Once these two signals are subtracted from each other, it is possible to discern the influence of the defects from the strain response, which is shown in Fig. 3.4c. The regression line achieved this way, can be considered

79

as a virtual reference strain signal. The mathematical processes leading to the formulation of reference signal is based on the regression analysis of data.
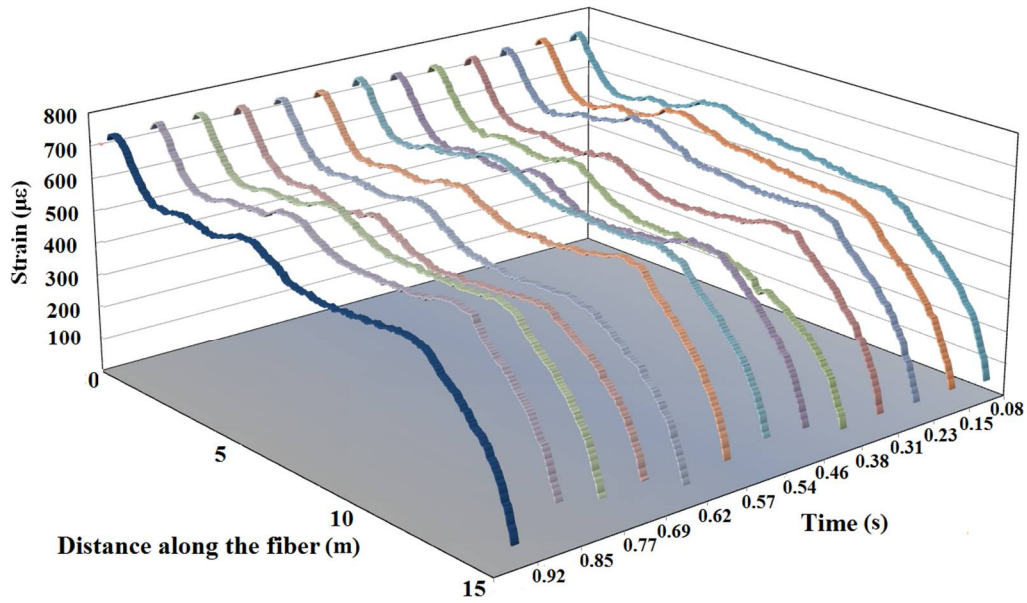
(a)
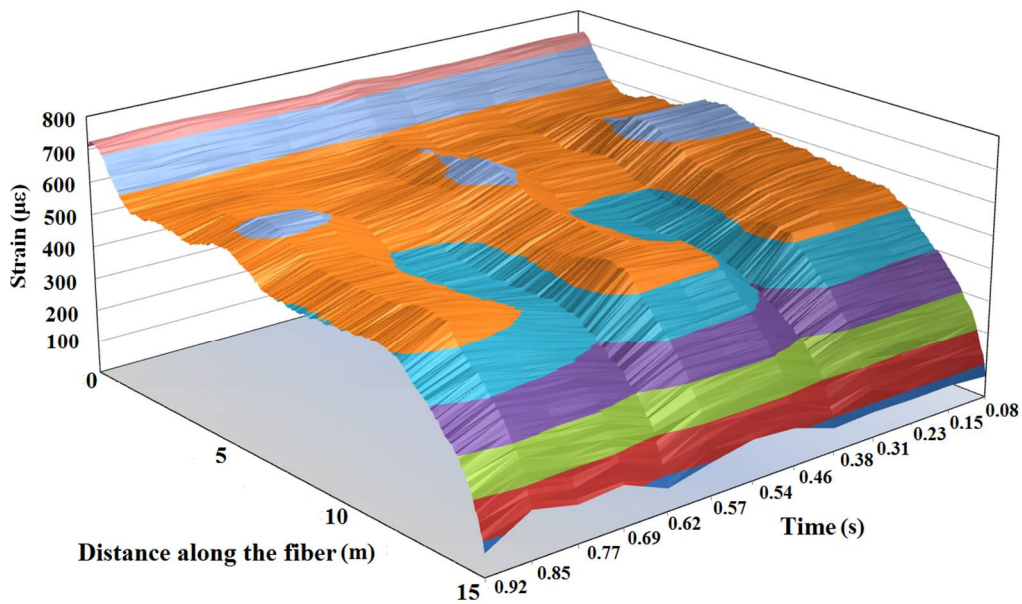
(b)

Figure 3.3 The 3-D response of the AT-BOTDA a) in discrete view, b) in continuous view
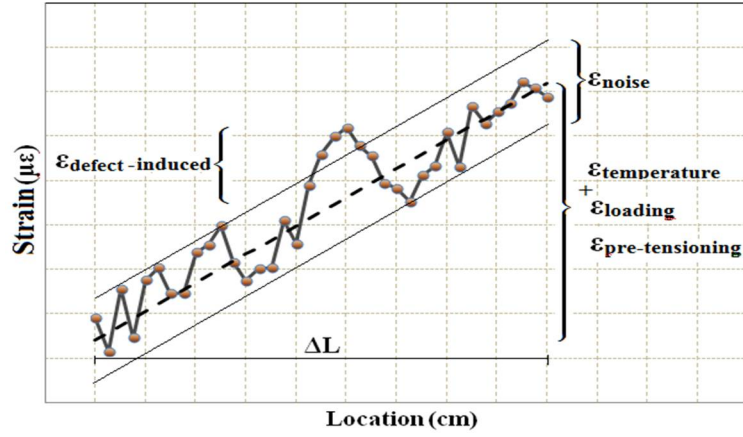
a) Damaged Structure
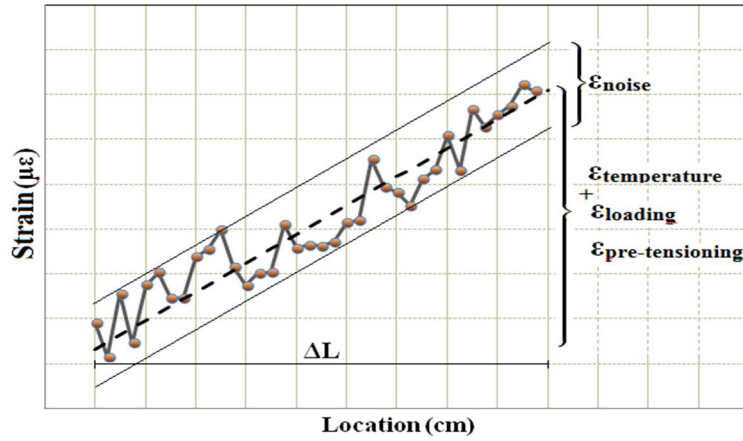
b) Undamaged Structure
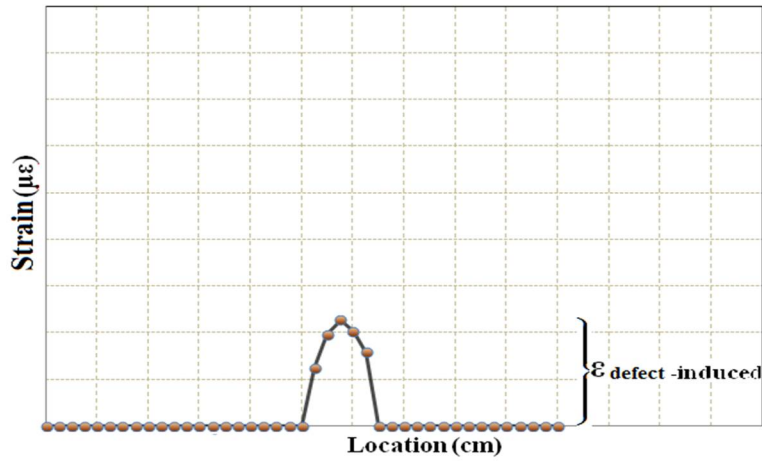
c) The detected defect based on
the virtual reference line

Figure 3.4 Formulation of virtual reference over damaged or undamaged segments of the structure

81

Regression analysis is highly dependent on the selection of the function, φ_k, to represent the strain distribution. Polynomials and exponential functions including spline or Bezier curves can be employed for this purpose (Gu et al. 2009). Selection of the function is dependent on the strain response. Considering that a polynomial can arbitrarily approach any continuous function, for the distributed strain data acquired in the present study, the generalized function is given by:

$$\{\varphi_0, \varphi_1, \varphi_2, \dots, \varphi_n\} = \{1, x, x^2, \dots, x^n\} \qquad \text{(Eq. 7)}$$

And the polynomial approximation is:

$$\varepsilon^*_{(x)} = a_0^* + a_1^* . x + a_2^* . x^2 + \cdots + a_n^* . x^n = \sum_{m=0}^{n} a_m^* . x^m \qquad \text{(Eq. 8)}$$

Where, $(a_0^*, a_1^*, a_2^*, \dots, a_n^*)$, n, and x respectively denote a coefficient set of least error, degree of polynomial, and location along the fiber. $\varepsilon^*_{(x)}$ is the estimated strains at the location of x along the optical fiber. Then, the normal equation set is established as:

$$\begin{bmatrix} \sum_{j=1}^{k} w_j & \sum_{j=1}^{k} w_j . x_j & \cdots & \sum_{j=1}^{k} w_j . x_j^n \\ \vdots & \ddots & & \vdots \\ \sum_{j=1}^{k} w_j . x_j^n & \sum_{j=1}^{k} w_j . x_j^{n+1} & \cdots & \sum_{j=1}^{k} w_j . x_j^{2n} \end{bmatrix} \begin{bmatrix} a_0^* \\ \vdots \\ \vdots \\ \vdots \\ a_n^* \end{bmatrix} = \begin{bmatrix} \sum_{j=1}^{k} w_j . \varepsilon_j \\ \vdots \\ \sum_{j=1}^{k} w_j . x_j^n . \varepsilon_j \end{bmatrix} \qquad \text{(Eq. 9)}$$

Where, $\varepsilon_{(j)}$ corresponds to the measured strain response obtained from the BOTDA measurements. w_j refers to the weight function, $w_j = w_{(x_j)}$ $(j = 1, 2, \dots, k)$. k is the total number of data points inside the specified ΔL intervals selected along the beam length as shown in Fig. 3.5. In order to choose the right value of n, a trial and error has to be performed on the results. In this study, where the experiments involved a determinate beam, the flexural strain is linearly distributed over the length of the structure.

Therefore, the linear regression method ($n = 1$) was used to fit the data. Eq. (10) represents the general form of the linear regression function employed herein. Using the coefficient of determination indicator (R^2), the performance of regression analysis can be estimated. For the present experiments, R^2 were above 0.93.

$$\varepsilon^*_{(x)} = a^*_0 + a^*_1 . x \qquad\qquad\qquad\qquad (Eq. 10)$$

Once the reference line is fitted and formulated for ΔL_i with the center at L_i, the virtual flexural strain (ε^*_i) is calculated again for the L^{th}_i data point using the Eq. (8) estimated formula. By sweeping the ΔL_i with the center at L_i for all data points (different sets of i) along the beam and continuing fitting the regression line for each ΔL_i, the virtual strain response (ε^*_i) is constructed. As discussed earlier, the difference between the measured data and the virtual reference response will result in only the response of defect-induced strain. The sweeping regression line approach is diagrammatically described in Fig. 3.5a. The virtual reference strain constructed in this manner is shown in Fig. 3.5b. In implementing this approach, the choice of the window size (ΔL) along the beam depends on the location of supports at which the stress concentration may require a smaller window size (ΔL).
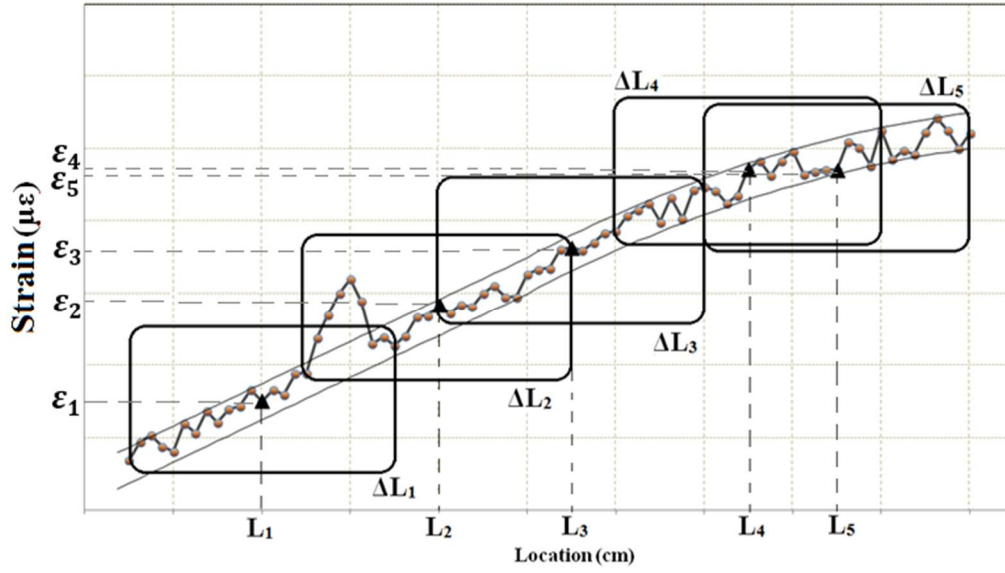
a) Damaged Structure Response
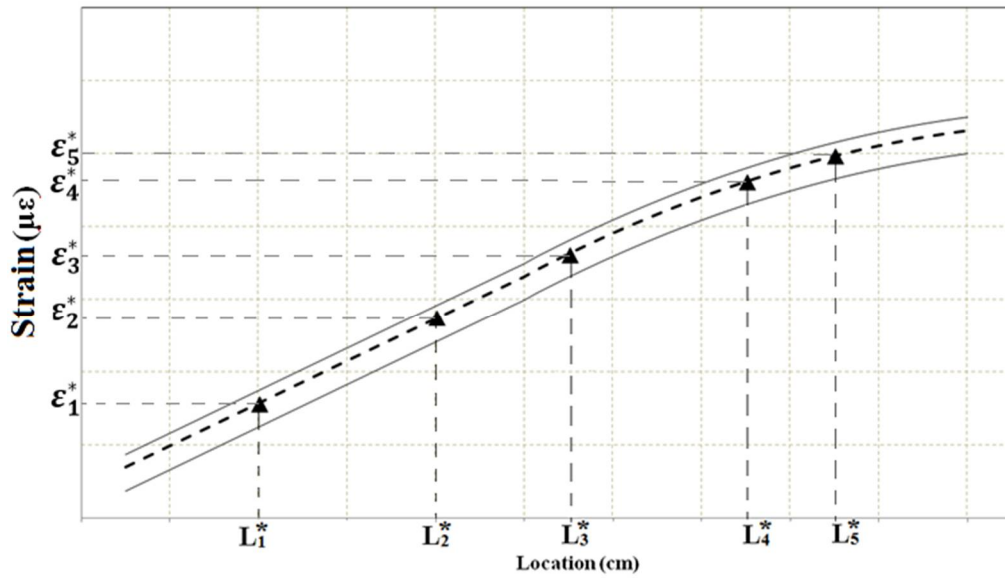
b) Constructed Virtual Undamaged Structure Response

Figure 3.5 Sweeping the ΔL interval along the structure length

Selection of the best ΔL depends on several factors including the damage area (L_D), total beam span length (L_T), and spatial resolution (SR). As the damage area (L_D) increases the damage-affected zone distributes along a longer length of the beam which mandates extending the ΔL range. However, as the ΔL range increases the accuracy of the method decreases since the loading profile is changed with more rate

along the ΔL range. A similar case is valid for the total beam span length (L_T), however, the $\Delta L/L_T$ is a more governing factor than the absolute value of L_T. In other words, as the $\Delta L/L_T$ is kept small the results fall into an acceptable levels of accuracy and reliability. With a higher L_T, even if the ΔL range increases the results will not be as affected since the loading profile is only changed slightly along the ΔL range. Therefore, the $\Delta L/L_T$ rate must be more crucial than solely monitoring L_T or ΔL. Alternatively, as previously pointed out the spatial resolution is an inherit feature of the BOTDA sensing device. Spatial resolution of a sensing set up is a representative of the distance that the measurement value indicates. It is obvious that the measured response by the sensing device at any location does not represent the actual corresponding response. Therefore, as the spatial resolution decreases, the accuracy of measurement increases. However, low SR measurements add more noise to the response. In order to locate the best trade-off between accuracy and noise level, a trial & error operation has to be performed. The strain measurement in each sampling point (x) is the representative of strain measurement within the distance range of $(x - SR/2 : x + SR/2)$ along the beam length, therefore, the ΔL range has to be greater than the spatial resolution. With all this in mind, in order to find the best ΔL range, the trade-off among the L_D, L_T ($\Delta L/L_T$), SR, and noise levels have to obtained for any experimental program. For the case of the present experimented steel beam, ΔL has been finalized as 50 cm, $L_D = 0.5$ mm, L_T (middle span length) $= 10$ m ($\Delta L/L_T = 0.05$), and SR $= 20$ cm. The flowchart addressing the stepped procedures for acquiring the virtual reference as well as the final defect induced response is shown in Fig. 3.6.
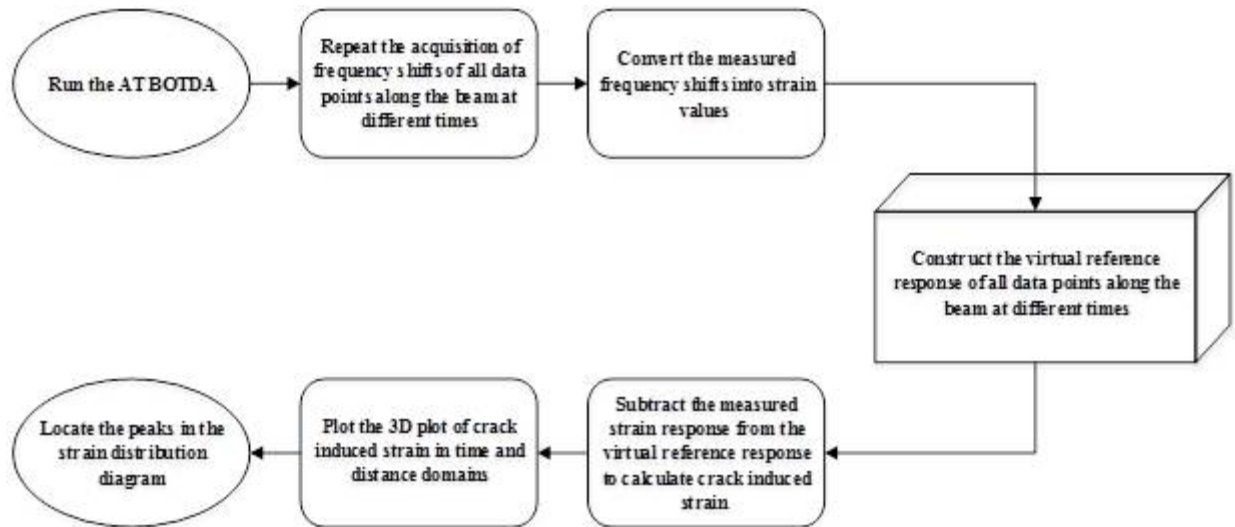
Figure 3.6 Flowchart representing the proposed reference free method

3.4. Experimental Results and Discussions

The experimental program involved testing of a long steel beam that embodied two fabricated defects. Loading was induced in the form of free vibrations. The beam was oscillated by lifting the beam mid-span by 9 mm and then releasing it. The objective was to examine the defect detection capability, both in terms of the resolution of the measurements as well as location detection.

Different damage levels (DL) were introduced in the beam in order to simulate the defect initiation and growth, and to determine the extent of detectable damage by the proposed approach. The level of damage and its severity were possible to be manipulated by tightening or loosening the bolts at the gusset plates. Fig. 3.7 depicts a typical gusset plate connection at the spliced joint. An arch type FBG-based displacement sensor was independently installed at the spliced joint location to measure the defect opening displacements during the dynamic vibration. Details regarding the FBG based displacement sensor can be found elsewhere (Bassam et al. 2011;

Iranmanesh and Ansari 2014). Table 3.1 corresponds to the experimental program for the range of damage levels, and defect opening displacements considered in the present study.

(a) Top view   (b) Side view
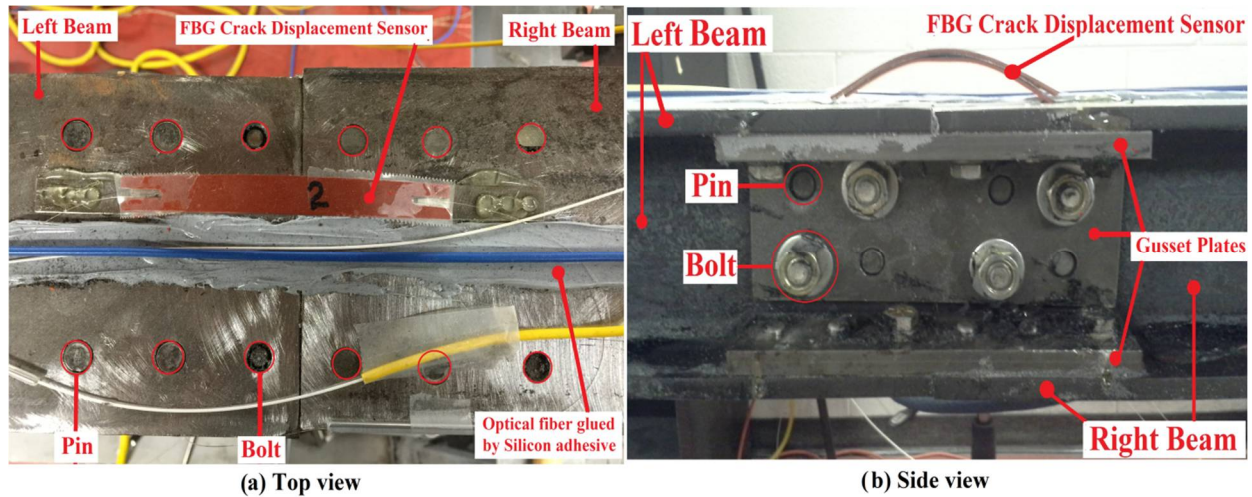
Figure 3.7 Spliced joint connection in details

Table 3.1 Summary of Damage Levels (DLs) for free vibration tests

Level of Damage	Left Joint Max Opening (μmm)	Right Joint Max Opening (μmm)
DL#0	30	30
DL#1	30	60
DL#2	35	120
DL#3	35	125
DL#4	50	120
DL#5	220	130
DL#6	300	160
DL#7	320	220
DL#8	350	240
DL#9	550	280

The undamaged state (intact) of the beam pertained to the condition where all the bolts at the spliced joints were fully tightened. For the intact condition (DL0 in Table 3.1), even though all the bolts were tightened, the defects opened by as much as 30 microns during oscillations as demonstrated in Table 3.1. For this condition, formulations

presented in Eqs. (7-9) were employed in order to establish the virtual reference signal shown in Fig. 3.8a. Fig. 3.8b corresponds to the difference between the raw data obtained from the measured response in Fig. 3.2, and the virtual reference response in Fig. 3.8a. As shown in Fig. 3.8b, the difference is flat and does not show any strain singularities at the location of the defects. The resolution of the measurements was not sufficient to detect the defect opening displacements for DL0 in this case.

(a)

(b)
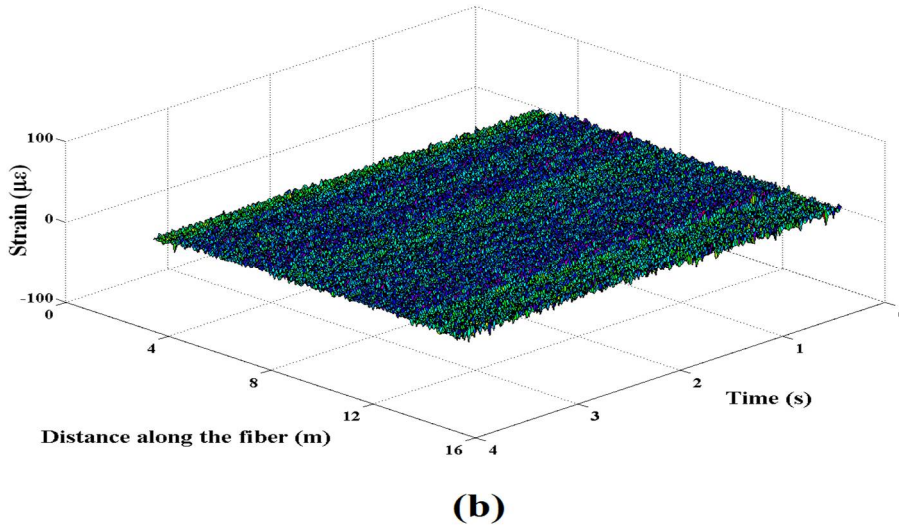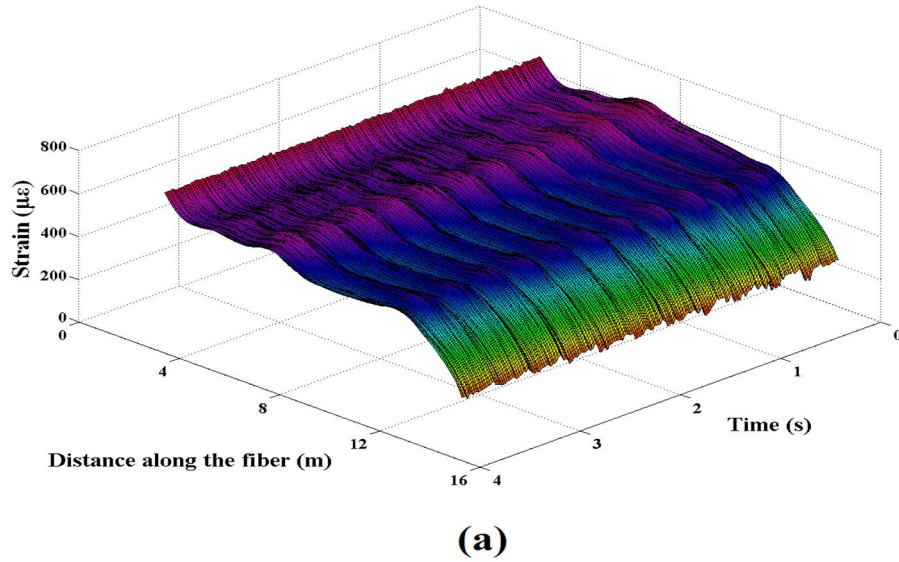
Figure 3.8 a) The virtual reference-free response in DL0, b) The defect-induced response in DL0

As discussed earlier, the level of damage was simulated by increasing the width of the defects at the spliced joints. Damage levels shown in Table 3.1 correspond to the opening displacements of the spliced joints following loosening of the bolts at each stage. The experiments were conducted in a sequential manner wherein damage levels DL1 through DL3 pertain to the progressive increase in defect size at the right joint (Fig. 3.1a). DL4 through DL6 correspond to progressive increase in the defect size at the left joint. During the experiments at the damage levels corresponding to DL4 through DL6, the amount of tension in the right side joint bolts remained at the DL3 level. Following these experiments, the right and left side joint bolts were simultaneously increased at three stages corresponding to the damage levels DL7 through DL9. An FBG based sensor was attached to the mid-span of the beam in order to determine the natural frequencies of the beam at each damage level. Fig. 3.9 pertains to typical frequency analysis of the time domain signals at each damage state. The first three modes for DL0 are apparent in Fig. 3.9. Natural frequency (NF) response of the beam for other damage states is shown in Table 3.2.

Table 3.2 Summary of the extracted first three natural frequencies

Damage	Natural Frequency (Hz)			Natural Frequency Difference (%)		
Levels	f_{n1}	f_{n2}	f_{n3}	f_{n1}	f_{n2}	f_{n3}
DL0	2.930	6.232	13.183	-	-	-
DL1	2.930	6.153	13.086	0.0	-1.3	-0.7
DL2	2.930	5.957	13.086	0.0	-4.4	-0.7
DL3	2.930	5.957	13.086	0.0	-4.4	-0.7
DL4	2.930	5.860	12.988	0.0	-6.0	-1.5
DL5	2.832	5.664	12.790	-3.3	-9.1	-3.0
DL6	2.832	5.566	12.790	-3.3	-10.7	-3.0
DL7	2.734	5.469	12.890	-6.7	-12.2	-2.2
DL8	2.734	5.459	12.890	-6.7	-12.4	-2.2
DL9	2.734	5.465	12.695	-6.7	-12.3	-3.7
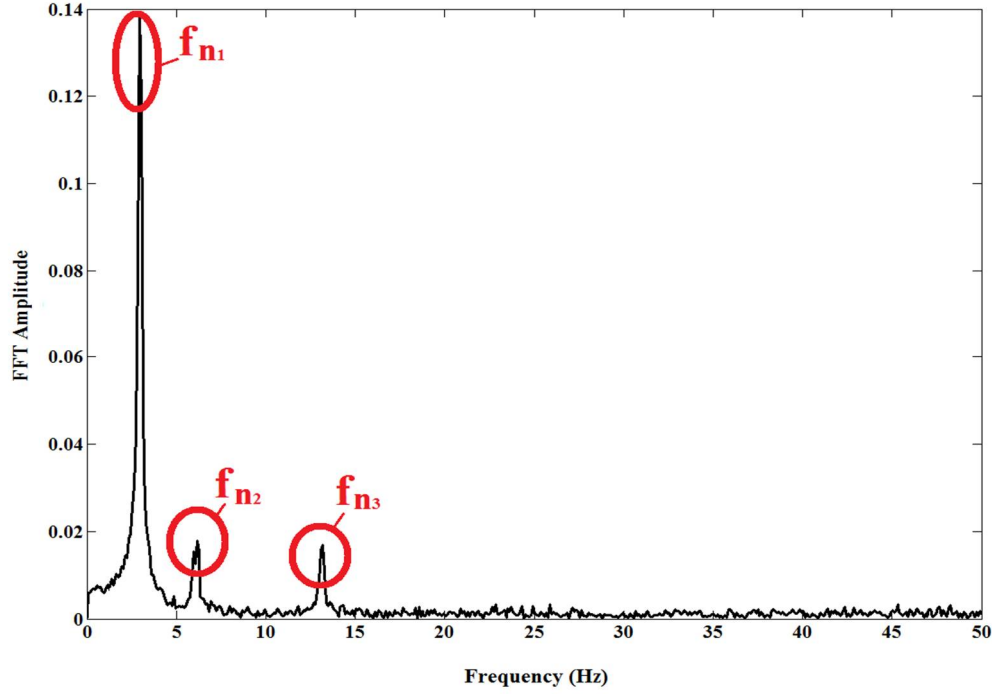
Figure 3.9 Typical FFT results of the free vibration tests measured by FBG-based sensor

Following acquisition of frequency shift data in distance and time domains, Eq. (1) in

Chapter 1 was employed in order to convert the measured frequency shifts to strains.

Then, regression analysis of strain data as formulated herein were employed in order to

acquire the crack induced strain response in time and spatial domains. To establish the

virtual references for all the damage scenarios, DL1 through DL9, Eqs. (7) through (9)

were again employed in transforming the raw experimental data to virtual references.

The virtual references obtained in this manner were compared with the raw

experimental data based on the vibration tests in order to evaluate the defect detection

capability of the method. The difference between the raw data obtained from BOTDA

measured response, and the virtual references for damage scenarios DL1 through DL3

are shown in Fig. 3.10. In a similar manner, Fig. 3.11 corresponds to the damage

scenarios DL4 through DL6, and damage scenarios DL7 through DL9 are represented

in Fig. 3.12.

As shown in Figs. 3.10a through 3.10c, the proposed method was capable of detecting the location of defect at the right joint due to progressive loosening of the bolts at the splice location. Displacements measured by the FBG displacement sensor at this joint indicated opening displacements of 60, 120, and 125 microns, respectively. The joint on the left side was not loosened and it only indicated the slight opening of the splice point due to the flexural vibration of the beam with opening displacements in the range of 30 to 35 microns for DL1 through DL3 damage scenarios. This level of damage was not detectable by the present approach. As shown in Table 3.2, for the three damage cases, DL1 through DL3, the first mode of vibration with respect to the intact condition (DL0) did not change. This is mainly due to the fact that the damage was not significant to change the first dominant natural frequency. The second and third modes changed due to the location of the defect on the right side with larger opening displacements. The second and third modes respectively had 1.3% and 0.7% decreases for DL1 indicating the loss of beam stiffness caused by partially releasing the right joint. During DL2, the second and third modes respectively had 4.4% and 0.7% decreases compared to the undamaged condition of the beam at DL0. In comparison to DL1, DL2 produced a 3.2% decrease in the second natural frequency while the third remained unchanged. Later on in DL3, the right joint's web was also partially released in addition to fully releasing the joint's top flange to simulate the development of the defect along the structure depth. This kind of defect development is seen more in structural elements experiencing flexural moments or vibrations such as beams, girders, etc. During DL3 there were 0%, 4.4%, and 0.7% decreases (related to DL0) in first, second, and third NFs, respectively. Compared to DL2, there were no changes in the NFs of DL3.
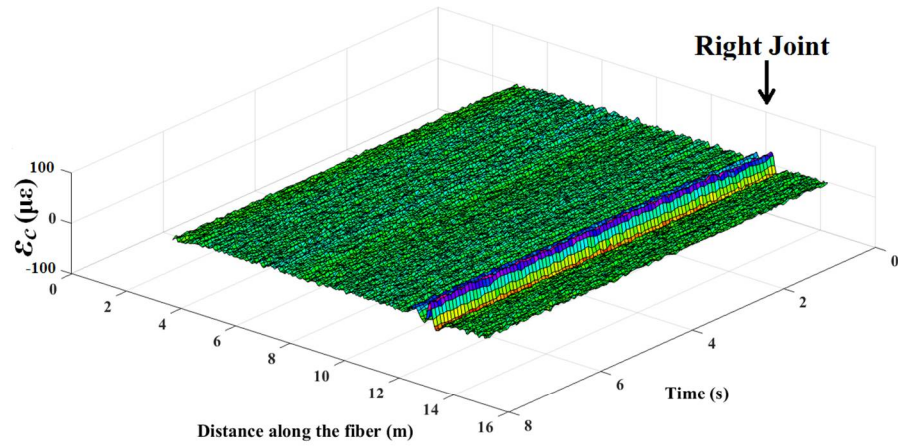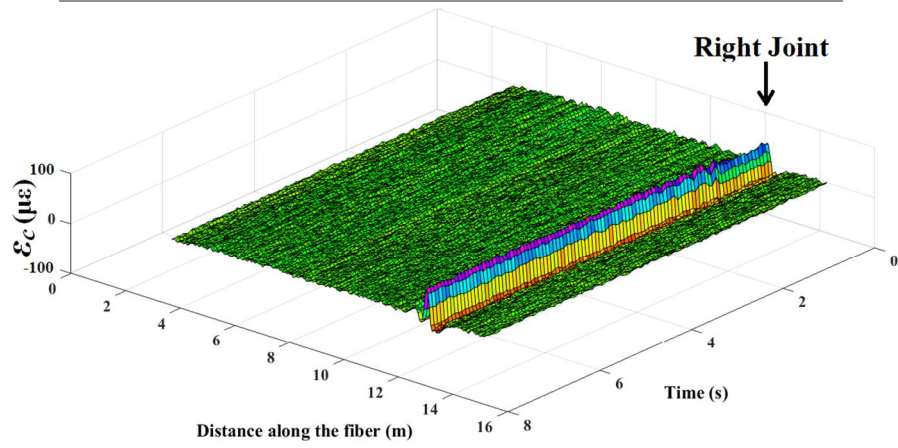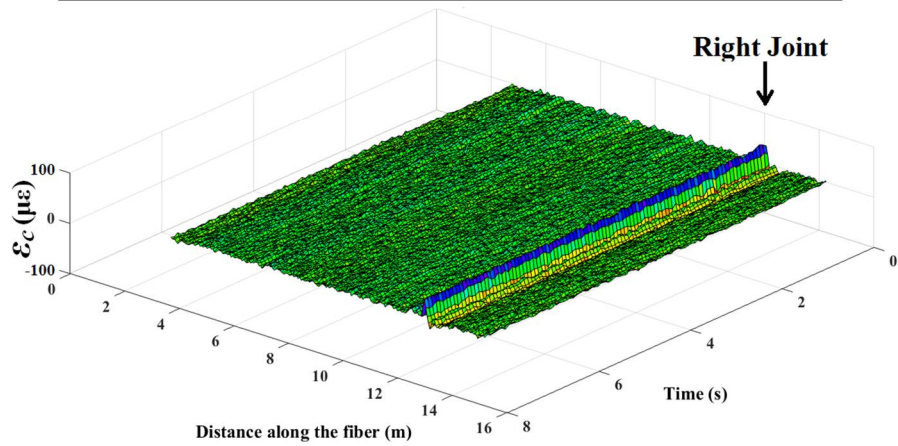
Figure 3.10 Defect induced response in: a) DL1, b) DL2, and c) DL3

In Fig. 3.11 where the experiments involved gradual increase in the opening displacements of the left side joint, it was possible to detect the opening displacements of the defects on both sides of the beam. As shown in Fig. 3.11a, despite the low amplitude of the strain profile, the system was able to pick up the 50 micron opening displacement of the left side, as well as the 120 micron displacement of the defect on the right side of the beam. It was also possible to qualitatively correlate the severity of left side joint damage to the strain amplitudes, because of the large difference in the defect opening displacements from 50 to 220, and then 300 microns in DL4, DL5, and DL6, respectively. During these experiments, the bolts on the right side splice were not physically adjusted. However, the additional opening displacements on this side are due to the influence of the left joint opening displacements on the overall flexural response of the beam. As indicated in Table 3.2, the slight opening displacement of the left joint in DL4 was not sufficient to change the first mode of the vibration. However, DL5 and DL6 opening displacements affected the fundamental mode. During DL4 there were 0%, 6%, and 1.5% loss in first, second, and third NFs in comparison with the undamaged condition of the structure at DL0. It is also notable that damage development from DL4 to DL5 has caused considerable (3.3%) loss in the first natural frequency denoting the greater influence of the left joint in the dominant first mode shape. The reason is primarily due to the fact that the left joint is placed closer to the middle of the beam where the first dominant mode shape could be affected more pronouncedly. In contrast, the right joint is located near the support resulting in smaller excitement of the first mode. From the transition of DL5 to DL6, only the second NF has been slightly changed.
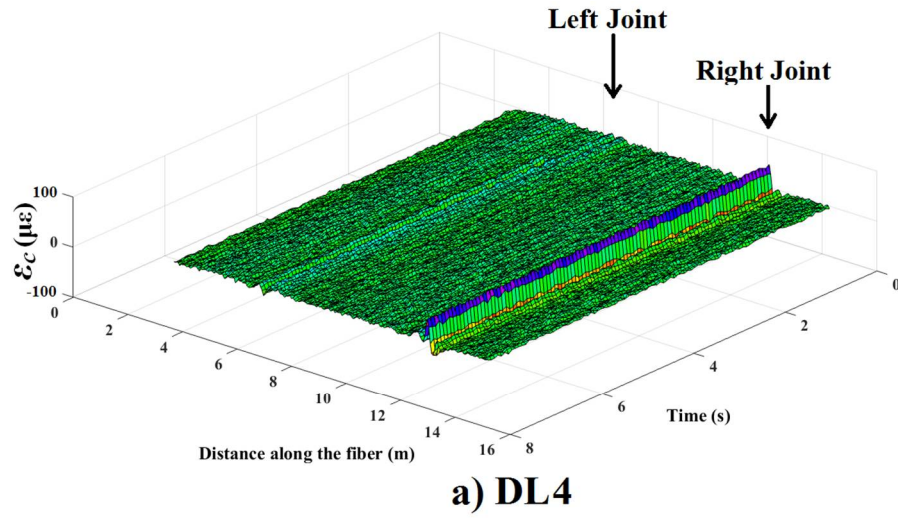
Figure 3.11 Defect induced response in: a) DL4, b) DL5, and c) DL6

Results shown in Fig. 3.12 pertain to the damage states during the DL7-9 where both joints experience further increase in their opening displacements. In these DLs, both left and right joints were simultaneously released to reach the maximum damage level. DL9 denotes the condition of the beam with the maximum amount of damage for both joints (left joint: 550 microns, right joint: 280 microns), where the top flange and web of both joints were completely released and only the bottom flanges were carrying out the integrity of beam at the joint locations. Compared to DL0, there were 6.7%, 12.3%, and 3.7% respective decreases in first, second, and third NFs of DL9 indicating the maximum damage level applied to the beam. Needless to say that the effect of larger opening displacements culminated to larger strain intensities at the defect locations. They also influenced all three modes of vibrations as shown in Table 3.2. It was also possible to qualitatively correlate the defect opening displacements to the strain intensities. As shown in Fig. 3.13, the dynamic strain based on the response of AT-BOTDA and the FBG displacement sensor at the left joint defect location are for all practical purposes in phase. Only qualitative quantification of the defect opening displacements by AT-BOTDA are possible at this time, because the strain transfer mechanism of the optical fiber extends beyond the defect zone. The spatial resolution of the BOTDA complicates direct correlation of strain and displacement in this case.
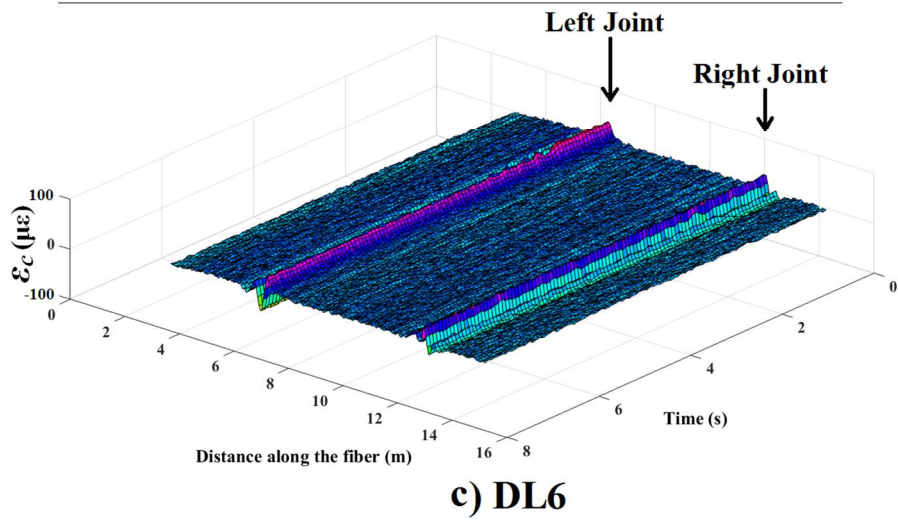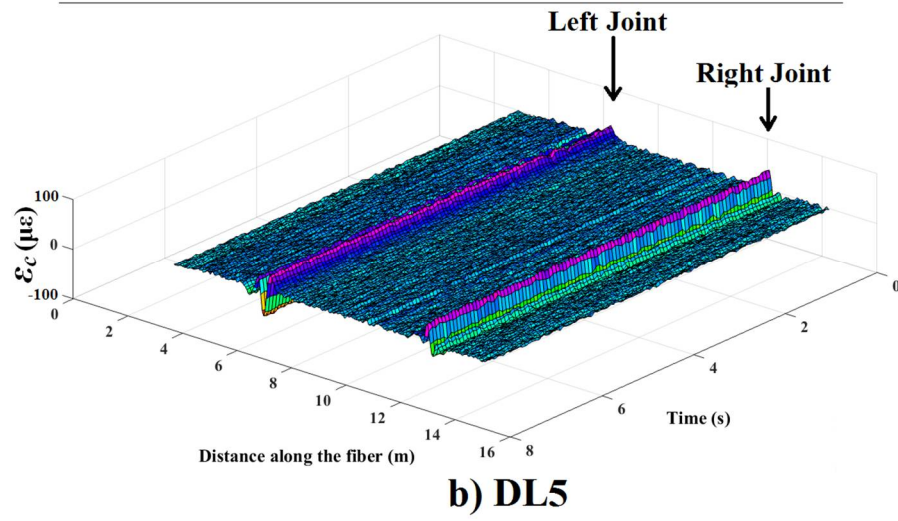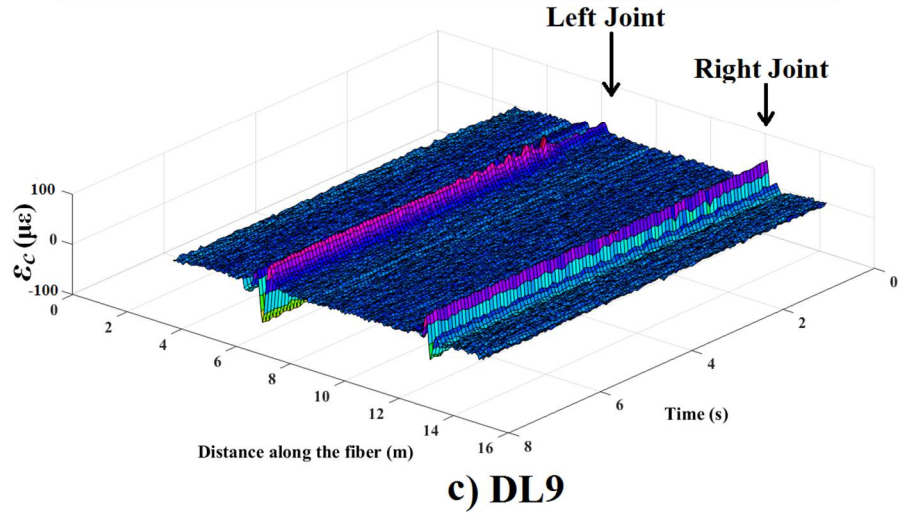
Figure 3.12 Defect induced response in: a) DL7, b) DL8, and c) DL9

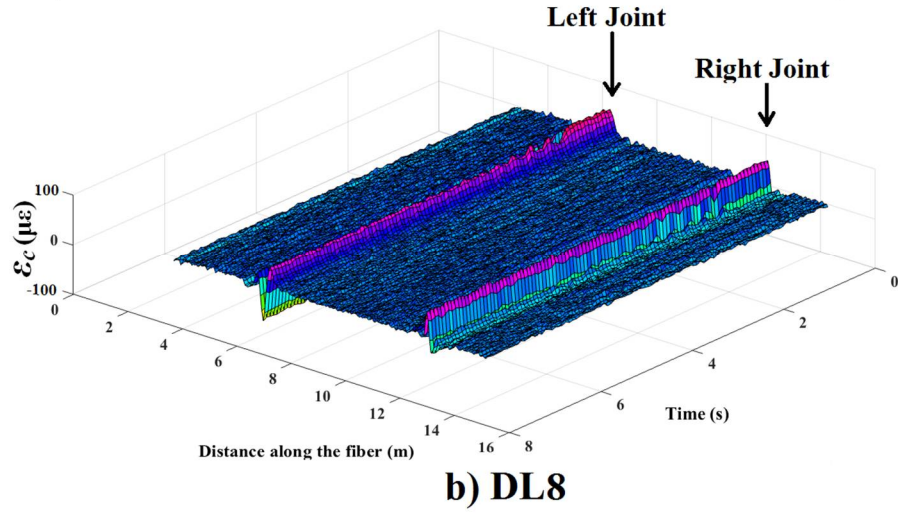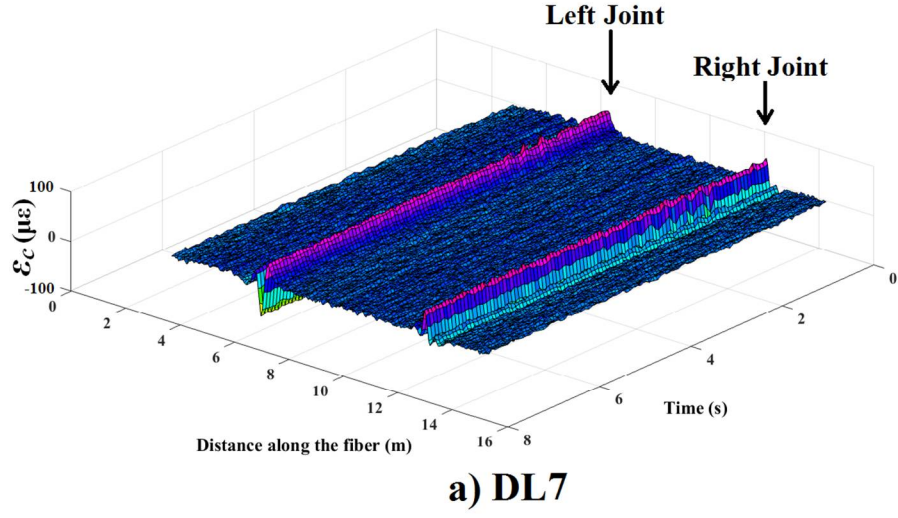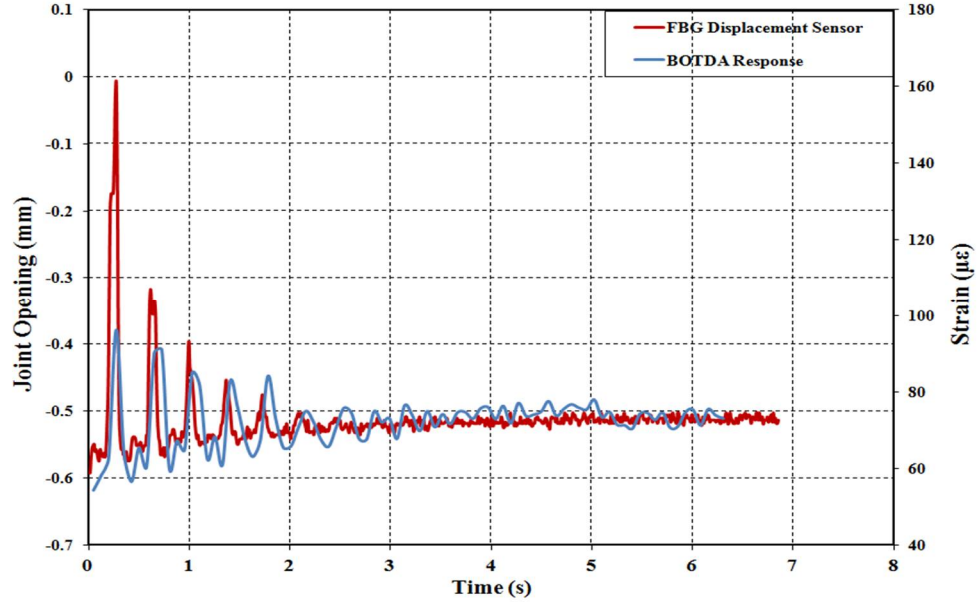**Figure 3.13 The comparison between the responses of BOTDA and FBG displacement sensors; Left joint; DL9**

3.5. Summary of the chapter

In the research described herein formulations and experiments pertaining to a reference-free distributed strain monitoring approach was introduced in order to detect the locations of small defects in structures under in-service operating conditions. The proposed methodology was primarily established based on the Pulse-Pre-pump Brillouin Optical Time Domain Analysis (PPP-BOTDA) method. To sense the structural perturbations corresponding to the in-service operations, i.e. aircrafts vibration during flights or bridges subjected to traffic induced vibration, the dynamic measurement capability of the PPP-BOTDA has been employed. The advantage of the method developed in this study is that it enables the structure to be monitored at any stage during its service life without the need for prior reference data. Fundamentally, the method enables simultaneous detection of many existing small size defects (i.e. 50

microns) over large sections of structural systems. Since the detection of defects requires a priori knowledge of reference or undamaged state of the structure, the proposed approach computes a virtual reference signal based on the dynamic distributed strain response of the structure in its current damaged state.

The formulations necessary to establish the virtual reference signal involved a dynamic curve fitting approach over specified sampling windows. The sampling window was swept over the strain signal in spatial domain. The window size was selected in order to balance the contrast between the effect of spatial resolution of the BOTDA and the signal intensities due to the existence of defects. The difference between the measured data and the virtual reference response was employed for the detection of defect locations.

An experimental program was designed to investigate the feasibility of the proposed approach in detecting the locations of very small defects. Laboratory experiments were designed in order to simulate the effect of ambient conditions in bridges, especially in terms of realistic displacements, i.e. deflections occurring in highway bridges. Distributed strain measurements were compared with the defect opening displacements measured by FBG displacement sensors. The experimental results indicated that the proposed method was capable of detecting defects in the order of 50 microns in width. The experiments performed in this study involved two defects. Future research should also involve experimentation with more closely spaced defects in order to examine the effect of multiple defects, and spatial resolution on the formulation of the virtual reference. Future studies should be expanded to bridges in order to evaluate the robustness of the proposed approach for monitoring damage under ambient conditions.

Chapter IV: Structural Defect Quantification using Dynamic Distributed Sensing

4.1. Introduction

Cracks and defects are the prevalent results of severe loads, aging, fatigue, corrosion, and environmental conditions on in-service structural systems such as bridges, building, and aircrafts components. Early detection of defects is mandatory to avoid major failures or costly repairs, replacements, and infrastructure shut downs. To accomplish this, it is necessary to perform detailed inspection as well as frequently evaluation of the structures for possible detection and quantification of all the defects during their early stages of formation.

During the Chapter 3 a reference free method has been proposed in order to locate the defects along the surface of structural components. However, it was pointed out that the proposed method is not capable to magnify the defects sizes. It is known that the optical fiber acts as a bridge between cracks when it is adhered or even embedded to the surface of structure. In this case, the fiber is subjected to localized strain discontinuity at the defect location. Localization of strain occurs in a very small segment of the fiber and it could not be quantitatively measured due to the spatial resolution limitations of the Brillouin based sensing. To address this issue, the mechanism of strain transfer from the structure surface to the sensing fiber core has been examined in a number of studies. These investigations implemented different analytical theories in order to specifically simulate the strain singularity within a segment of the optical fiber traversing a defect (Ansari and Libo 1998; Feng et al. 2013; Motamedi et al. 2012; Imai and Feng 2012). Despite the obvious advantages, the developed analytical methods have not

gained widespread usage in structural health monitoring. This is due to the fact that all the analytical methods have been established based on static conditions while the monitored structures are frequently subjected to vibration. In addition, the developed theories were established in complex mathematical functions in a way that their components have explicit mathematical relationships. The complexity prevents from developing formulas which quantify the defects sizes from the strain measurements. Furthermore, the previously established models require different material and geometric properties of optical fibers and adhesives. These requirements limit the practical application of the proposed formulas only to circumstances: (a) where the measurements are performed during the static condition of the structure; (b) during post processing, when the calculations are conducted in a later stage of measurements due to the complex nature of established formulas; and (c) the material and geometric properties of optical fibers and adhesives are known. In essence, all the existing models fall short in quantification of defect sizes using the distributed strain sensing.

The objective of the research described herein is to formulate a quantification method in order to estimate the sizes of defects using the dynamic distributed strain response of the structure. The theoretical formulation simulated the strain distribution within the components of an optical fiber crossing over a single crack opening. The strain transfer model that was developed previously at Smart Sensors and NDT lab of UIC was employed for the formation of distributed strain along the fiber length (Feng et al. 2013). It is designed in time domain to consider the dynamic vibration effects. Both linear and nonlinear mechanical characteristics of optical fiber components were assumed in the formulation as well as the dynamic effects have been also considered. The spatial

resolution effect was further numerically implemented within the formulation in order to simulate the measurement configurations. It was then possible to theoretically quantify the defect displacements from the measured dynamic distributed strain. An experimental program was designed for calibration as well as the validation of theoretical formulations. During the experimental program, a Brillouin Optical Time Domain Analyzer (BOTDA) device has been utilized in order to measure the dynamic distributed strain along the beam length. The calculated defect displacements were compared with the independently installed FBG crack displacement sensor measurements.

4.2. Proposed Methodology Formulation

A theoretical model, which accurately quantifies the deformation discontinuity due to the crack opening levels by the measured dynamic BOTDA strain response, is formulated herein. The proposed dynamic quantification formulation is established based on a shear lag model that considers the elastic as well as the elastoplastic behaviors of the fiber core-coating interfaces recently developed by Feng et al. (2013). The model has been successfully validated under static loading condition using a BOTDR distributed fiber optic sensor with 100 cm spatial resolution.

4.2.1. Dynamic Elastic Stage

Fig. 4.1 represents the schematic view of an optical fiber attached to the substrate structure including a fabricated crack opening. Due to symmetry, only half of the section of the optical fiber, as well as the substrate, has been shown. With a bonded sensing

fiber length of $2L$, a crack opening displacement (COD) of 2δ at $x = 0$, and considering elastic behavior within the fiber components with a strain ε_m in the structure, the displacement distribution $u_f^e(x)$, the strain distribution $\varepsilon_f^e(x)$, and shear stress distribution $\tau_f^e(x)$ in the optical fiber were derived in the optical fiber core by Feng et al. (2013) from a linear elastic analysis and given by the following expression:

$$u_f^e(x) = C_1 exp(\beta x) + C_2 exp(-\beta x) + \varepsilon_m x + \delta \qquad \text{(Eq. 1)}$$

$$\varepsilon_f^e(x) = \beta C_1 exp(\beta x) - \beta C_2 exp(-\beta x) + \varepsilon_m \qquad \text{(Eq. 2)}$$

$$\tau_f^e(x) = -\frac{E_f . r_f . \beta^2}{2}(C_1 exp(\beta x) + C_2 exp(-\beta x)) \qquad \text{(Eq. 3)}$$

Where β is the shear lag effect factor, which is related to the material and geometric properties of the optical fiber as well as the adhesive layer. x denotes the distance from the arbitrary section to the center. C_1 and C_2 are constants that are computed from the boundary conditions, $u_f(0) = 0$, and $\varepsilon_f(L) = \varepsilon_m$ for $x > 0$, and the final equations are given as Eq. (4) through Eq. (5). $u_f(0)$ corresponds to the displacement exactly at the location of defect $(x = 0)$ and $\varepsilon_f(L)$ represents the strain value at the location of L from the defect location $(x = L)$.

$$C_1 = -\frac{\delta_t}{exp(2\beta L) + 1} \qquad \text{(Eq. 4)}$$

$$C_2 = -\frac{\delta_t exp(2\beta L)}{exp(2\beta L) + 1} \qquad \text{(Eq. 5)}$$

In Eqs. (4-5), if $exp(2\beta L) \gg \delta$, then $C_1 \approx 0$ and $C_2 \approx -\delta$. By combining Eq. (2) and Eqs. (4-5) as well as expanding the Eq. (2) in time domain the strain $\varepsilon_f^e(x, t)$ value at the instance of t during the dynamic vibration can be simplified as:

$$\varepsilon_f^e(x, t) = \delta_t \beta exp(-\beta x) + \varepsilon_{m,t} \qquad \text{(Eq. 6)}$$

Each of the measurement conducted by any distributed sensing device is only a representative value in the spatial resolution distance and differs from the actual strain along the optical fiber. Therefore, it is not possible to use Eq. (2) in order to mathematically relate the distributed strain and COD and adjust the formulation for different measurement configurations. Initial known values of β and L are also required to form Eq. (2), which needs further detailed experiments as well as FEM analysis to be obtained. Additionally Eq. (2) was given the distributed strain for the static condition of structure and was not extended in time domain.

Rearranging Eq. (6) will result in the sole effects of crack induced strain, termed as ε_{cr}, and is given by the following expression:

$$\varepsilon_{cr}^e(x,t) = \varepsilon_f^e(x,t) - \varepsilon_{m,t} = \delta_t.\beta exp(-\beta x) \tag{Eq. 7}$$

The Brillouin scattering based methods averages the strains over their spatial resolution, and each of the distributed measurements signifies the average strain over a length of spatial resolution. The discrepancy between measured and theoretical strains are dramatically increased when there is a major singularity along the spatial resolution range. The singularity is mainly caused by crack opening displacement along the structure length. The theoretical strains shown in either Eq. (6) or Eq. (7) represents the real strain value at each point along the structure length, while the Brillouin sensors provide a weighted average of strains within the spatial resolution of the system along the sensor length. The averaged strain obtained by BOTDA at any section, i. e. along the sensor length can be written as (Yamauchi et al. 2007):

$$\bar{\varepsilon}_i = \frac{1}{\int_{-\frac{d}{2}}^{\frac{d}{2}} w(s)ds} \int_{-\frac{d}{2}}^{\frac{d}{2}} w(s)\varepsilon_i(s)ds \tag{Eq. 8}$$
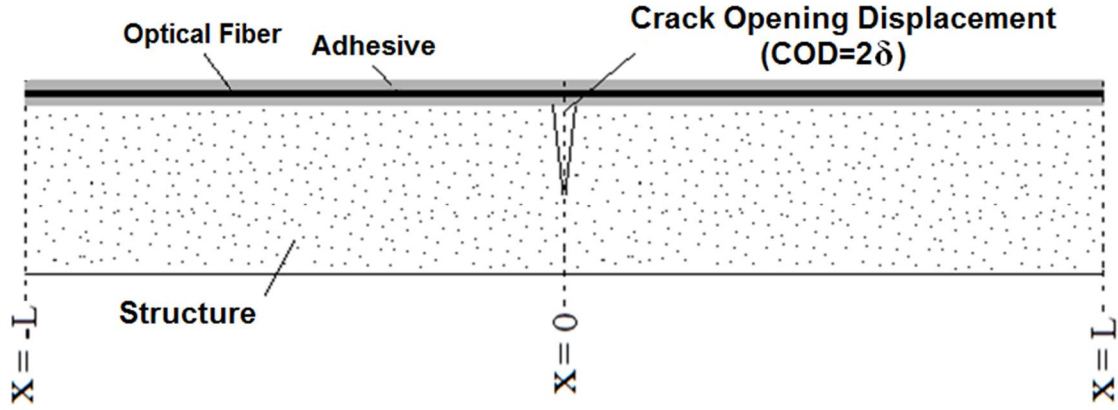
Figure 4.1 Optical fiber sensor crossing over a crack opening

Where, $\bar{\varepsilon}_i$ denotes the strain after implementing the spatial resolution effect, $\varepsilon_i(s)$ is the true strain at a distance of s, d is the spatial resolution or the length over which the BOTDA system averages the strain, and w is the weighting function which depends on the shape of the pump pulse and or pre-pump pulse. Considering a rectangular pump pulse, Eq. (9) can be simplified as a moving average over the averaging length (Kishida et al. 2005b) as follows:

$$\bar{\varepsilon}_i = \frac{1}{d}\sum_{-\frac{d}{2}}^{\frac{d}{2}}{}_d\,\varepsilon_i(s)\delta_s \qquad\qquad\qquad\qquad\text{(Eq. 9)}$$

Where, δ_s is the spatial resolution or the length over which the BOTDA system averages the strain, s is the spatial distance along the fiber, and $\varepsilon_i(s)$ is the actual strain at a distance, s, from the section under consideration. To consider the effect of spatial resolution Eq. (9) was employed for averaging of the computed strain by Eq. (7) over the spatial resolution of the BOTDA device, as shown below:

$$\overline{\varepsilon_{cr}^e}(x = 0, t) = \frac{\delta_t.\beta}{N}\left(1 + 2\sum_{i=1}^{\frac{SR}{2.SI}} exp(-\beta.SI.i)\right) \qquad\qquad\text{(Eq. 10)}$$

Where $\overline{\varepsilon_{cr}^e}(x = 0, t)$ corresponds to the theoretical elastic crack induced strain at the location of crack ($x = 0$) in which the spatial resolution effect has been implemented.

104

SR, SI, and N are respectively denoting spatial resolution, sampling interval and $\frac{SR}{SI} + 1$ values. Fig. 4.2 compares the difference between theoretical normal strain before and after implementation of spatial resolution effect. It is clear that the amplitudes of the singularities corresponded to the localized defects are dramatically decreased from the ones calculated from the theoretical formulation. This phenomenon will question the actual defect size estimation using the BOTDA measured strain response.
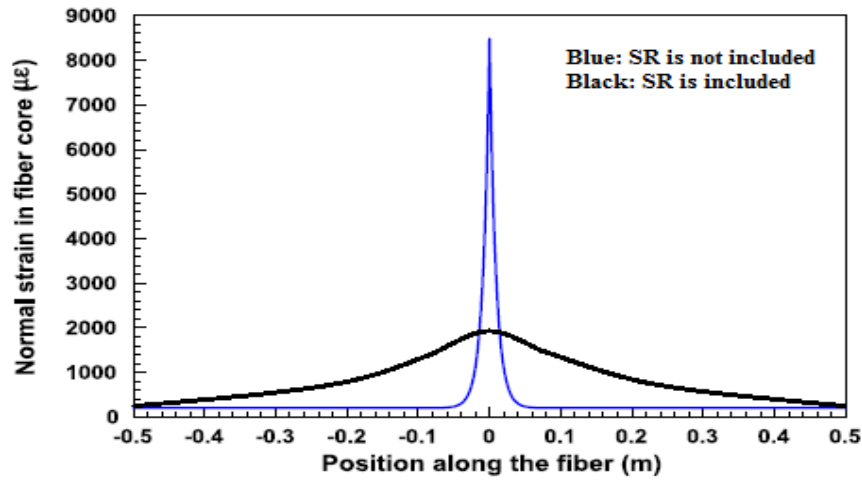
Figure 4.2 Theoretical normal strain in the fiber core based on elastic analysis before and after implementation of spatial resolution effect

Rearranging Eq. (10) will result in Eq. (11) quantifying the half COD (δ_t) at the instance of t during the dynamic vibration by the crack induced strain already being averaged:

$$\delta_t^e = K.\overline{\varepsilon_{cr}^e}(x = 0, t)$$ (Eq. 11)

Where, $K = \frac{N}{\beta(1+2\sum_{i=1}^{SR/(2.SI)} \exp(-\beta.SI.i))}$ is a time-independent (constant) parameter signifying the material and geometric properties of the optical fiber components as well as the measurement configurations. The procedure to calculate K is later discussed in the "4.2.4.Calibration" section. The calibration of K makes the quantification process needless from the knowledge of β and L terms.

4.2.2. Dynamic Elasto-Plastic Stage

Calculating the normal strain and shear stress for a range of given CODs (between 10-100 microns) shows that the COD at the crack location produced sharp peaks in both normal strain and the shear stress distributions. The singularity in strain profile at the location of crack exceeds the yield stress limits of the fiber core, which would lead to fracture of the fiber. However, actual experimental tests have shown that the fiber performs well without fracturing. For very small defects, it is possible to use the linear approach. However, at slightly larger crack opening displacements, the behavior becomes nonlinear defying the linear formulation. In the elasto-plastic phase, once the strain exceeds the fiber coating elastic limits plastic deformation is created and any extra increase in the strain yielding propagates through the optical fiber length. It should be noted that the fiber core remains elastic even when the coating has transferred to its plastic phase. Formation of cracks causes singularity in the strain profile resulting in localized plasticity in the optical fiber coating. The length of the plastic region, l_p, is a dependent of mechanical properties of optical fiber, i.e. core and coating, as well as crack opening displacement. The shear stress at the core-coating interface reaches its yield stress limitation within the plastic region. It is assumed that the polymeric coating behaves as an ideal elasto-plastic material. Fig. 4.3 and Fig. 4.4 respectively represent the normal strain in the fiber core and shear stress at the core-coating interface. Therefore, the elasto-plastic model proposed by Feng et al. (2013) has been expanded herein to be implemented for dynamic formulation. The displacement distribution $u_f^p(x)$, the strain distribution $\varepsilon_f^p(x)$, and shear stress distribution $\tau_f^p(x)$ in the optical fiber were derived by Feng et al. (2013) and are given by the following expressions:

106

$$u_f^p(x) = \begin{cases} D_1 exp(\beta x) + D_2 exp(-\beta x) + (\varepsilon_m x + \delta) & x > l_p \\ -\dfrac{\tau_{cr}}{E_f r_f} x^2 + D_3 x + D_4 & x < l_p \end{cases} \tag{Eq. 12}$$

$$\varepsilon_f^p(x) = \begin{cases} \beta D_1 exp(\beta x) - \beta D_2 exp(-\beta x) + \varepsilon_m & x > l_p \\ -\dfrac{2\tau_{cr}}{E_f r_f} x + D_3 & x < l_p \end{cases} \tag{Eq. 13}$$

$$\tau_f^p(x) = \begin{cases} \tau_{cr} & x < l_p \\ -\dfrac{\beta^2}{2E_f r_f}\{D_1 exp(\beta x) + D_2 exp(-\beta x)\} & x > l_p \end{cases} \tag{Eq. 14}$$

$$D_1 = -\frac{2\tau_{cr} exp(\beta l_p)}{\beta^2 E_f r_f \{exp(2\beta l_p) + exp(2\beta L)\}} \tag{Eq. 15}$$

$$D_2 = -\frac{2\tau_{cr} exp(\beta l_p)}{\beta^2 E_f r_f \{1 + exp[2\beta(l_p - L)]\}} \tag{Eq. 16}$$

$$D_3 = \varepsilon_m + \frac{2\tau_{cr} l_p}{E_f r_f} + \frac{2\tau_{cr}}{\beta E_f r_f} \cdot \left(\frac{exp(2\beta L) - exp(2\beta l_p)}{exp(2\beta L) + exp(2\beta l_p)}\right) \tag{Eq. 17}$$

$$D_4 = \delta - \frac{2\tau_{cr}}{\beta^2 E_f r_f} - \frac{\tau_{cr} l_p^2}{E_f r_f} - \frac{2\tau_{cr} l_p}{\beta E_f r_f} \cdot \left(\frac{exp(2\beta L) - exp(2\beta l_p)}{exp(2\beta L) + exp(2\beta l_p)}\right) \tag{Eq. 18}$$
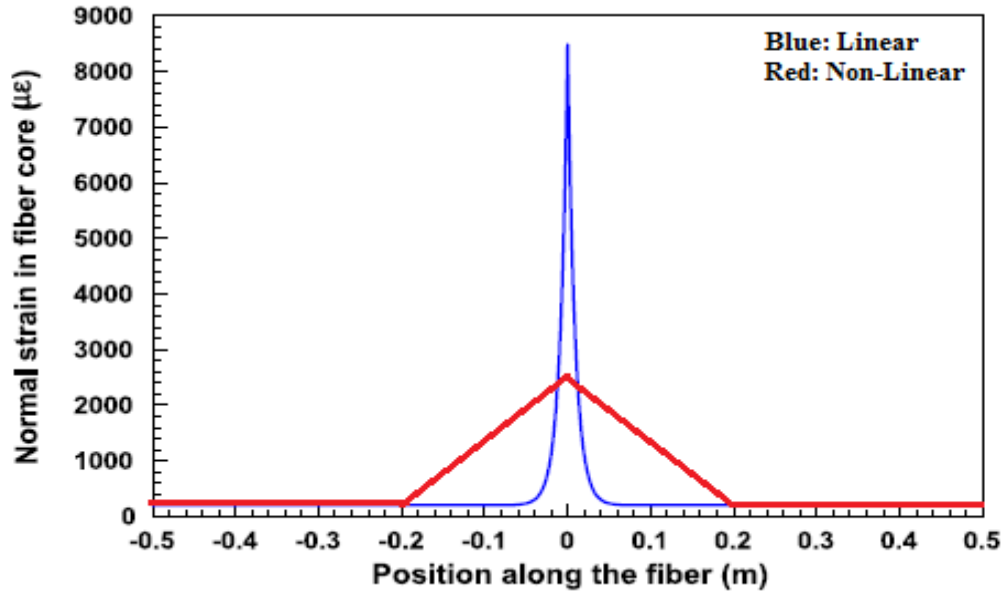
Figure 4.3 Normal strain in the fiber core based on elastic and elasto-plastic analysis
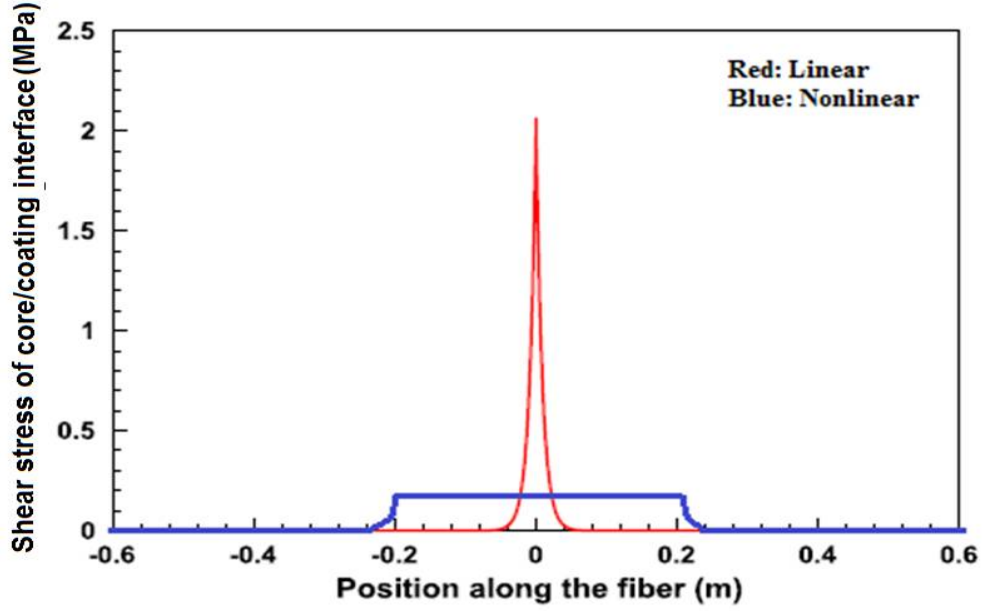
Figure 4.4 Shear stress at the coating-core interface based on elastic and elasto-plastic analysis

As mentioned earlier, Fig. 4.3 represents the difference between strains calculated by considering elastic as well as the elasto-plastic conditions. It is obvious that considering elasto-plastic behavior dissipates the strain along the longer length of beam reliving localized strain concentration in the fiber core. Considering the boundary condition, $u_f^p(0) = 0$ yields the half-COD relationship as:

$$\delta = \frac{2\tau_{cr}}{\beta^2 E_f r_f} + \frac{\tau_{cr} l_p^2}{E_f r_f} + \frac{2\tau_{cr} l_p}{\beta E_f r_f} \cdot \left(\frac{exp(2\beta L) - exp(2\beta l_p)}{exp(2\beta L) + exp(2\beta l_p)} \right) \qquad \text{(Eq. 19)}$$

To draw the distributed strain profile using Eq. (13), it is required to know the values of $\tau_{cr}, E_f, r_f, \beta, L$, and l_p. The $\tau_{cr}, E_f, r_f, \beta, L$ terms correspond to the material and geometric properties of optical fiber and must be obtained via experimental tests and or FEM analysis. Alternatively, based on Eq. (19), the plastic zone l_p could be only estimated by a known value of COD which requires to be independently measured. This issue disables the Eq. (14) through (19) to be employed for defect size quantification by using distributed sensing. Furthermore, there is no exact definition in Eqs. (14-19) where the

108

elastic behavior is being transferred to the elasto-plastic phase. The previously discussed issues such as complex formulation and lack of consideration of spatial resolution effects additionally drawback the Eqs. (14-19) to be applied for quantification purposes.

It should be noted that the COD depends on the plastic region length, l_p, as well as the mechanical properties of the fiber core and polymeric coating. Eq. (19) reveals that the COD has a direct relationship with the plastic region length, l_p. Fig. 4.5 represent the beam vertical deflection diagram under dynamic free loading as well as the shear strain-stress diagram of the fiber coating under periodic dynamic loading. During the dynamic vibration in which the deflection profile of the beam has either a descending or ascending order, the l_p is not constant and does not keep its initial value which corresponds to the largest deflection (point A in both Fig. 4.5a and Fig. 4.5b). In other words, some portions of the fiber coating that have already reached their plastic limit do not always remain in their plastic conditions in later vibrations. Unloading the beam causes the plastic region of the fiber coating to return back to their initial elastic condition (point E in both Fig. 4.5a and Fig. 4.5b) while some residual shear strains remain along the fiber coating. The residual shear strain in the coating causes an internal normal strain within the fiber core which can be easily compensated by shifting to the zero value. By reloading the beam, the fiber acts as a new one and all of its components start their behaviors from the elastic condition. According to Fig. 4.5, the corresponding l_p values can be different for different levels of COD which can be independently calculated by Eq. (19).
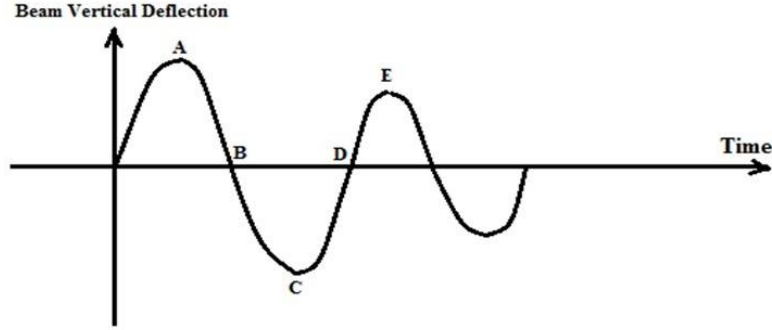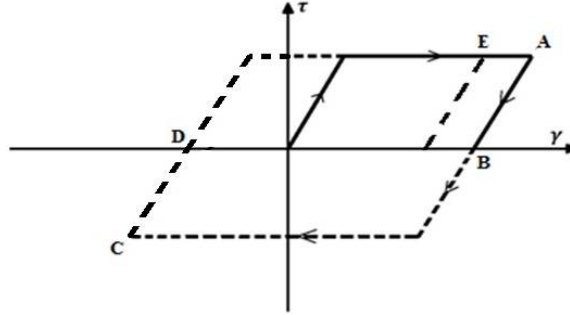
Figure 4.5 a) The beam vertical deflection diagram under dynamic free loading, b) Schematic shear strain-stress of the fiber coating under periodic dynamic loading

Referring back to Eq. (19), since $L \gg l_p$ and $exp(2\beta L) \gg exp(2\beta l_p)$, then $\frac{exp(2\beta L) - exp(2\beta l_p)}{exp(2\beta L) + exp(2\beta l_p)} \approx 1$. By considering the dynamic vibration in the time domain and rearranging Eq. (19) the half COD in the fiber core can be simplified as:

$$\delta_t = K'.\left(\frac{1}{\beta} + \frac{l_{p,t}^2}{2\beta} + l_{p,t}\right) \tag{Eq. 20}$$

Where, $K' = \frac{2\tau_{cr}}{\beta E_f r_f}$ is a time-independent/constant parameter signifying the material and geometric properties of the optical fiber components. $l_{p,t}$ denotes the plastic region length corresponding to the half COD at the instance of t during the dynamic vibration.

110

Similarly to K, the procedure to calculate K' is later discussed in the "4.2.4.Calibration" section.

As it is obvious from Eqs. (12)-(19), the relationship between COD and the normal strain within the fiber core follows a complex explicit mathematical format. In order to simplify the above mentioned formulas and eliminate the less effective factors from the equations, a sensitivity analysis was implemented. Sensitivity analysis provides a powerful tool in order to evaluate the contribution of each input variable in the proposed model or output (Gandomi et al. 2013). The sensitivity analysis used here was primarily developed by Gandomi et al. (2013) and has been numerously applied in different investigations. The details regarding the applied sensitivity analysis is later discussed in "4.2.3.Sensitivity Analysis" section. For a given instance of dynamic vibration, performing sensitivity analysis on the $(\frac{1}{\beta} + \frac{l_{p,t}^2}{2\beta} + l_{p,t})$ term respectively shows 97% and 3% dependencies to the $l_{p,t}$ and β variables. Therefore, with a high degree of accuracy the $(\frac{1}{\beta} + \frac{l_{p,t}^2}{2\beta} + l_{p,t})$ term can be substituted by a function of $l_{p,t}$. Fig. 4.6 demonstrates the dependency of the aforementioned term versus the $l_{p,t}$ and β variations. The best polynomial function was fitted in order to relate the $\left(\frac{1}{\beta} + \frac{l_{p,t}^2}{2\beta} + l_{p,t}\right)$ term to the $l_{p,t}$ term and substituting in Eq. (20) results in:

$$\delta_t = K'.\left(0.5l_{p,t}^2 + 0.0164l_{p,t} + 0.0003\right) \qquad (Eq.\,21)$$
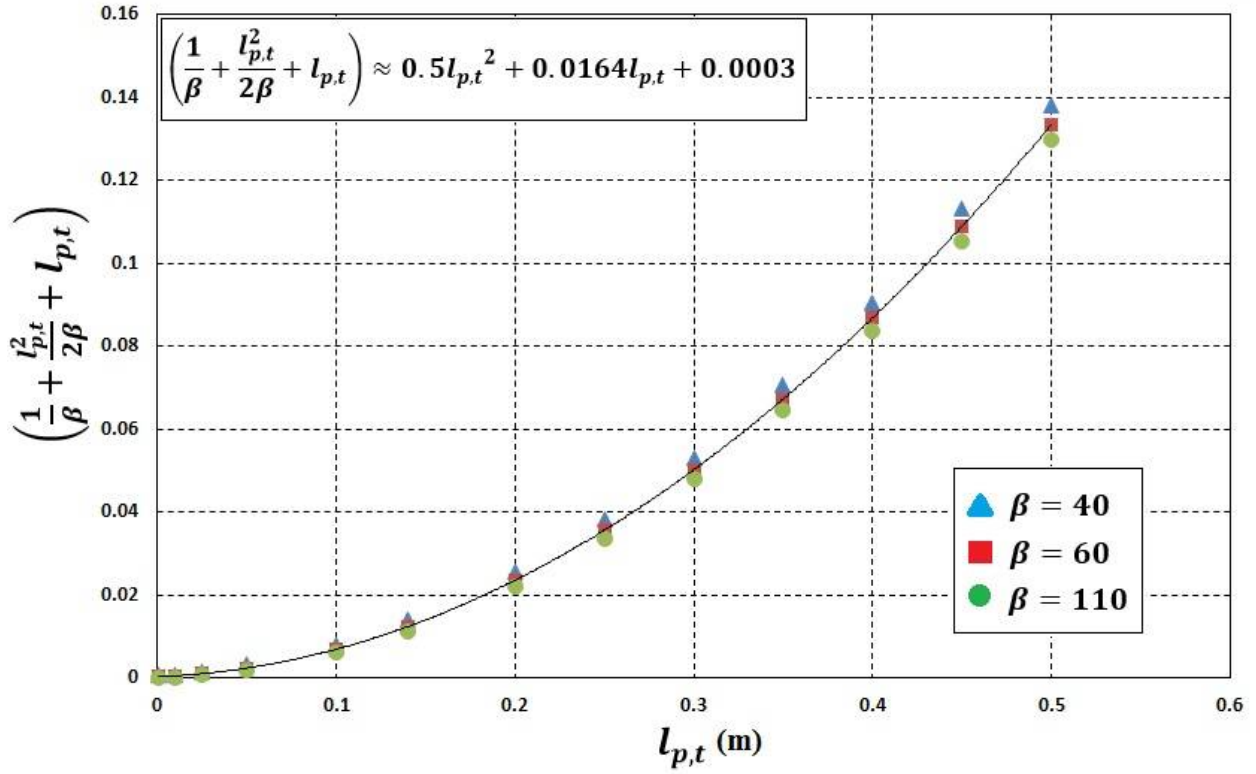
Figure 4.6 The diagram of $\left(\frac{1}{\beta} + \frac{l_{p,t}^2}{2\beta} + l_{p,t}\right)$ term versus the $l_{p,t}$ variations

Furthermore, by substituting Eq. (20) into Eq. (13) and considering the fact that the crack induced strain for the location of fiber far from the plastic region ($x > l_{p,t}$) is negligible, will result in:

$$\varepsilon_{cr}^p(x,t) = \varepsilon_f^p(x,t) - \varepsilon_{m,t} = \begin{cases} \delta_t \left(\dfrac{\beta l_{p,t} - \beta x + 1}{\frac{1}{\beta} + \frac{l_{p,t}^2}{2\beta} + l_{p,t}}\right) & x < l_{p,t} \\ \approx 0 & x > l_{p,t} \end{cases} \qquad \text{(Eq. 22)}$$

Where $\varepsilon_f^p(x,t)$ and $\varepsilon_{cr}^p(x,t)$ respectively denote the strain in the optical fiber core and the crack induced strain while the fiber coating has passed its elastic limits. Similar to the elastic phase, to consider the effect of spatial resolution on the strains computed from elasto-plastic theoretical analysis, Eq. (22) was substituted in the averaging relationships explained by Eq. (9), resulting in:

112

$$\overline{\varepsilon_{cr}^{p}}(x = 0, t) = \left\{ \begin{array}{ll} \delta_t \left(\dfrac{(2n+1)(\beta l_{p,t}+1)-\beta.SI.n(n+1)}{N(\frac{1}{\beta}+\frac{l_{p,t}^2}{2\beta}+l_{p,t})} \right) & \dfrac{SR}{2} > l_{p,t} \\[4mm] \delta_t \left(\dfrac{(2n\prime+1)(\beta l_{p,t}+1)-\beta.SI.n\prime(n\prime+1)}{(2n\prime+1)(\frac{1}{\beta}+\frac{l_{p,t}^2}{2\beta}+l_{p,t})} \right) & \dfrac{SR}{2} < l_{p,t} \end{array} \right.$$

$$(Eq. 23)$$

Where $\overline{\varepsilon_{cr}^{p}}(x = 0, t)$ corresponds to the theoretical elasto-plastic crack induced strain at the location of crack ($x = 0$) in which the spatial resolution effects has been implemented. N, n, and $n\prime$ are respectively denoting the closest integer value of $SR/SI + 1$, $l_{p,t}/SI$, and $SR/(2.SI)$ values. Fig. 4.7 compares the difference between theoretical normal strain before and after implementation of spatial resolution effect. As pinpointed previously this is an expected problem owing to the strain averaging process over spatial resolution distance. To evaluate the dependency of the term inside the parenthesis to the $l_{p,t}$ and β terms in Eq. (23), a typical sensitivity analysis was also performed. The sensitivity analysis was implemented by considering the $l_{p,t}$ and β terms as variables while the SR and SI components were assumed to be constant. The analysis showed respectively 98% and 2% dependencies of the aforementioned term to the $l_{p,t}$ and β variables' changes. Therefore, with a high degree of accuracy the term can be substituted by a function of $l_{p,t}$. Fig. 4.8 demonstrates the dependency of the aforementioned term versus the $l_{p,t}$ and β variations. For a given $SR = 20\ cm$ and $SI = 5\ cm$ measurement configurations conducted in current investigation, the best fitted polynomial function was achieved. The fitting product has been substituted in Eq. (23), resulting in:

$$\delta_t = \overline{\varepsilon_{cr}^{p}}(x = 0, t).\left(0.56l_{p,t}^2 + 0.092l_{p,t} + 0.1176\right) \qquad (Eq. 24)$$
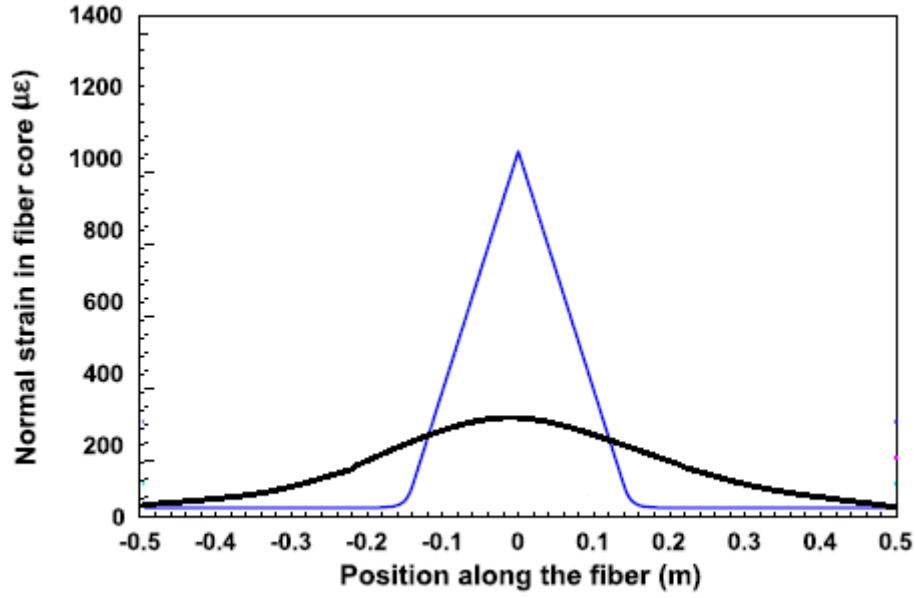
Figure 4.7 Theoretical normal strain in the fiber core based on elasto-plastic analysis before and after implementation of spatial resolution effect
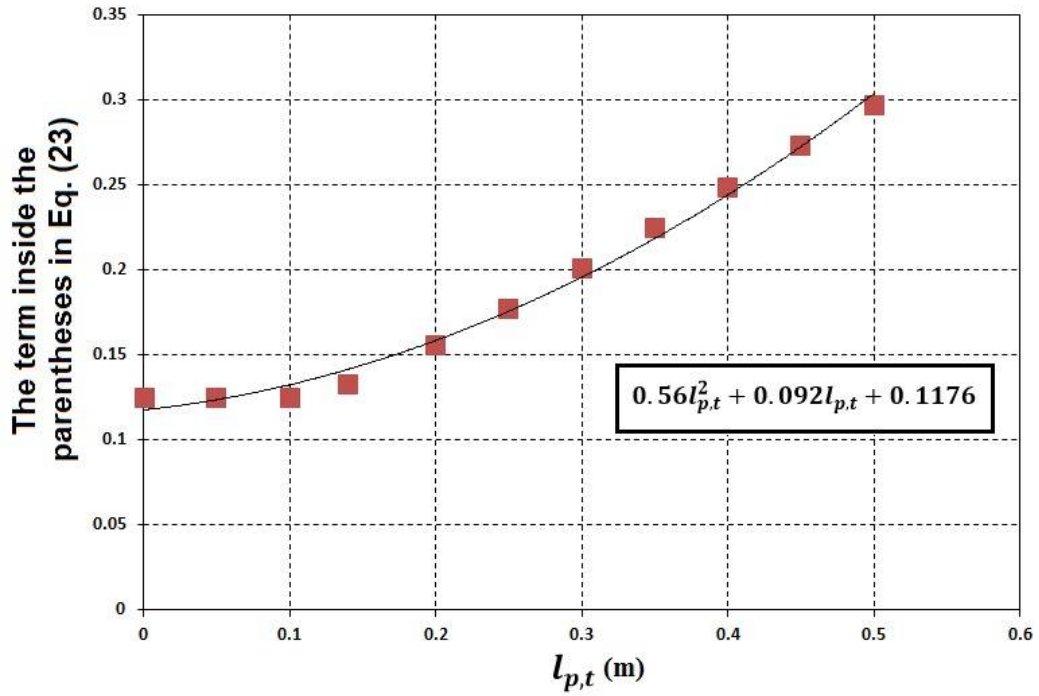
Figure 4.8 The diagram of term inside the parentheses in Eq. (23) versus the $l_{p,t}$ variations

Substituting Eq. (24) into Eq. (21) yields

$$\overline{\varepsilon_{cr}^{p}}(x = 0, t) = K' . \frac{0.5l_{p,t}^{2} + 0.0164l_{p,t} + 0.0003}{0.56l_{p,t}^{2} + 0.092l_{p,t} + 0.1176}$$ (Eq. 25)

As shown in Fig. 4.9, the fraction component in Eq. (25) was calculated for different $l_{p,t}$ values demonstrating a proper simple linear substitution equal to $0.8607l_{p,t}$. Therefore, Eq. (25) can be re-written as:

$$l_{p,t} = 1.1618 \frac{\overline{\varepsilon_{cr}^{p}}(x=0,t)}{K'}$$ (Eq. 26)
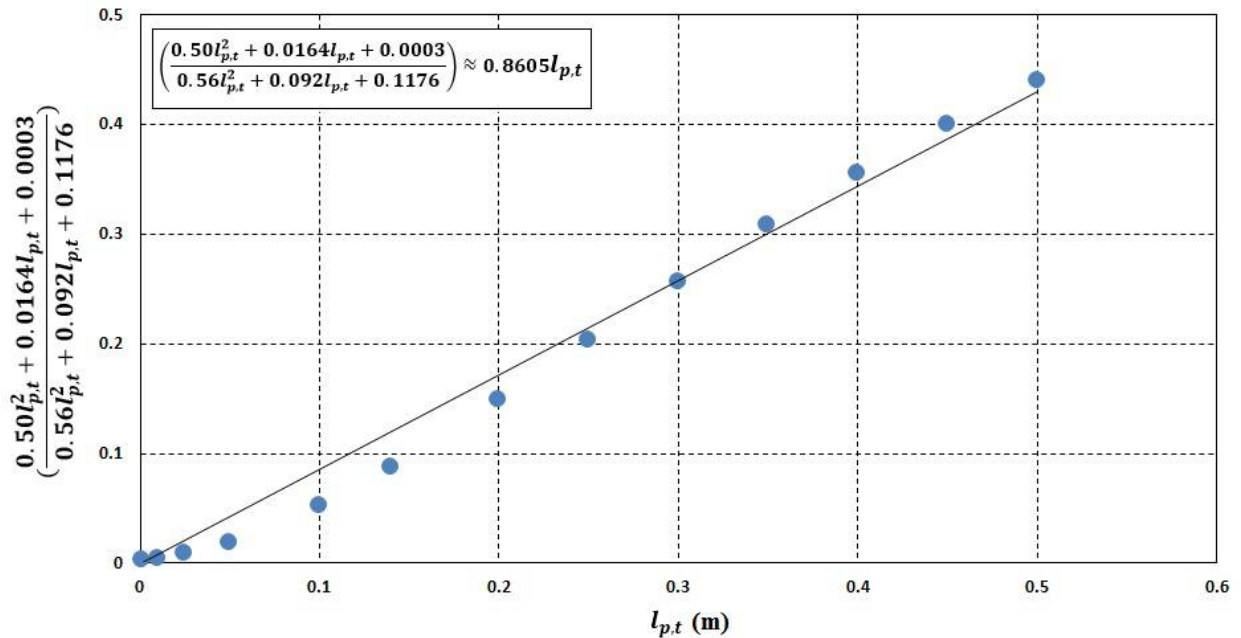
Figure 4.9 The diagram of the fraction component in Eq. (25) versus the l_p variations

Back substitution of Eq. (26) into Eq. (21) results in quantifying the half COD (δ) by the crack induced strain in which the effects of spatial resolution was already implemented:

$$\delta_{t}^{p} = K' . \left(0.675 \left(\frac{\overline{\varepsilon_{cr}^{p}}(x = 0, t)}{K'} \right)^{2} + 0.0191 \left(\frac{\overline{\varepsilon_{cr}^{p}}(x = 0, t)}{K'} \right) + 0.0003 \right)$$ (Eq. 27)

4.2.3. Sensitivity Analysis

Sensitivity analysis was previously developed in order to evaluate the contribution of each input variable to the final output of a given model. The model could be an empirical/numerical mathematical function or a simulation box. Sensitivity analysis is performed to quantitatively measure the dependency of a given model to its constitutive components. The approach of sensitivity analysis proposed by Gandomi et al. (2013) is simple and therefore, was applied in current study. For a given function or model, the sensitivity percentage of the output to each input parameter is determined using the following formulas:

$$N_i = f_{max}(x_i) - f_{min}(x_i) \qquad \text{(Eq. 28)}$$

$$S_i = \frac{N_i}{\sum_{j=1}^{n} N_j} \times 100 \qquad \text{(Eq. 29)}$$

where $f_{min}(x_i)$ and $f_{max}(x_i)$ respectively denote the minimum and maximum of the predicted output over the ith input domain, where other variables are equal to their mean values. S_i represents the contribution of each input variable (i) in terms of final output.

4.2.4. Calibration Procedure

Eq. (11) and Eq. (27) respectively quantify the crack opening displacement based on the measured BOTDA strain response for both elastic and elasto-plastic phases during dynamic vibrations. As the K and K' parameters are determined with higher accuracy, the level of predicted results increase. Using the materials and geometrical properties of the optical fiber or even implementing a detailed FEM analysis can calculate the aforementioned parameters, a more realistic approach is to compute them during the

calibration process. This assures that these factors portray changes in the materials properties and geometrical characteristics as well as composite action of the fiber core-coating-adhesive interfaces. This necessity is more highlighted when the dynamic effects have additionally influenced the experiment. During the calibration process, the K (or K′) value is calibrated by defining an error function (E), as formulated by Eq. (30), representing the differences between measured and theoretical crack openings. The function E is minimized in terms of K (or K′) to position the theoretical crack opening as close as possible to the measured openings.

$$E = \begin{cases} \sum_{i=1}^{num} \left[\delta_i^{Measured} - \delta_i^{e} \right]^2 & to\ find\ the\ best\ K\ for\ Elastic\ phase \\ \sum_{i=1}^{num} \left[\delta_i^{Measured} - \delta_i^{p} \right]^2 & to\ find\ the\ best\ K'\ for\ ElastoPlastic\ phase \end{cases} \quad (Eq.\,30)$$

Where E is the objective function, $\delta_i^{Measured}$ is the ith measured crack opening independently recorded by FBG crack sensor, δ_i^{e} and δ_i^{p} are respectively the theoretical elastic and elasto-plastic crack openings calculated by Eq. (11) and Eq. (27), and num is the total number of available data points measured during the dynamic vibrations. To calculate the δ_i^{e} and δ_i^{p} components, $\overline{\varepsilon_{cr}^{p}}(x = 0, t)$ and $\overline{\varepsilon_{cr}^{e}}(x = 0, t)$ are required. These terms are achieved from the BOTDA measurements later discussed in the "4.3.Experimental Investigation" section. Using Eq. (20) and replacing l_p equals to zero locates the point where the elastic behavior is being transferred to the elasto-plastic phase. For half COD (δ) less than the transition point, the elastic form of Eq. (30) is applied. Conversely, the elasto-plastic form of Eq. (30) is used for the half COD (δ) greater than the transition point. Minimizing Eq. (30) is a non-linear optimization problem and could be solved by different mathematic based, evolutionary based, or pattern

based techniques. For the present study, a MATLAB code has been implemented based on the pattern search technique. During the calibration process, the BOTDA measured crack induced strain response and the FBG crack sensor measured displacement are employed in order to obtain K (or K'). Once K (or K') is computed during the calibration process, the crack opening displacement can be quantified from the BOTDA measured strain response using either Eq. (11) or Eq. (27).

4.3. Experimental Investigations

4.3.1. Experimental testing procedure

The proposed quantification methodology is established based on the considering the dynamic motion of the beam shown in Fig. 4.10a. The beam could be represented as any structural component such as a bridge girder vibrated due to the traffic passage, or stiffening element of a fuselage during flight, etc. It is further considered that the beam has incurred damage in the form of two small defects. In the experiments the two defects were designed by splicing three wide flange sections to form a 15 meter long beam. The bolts in the spliced sections could be manipulated to show various magnitudes of displacements due to opening of defects under dynamic loads at either one or both joints. They could be also tightened to represent an intact beam without defects. The beam dimensions and the locations of the two defects and support locations are schematically provided in Figs. 14.10a, 14.10b and 14.10c. Fig. 14.10d shows the actual beam in the loading frame. Beam oscillation is induced by releasing the mid span of the beam after displacing it by 9 mm. As shown in Figs. 14.10c and 14.10d, the vertical movement of the beam at the two supports is prevented by the

118

frame assembly. The optical fiber was pre-tensioned to a prescribed level and adhered along the entire 15-meter length of the beam. This procedure assures that the fiber remains in tension during load cycles. As shown in Fig. 14.10a and 14.10d, the sensor was placed on the top surface for ease of operations during the laboratory experiments. It was then connected to an AT-BOTDA device as shown in Fig. 4.11. A single mode Corning SMF-28 commercial optical fiber with a polymeric coating around was adhered using a glue adhesive to the surface of the beam over the 15 m span. The dynamic distributed measurements were conducted using a commercial BOTDA measuring unit manufactured by Neubrex-model # NBx-6055 (Fig. 4.11).
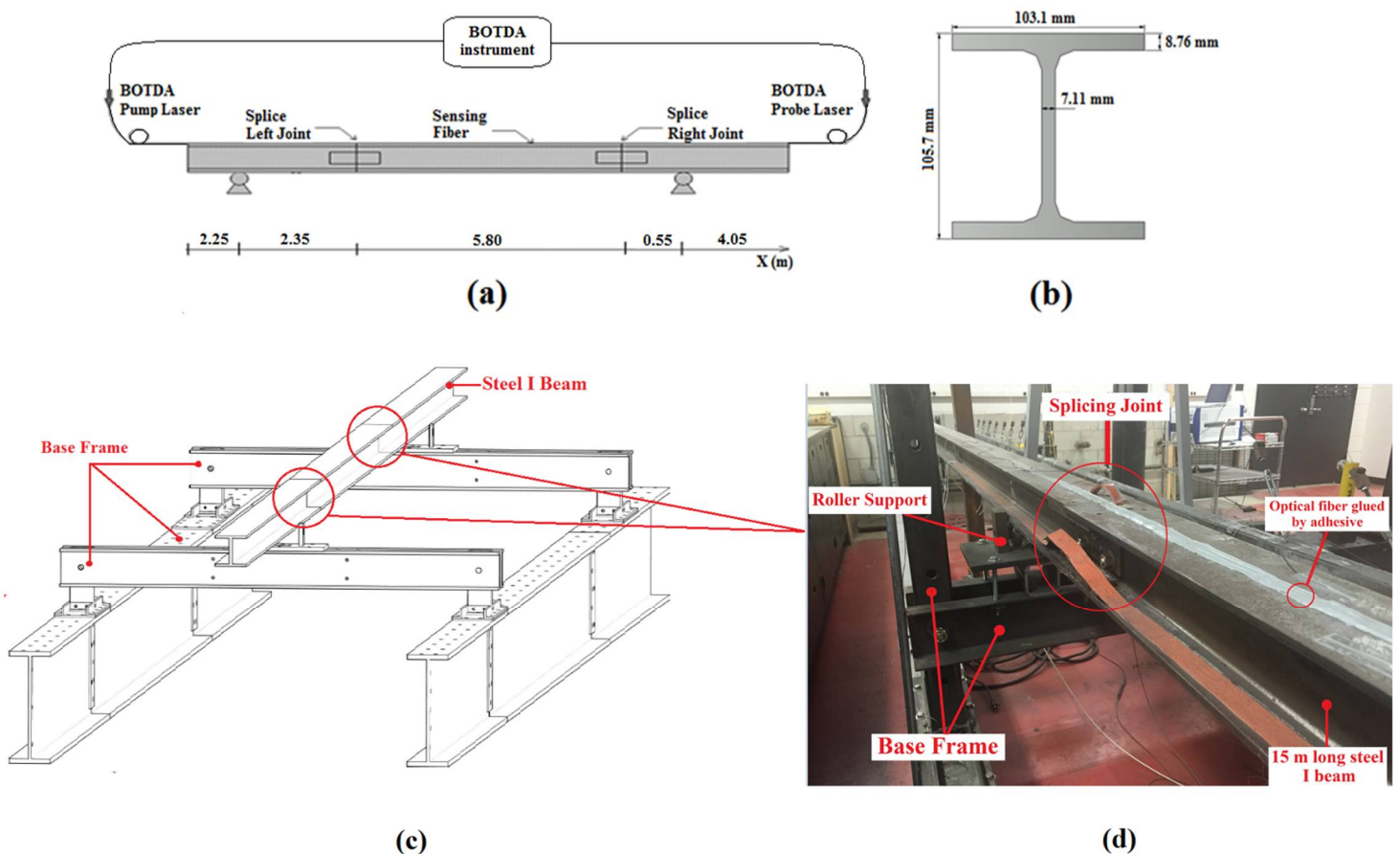
Figure 4.10 a) Beam layout, b) beam cross section details, c) schematic view, d) actual beam in the loading frame
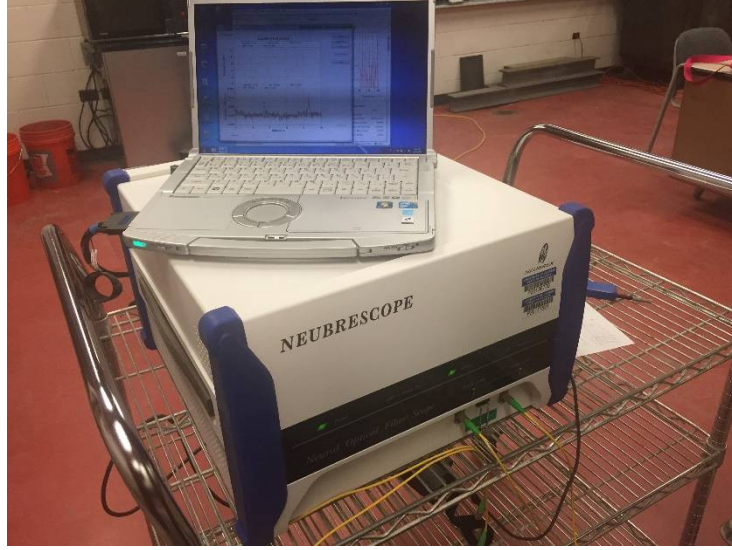
Figure 4.11 BOTDA interrogation device manufactured by Neubrex Ltd

The experimental program involved oscillating the beam and recording the distributed dynamic strain data along the length of the beam. The objective was to extract the crack induced strain response in order to quantify the COD. The BOTDA measured data pertained to spatial distribution of strain in time domain, providing a three dimensional (3-D) representation of the dynamic strain distribution of the structural system during the sampling period. Fig. 4.12a pertains to the response of the damaged beam as acquired by the AT-BOTDA. In the 3-D response spectrum of Fig. 4.12a, the vertical axis is the strain amplitude, the horizontal axis corresponds to the distance along the beam length, and the transverse axis represents time. In addition to the induced strain due to opening of the defects in the optical fiber, ε_{Cr}, the strain response of the beam with defects, ε_D, is influenced by the dynamic load, system noise, temperature, and the pre-tensioning strain in the fiber. The strain response of the beam with a defect is generally described by the following relationship:

$$\varepsilon_D = \varepsilon_m + \varepsilon_{Tf} + \varepsilon_{Ts} + \varepsilon_{PT} + \varepsilon_N + \varepsilon_C \qquad (Eq.\,31)$$

(a) Damaged structure
ε_f (strain in fiber)

(b) Undamaged structure
ε_m (loading strain on substrate)

(c) Crack induced strain
ε^* (crack induced strain)
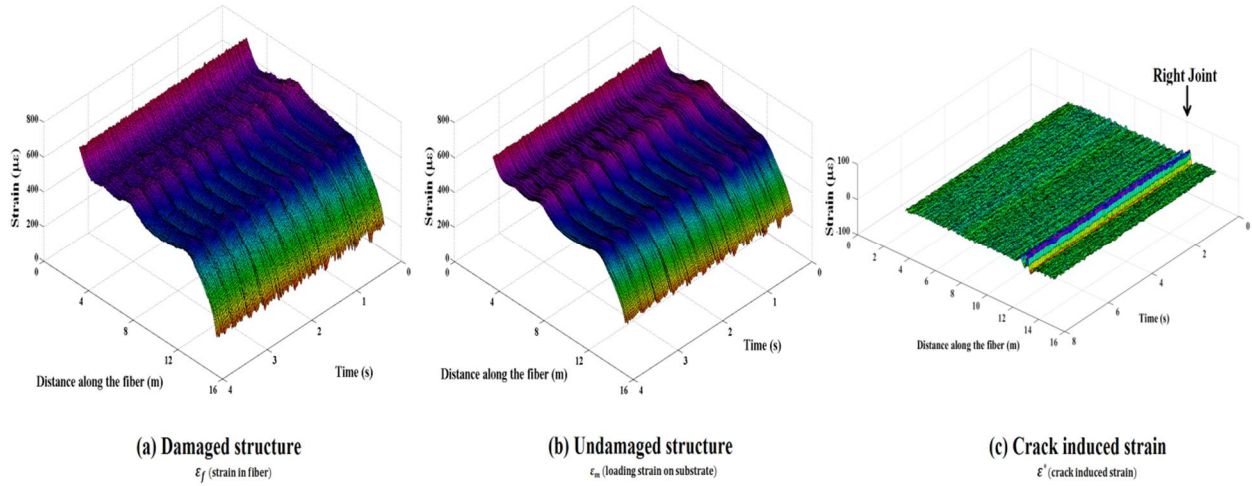
Figure 4.12 a) Damaged structure, b) Undamaged structure, c) Sole effect of crack induced strain

Where, $\varepsilon_m, \varepsilon_{Tf}, \varepsilon_{Ts}, \varepsilon_{PT},$ and ε_N pertain to the flexural strain in the beam due to dynamic load, temperature induced strain in fiber, temperature induced strain in structure, residual strain in the fiber due to pre-tensioning, and noise. The other strain terms in Eq. (31), intrinsically mask the strain generated from the opening of the defects. Therefore, it will be necessary to eliminate as much the effects of the other strain components from the signal in order to differentiate the influence of the defects. To extract the sole effects of crack induced response, the reference data corresponding to the response of beam without any defect is required. To do so, the strain response of the undamaged beam under the same free vibration loading condition was used as a reference data. The reference data strain response (ε_D) primarily includes the effects of $\varepsilon_m, \varepsilon_{Tf}, \varepsilon_{Ts}, \varepsilon_{PT},$ and ε_N. Therefore, the subtraction of strain response for the damaged condition of the beam from the damaged condition of the beam under equal dynamic loading results in the sole effect of crack induced strain (ε_{cr}).

Fig. 4.12a represents the beam in the damaged state, and Fig. 4.12b pertains to the same beam in undamaged state without a defect. Once these two signals are

subtracted from each other, it is possible to discern the influence of the defects from the strain response, which is shown in Fig. 4.12c. Depending on the level of strain acting along the fiber, the response of Fig. 4.12c corresponds to the either $\overline{\varepsilon_{cr}^{p}}(x,t)$ or $\overline{\varepsilon_{cr}^{e}}(x,t)$ respectively denoted by Eq. (11) and Eq. (27).

Different crack levels (CL) were introduced in the beam by defining different crack openings in order to simulate the defect initiation and growth, and to determine the sensitivity of proposed quantification approach. The level of damage and its severity were possible to be manipulated by tightening or loosening the bolts at the gusset plates. Fig. 4.13 depicts a typical gusset plate connection at the spliced joint. An arch type FBG-based displacement sensor was independently installed at the spliced joint location to measure the defect opening displacements ($\delta^{Measured}$ in Eq. (30)) during the dynamic vibration. Details regarding the FBG based displacement sensor can be found elsewhere (Bassam et al. 2011; Iranmanesh and Ansari 2014). Table 4.1 corresponds to the experimental program for the range of damage levels simulated by crack opening displacements considered in the present study. The experiments were conducted in a sequential manner wherein the crack levels progressively increased to reach the maximum opening.
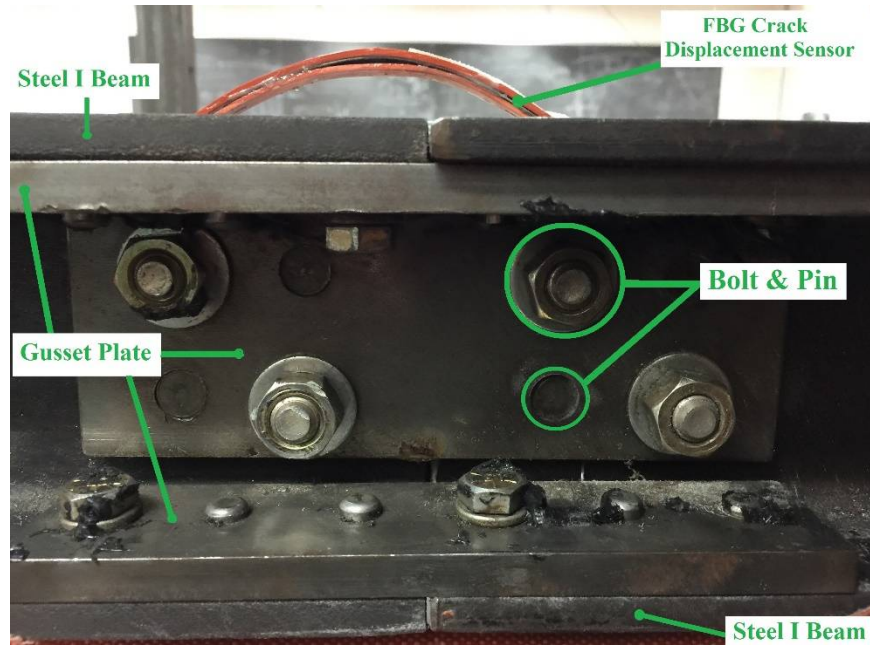
Figure 4.13 Spliced joint connection in details

Table 4.1 Summary of different experimented crack opening levels

Level of Crack	Left Joint Max Opening (µmm)	Right Joint Max Opening (µmm)
CL#0	30	30
CL#1	30	60
CL#2	35	120
CL#3	35	125
CL#4	50	120
CL#5	220	130
CL#6	300	160
CL#7	320	220
CL#8	350	240
CL#9	550	280
CL#10	330	260
CL#11	300	245
CL#12	160	135
CL#13	90	75
CL#14	50	45

The undamaged state (intact) of the beam pertained to the condition where all the bolts

at the spliced joints were fully tightened. For the intact condition (CL0), even though all

the bolts were tightened, the defects opened by as much as 30 microns during

oscillations as demonstrated in Table 4.1. As mentioned earlier, in order to acquire the sole effect of crack induced strain for damaged levels of the beam (DL1-14), the response of the undamaged condition (CL0) is subtracted from all of the damaged conditions. The remaining respond corresponds to the either $\overline{\varepsilon_{cr}^p}(x,t)$ or $\overline{\varepsilon_{cr}^e}(x,t)$. The Amplitude Transfer (AT) mode of the Neubrex device has been utilized in order to conduct the dynamic distributed strain measurements. The sampling interval (SI) and the spatial resolution (SR) were set as 5 cm and 20 cm, respectively. The dynamic measurement was conducted by 26 Hz speed (26 measurements/second).

4.3.2. Experimental results and discussion

The Eq. (30) was employed for calibration of the proposed quantification formulation. First, the BOTDA measured crack induced strain was achieved through the subtraction of the responses of damaged and intact conditions of the beam. Then, the corresponding strains at the location of both cracks (or splice joints) were extracted and considered either as the $\overline{\varepsilon_{cr}^p}(x=0,t)$ or $\overline{\varepsilon_{cr}^e}(x=0,t)$. These terms were used to calculate the theoretical half COD (δ^e and δ^p terms in Eq. (30)). Besides, the FBG displacement sensors simultaneously measured the crack opening at the location of both cracks. The FBG displacement sensor measurements pertained to the δ^{Measured} term in Eq. (30). Finally, minimizing Eq. (30) resulted in calibrating the K and K' parameters. Following calibration calculations, with the known K and K' parameters, the Eq. (11) and Eq. (27) were utilized again, this time for quantification of COD using the BOTDA measured strain response. Further verification tests were performed in order to evaluate the efficacy of the proposed quantification formula.

As discussed earlier, the level of damage in terms of induced crack was simulated by increasing the width of the cracks at the spliced joints. The experiments were conducted in a sequential manner wherein damage levels CL1 through CL3 pertain to the progressive increase in crack size at the right joint. CL4 through CL6 correspond to progressive increase in the crack size at the left joint. During the experiments at the damage levels corresponding to CL4 through CL6, the amount of tension in the right side joint bolts remained at the CL3 level. Following these experiments, the right and left side joint bolts were simultaneously increased at three stages corresponding to the crack levels CL7 through CL9. Later on, the right and left side joint bolts were simultaneously tightened at five stages along the crack levels CL10 through CL14. Each damage level was experimented four times in order to increase the repeatability of the results. For each damage level, one run was applied for calibration and determination of K and K', and the rest of three runs were specified for verification. During the calibration process, the selected runs of different damage levels were assembled together and all the data points were fed into the Eq. (30). The measured parameters, K and K' were respectively estimated to be 0.79 and 0.33. Fig. 4.14 and Fig. 4.15 respectively denote the optimized K and K' factors calculated during calibration process.
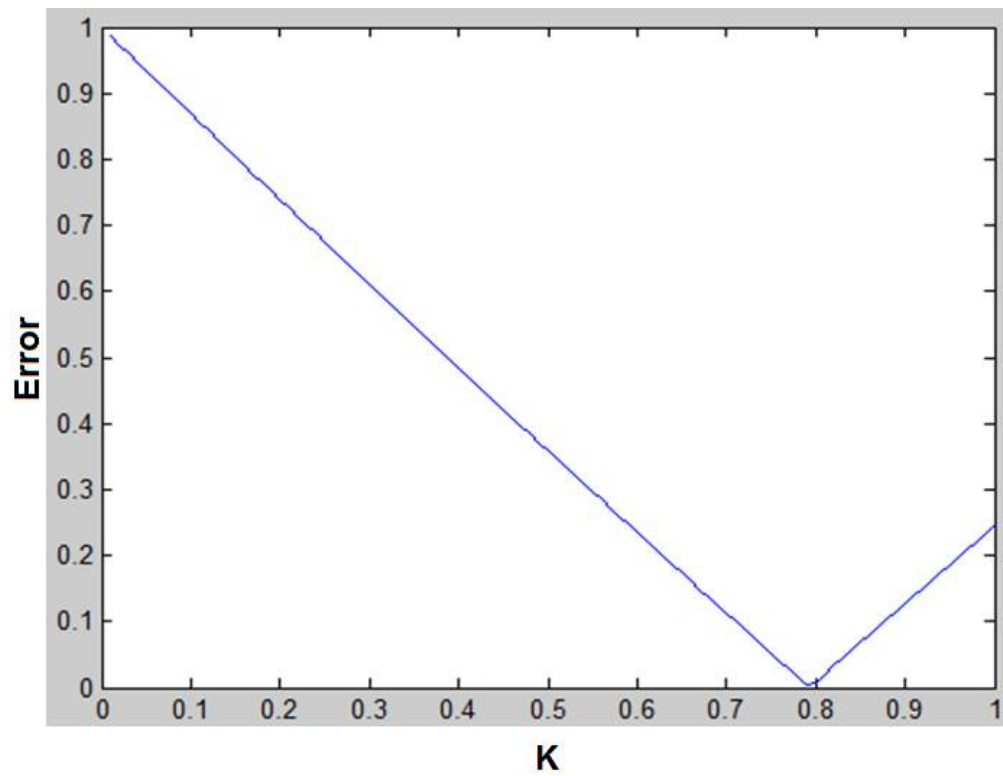
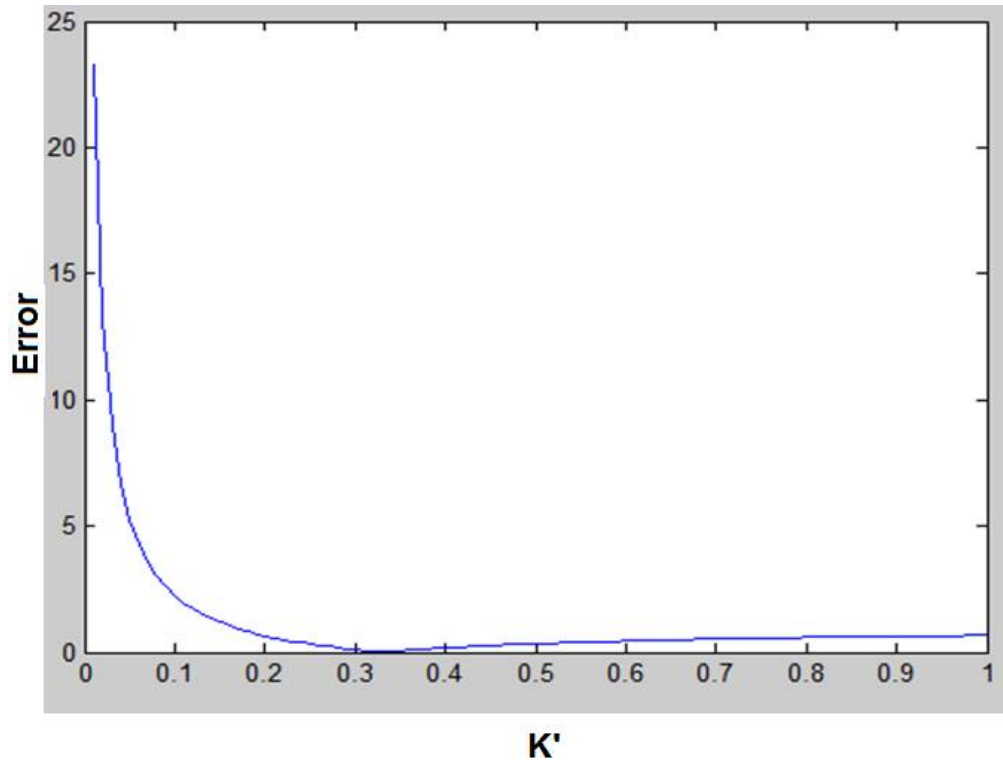**Figure 4.14 The optimized Κ coefficient versus the Error function**

Figure 4.15 The optimized Κ′ coefficient versus the Error function

126

Table 4.2 pertains to the error results from the verification tests performed on different damage levels. The error results were calculated based on the differences between the computed and measured CODs. The results for the runs from the same crack level were sufficiently close so that it was possible to consider the average value as the representative indicator of that crack level. The estimated COD compared well with the actual values measured by the FBG displacement sensors proving the promising capability of the proposed dynamic formula in quantification of crack opening using the measured BOTDA strain response.

Table 4.2 The error results between the computed and measured CODs

Damage Level	Error (%)	
	Left Joint	Right Joint
CL1	24	27
CL2	21	26.4
CL3	23	17.3
CL4	11.9	18.5
CL5	10.2	14.9
CL6	13.9	6.9
CL7	11.7	9.9
CL8	4.1	14.5
CL9	4.3	4.5
CL10	11.9	7.5
CL11	12.1	10.7
CL12	9.3	8
CL13	17.7	20
CL14	22	17.7

Fig. 4.16 schematically represents the error results versus the different CLs for both left and right joints. It is obvious that the error results are less for the middle CLs corresponding to the larger crack openings. The reason is attributed to the fact that FBG displacement sensors perform well when larger crack openings are experienced. In

127

other words, for smaller crack opening the FBG displacement sensor accuracy falls down resulting in higher error rate between measured and calculated crack openings.
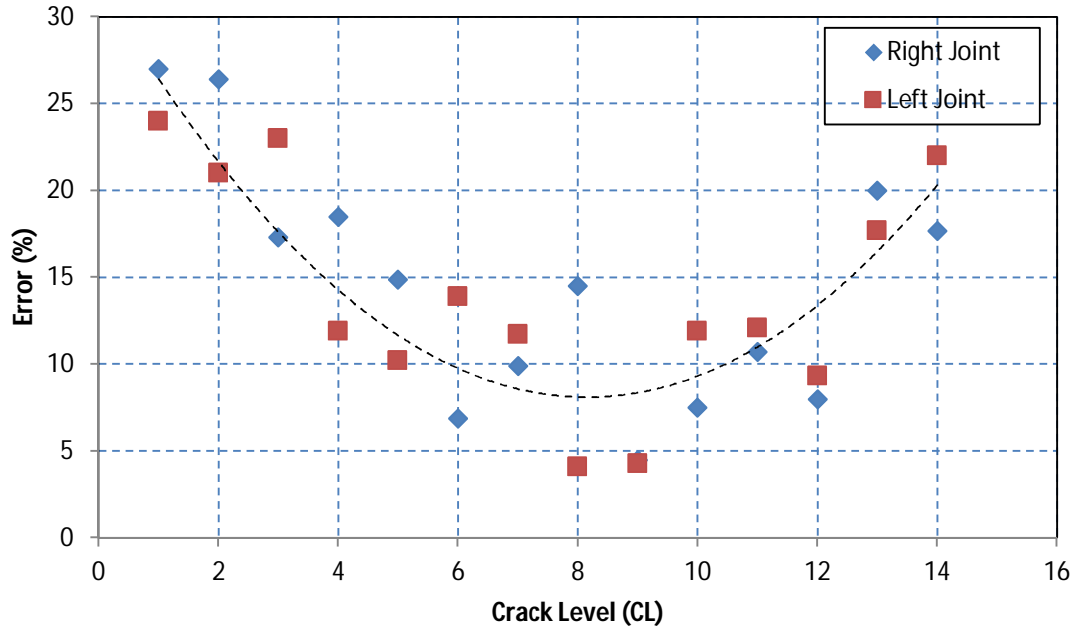
Figure 4.16 The error results versus different CLs

To study the functionality of proposed formula with respect to different range of crack openings, Fig. 4.17 demonstrates a different approach in evaluation of proposed formulation. Each data point in Fig. 4.17 corresponds to the condition when the top flange of beam, where the distributed fiber was adhered, experiences the maximum tension during the dynamic vibrations. The peak data points from all of the CLs were assembled together and plotted in Fig. 4.17. The results reveal the robust performance of elastic and elasto-plastic formulations in their capabilities for COD less than 300 microns (Note that the horizontal displacements in Fig. 4.17 correspond to the half COD , δ). However, for larger COD the behavior of fiber changes defying the elastic and elasto-plastic approaches established herein. The main reason is attributed to the fact that possible slippage occur among core-coating-adhesive-substrate interfaces at larger

deformations. Further test programs, detailed FEM analysis as well as more advanced formulation addressing the contact phenomenon in optical fiber interfaces are needed to be established.
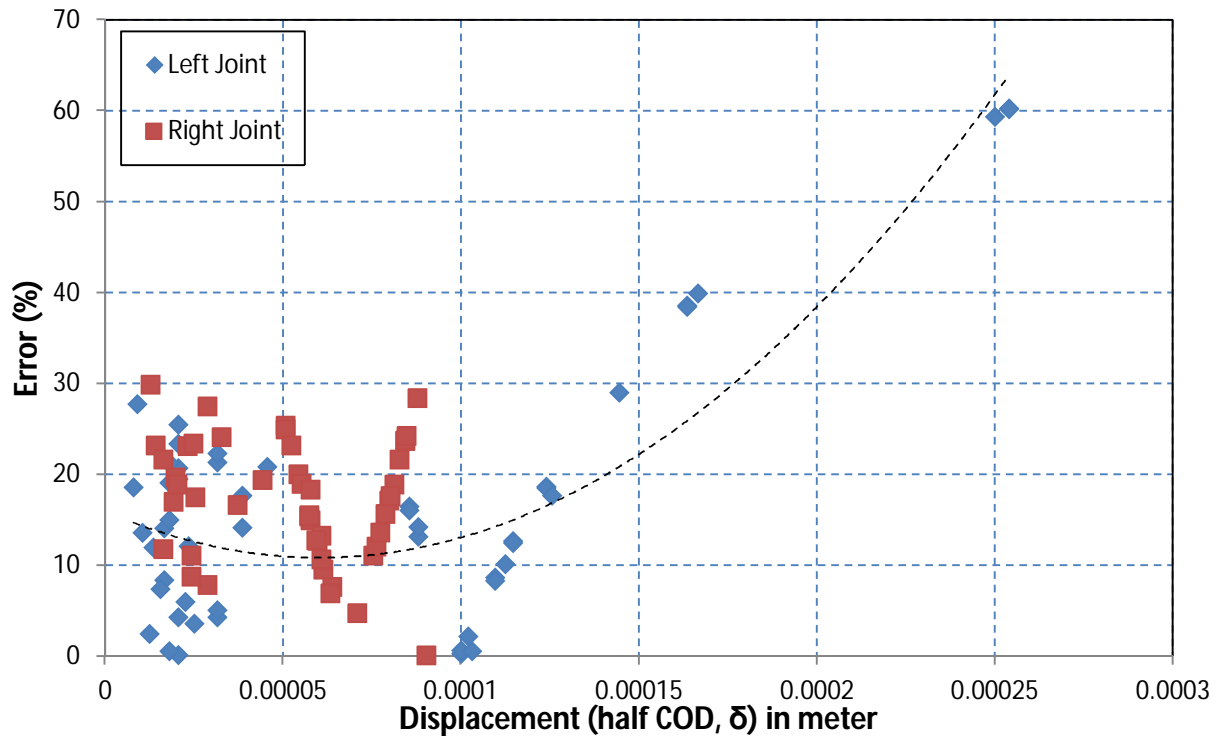
Figure 4.17 The error results versus different half COD

Fig. 4.18 through Fig. 4.20 compare the calculated and measured COD profile at the location of right joint. Fig. 4.18 through Fig. 4.20 respectively belong to the full eight seconds dynamic vibration of beam where the joint was fabricated in CL3, CL5 and CL7 conditions. In a similar manner, Fig. 4.21 through Fig. 4.23 respectively pertain to the comparison of calculated and measured COD profile at the location of left joint during CL4, CL6 and CL8 conditions. As shown in these figures, the measured and computed deflections were in phase and from the global point of view the maximum and minimum deflections correlated well. However, the amplitudes of minimum and maximum peaks in calculated displacement profile differed at few instances during the vibration loading.

The differences are major when the joint and fiber experience lower opening. This phenomenon is mainly due to the fact that the calculated crack opening is the product of BOTDA measured strain response which usually accompanies with a range of system noise as well as accuracy level. The accuracy level dramatically falls when the signal to noise ratio is less. As previously depicted in Fig. 4.16 through 4.17, the decrease of sensitivity in FBG displacement sensors measurement is also an additional source of error.
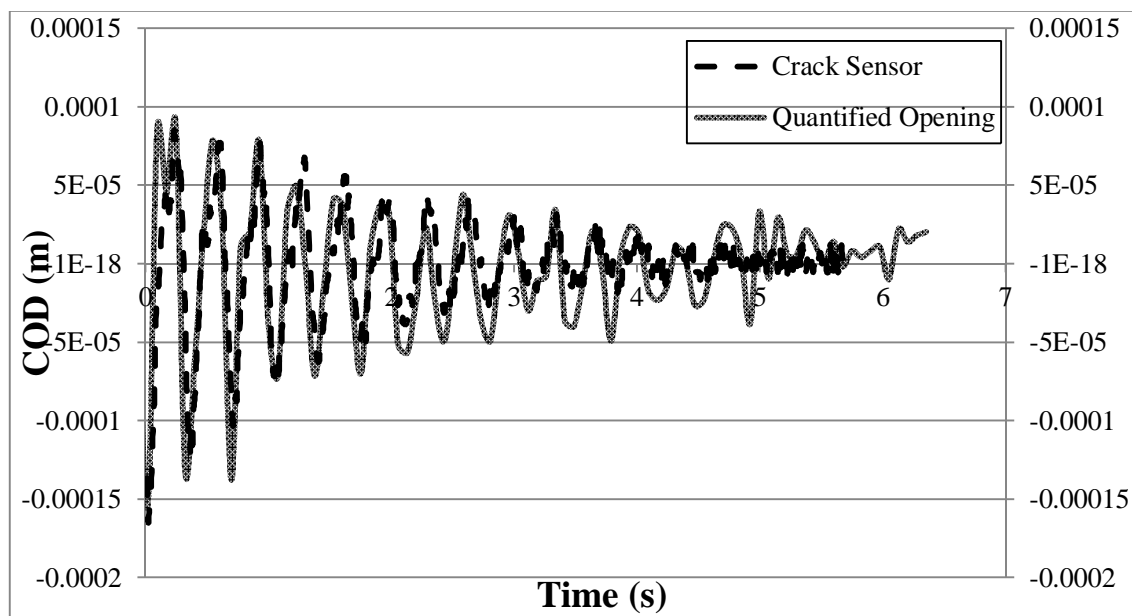
Figure 4.18 The estimated COD compared to measured COD at the location of right joint during the CL3

Figure 4.19 The estimated COD compared to measured COD at the location of right joint during the CL5
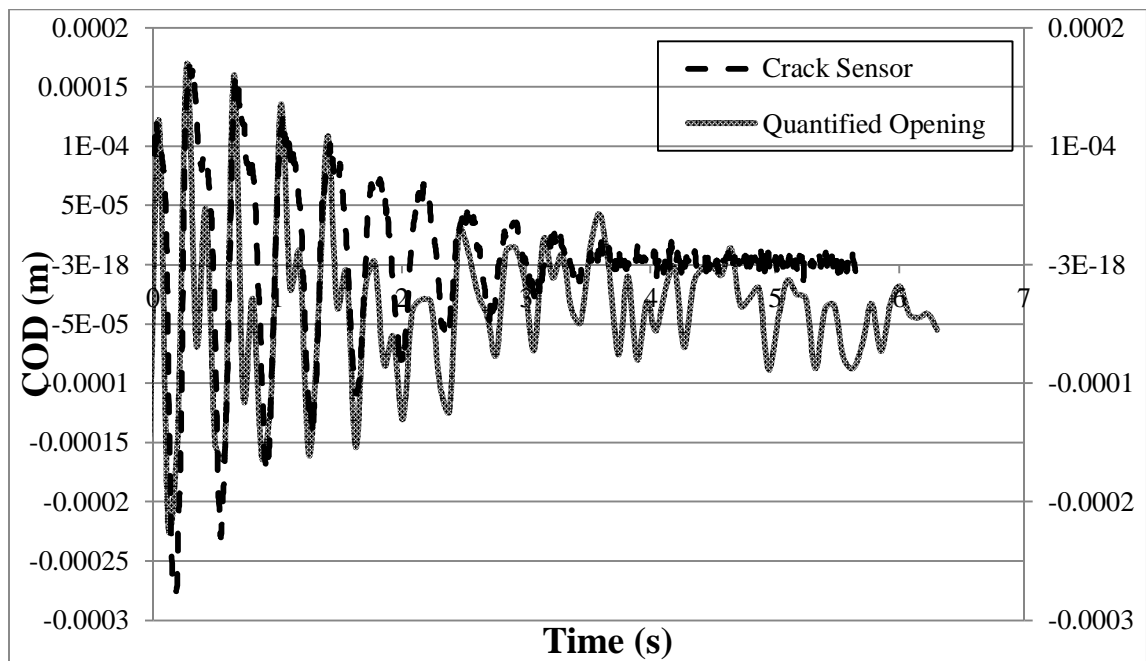
Figure 4.20 The estimated COD compared to measured COD at the location of right joint during the CL7

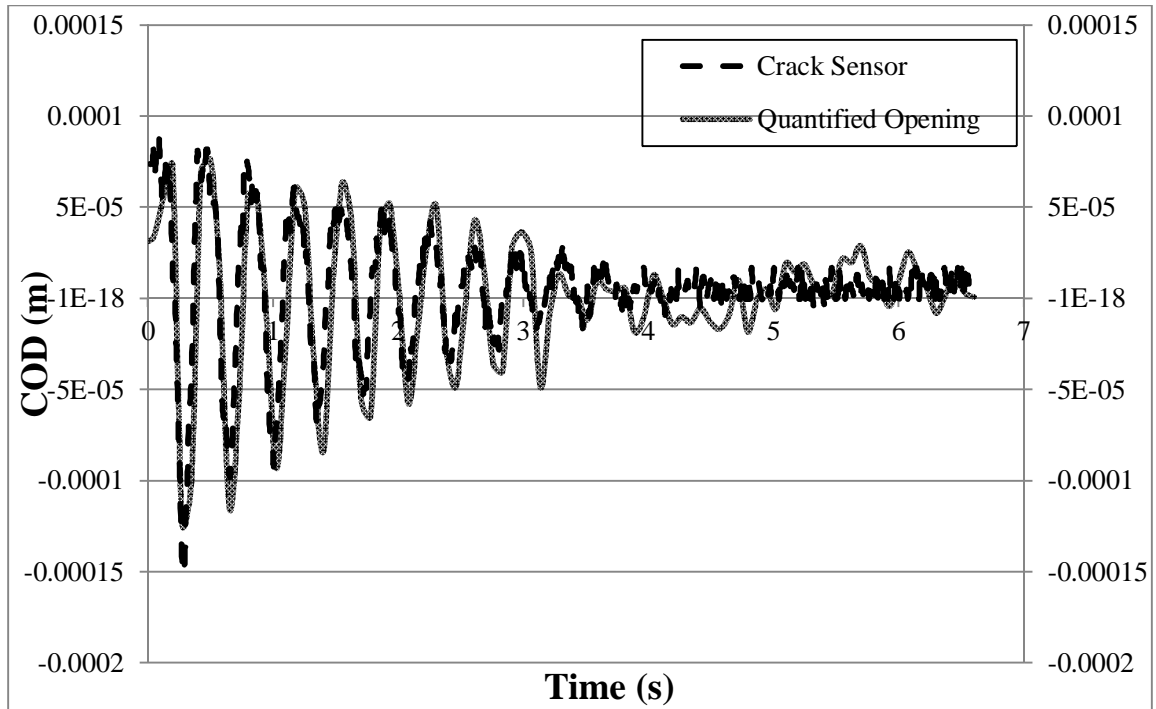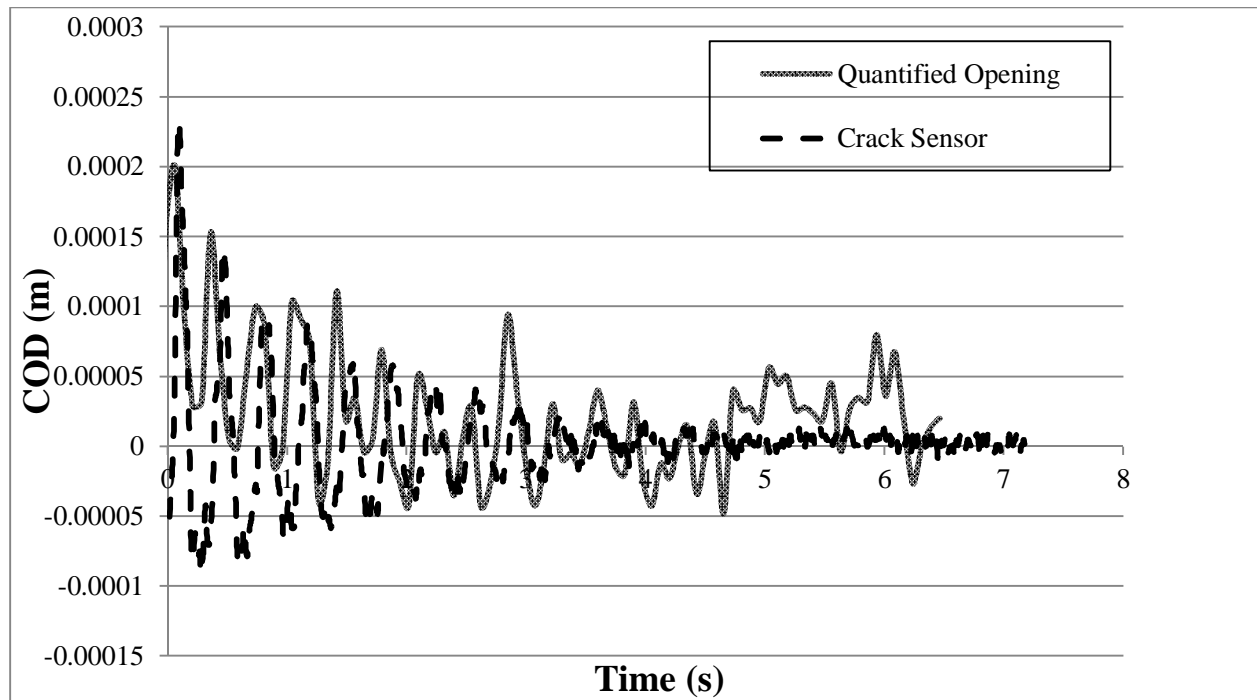**Figure 4.21 The estimated COD compared to measured COD at the location of left joint during the CL4**
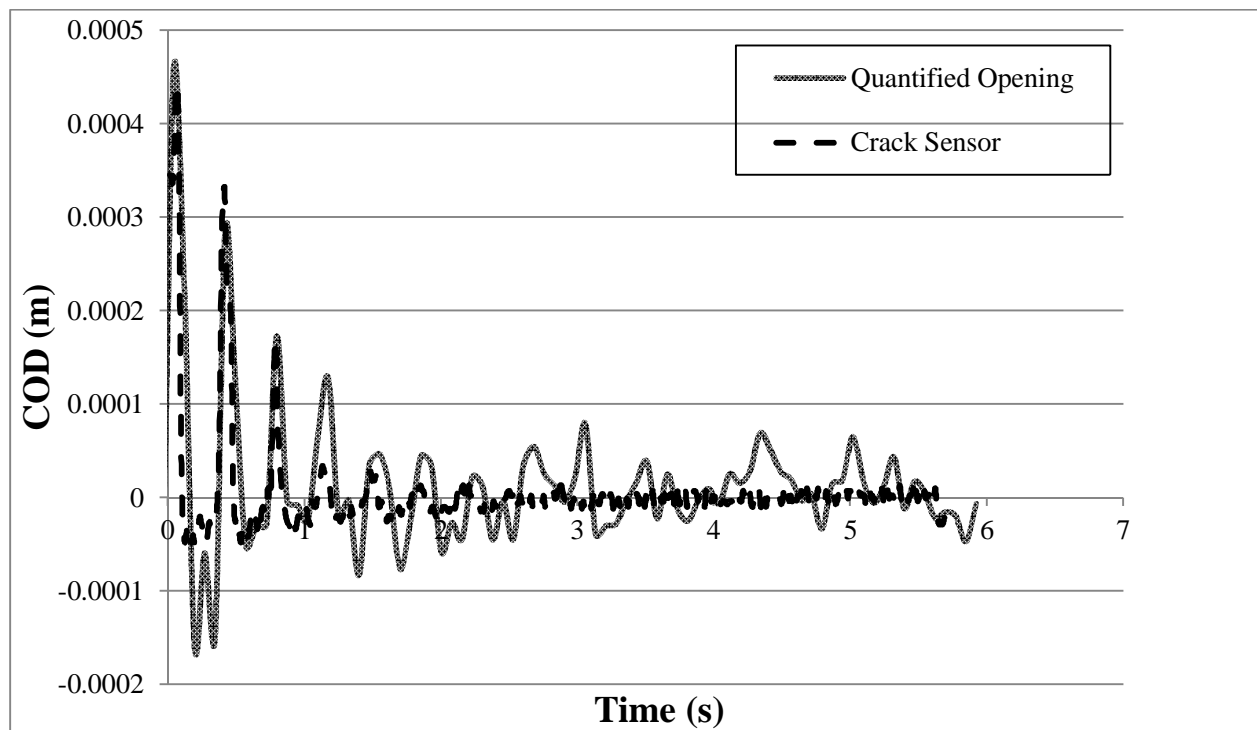
Figure 4.22 The estimated COD compared to measured COD at the location of left joint during the CL6
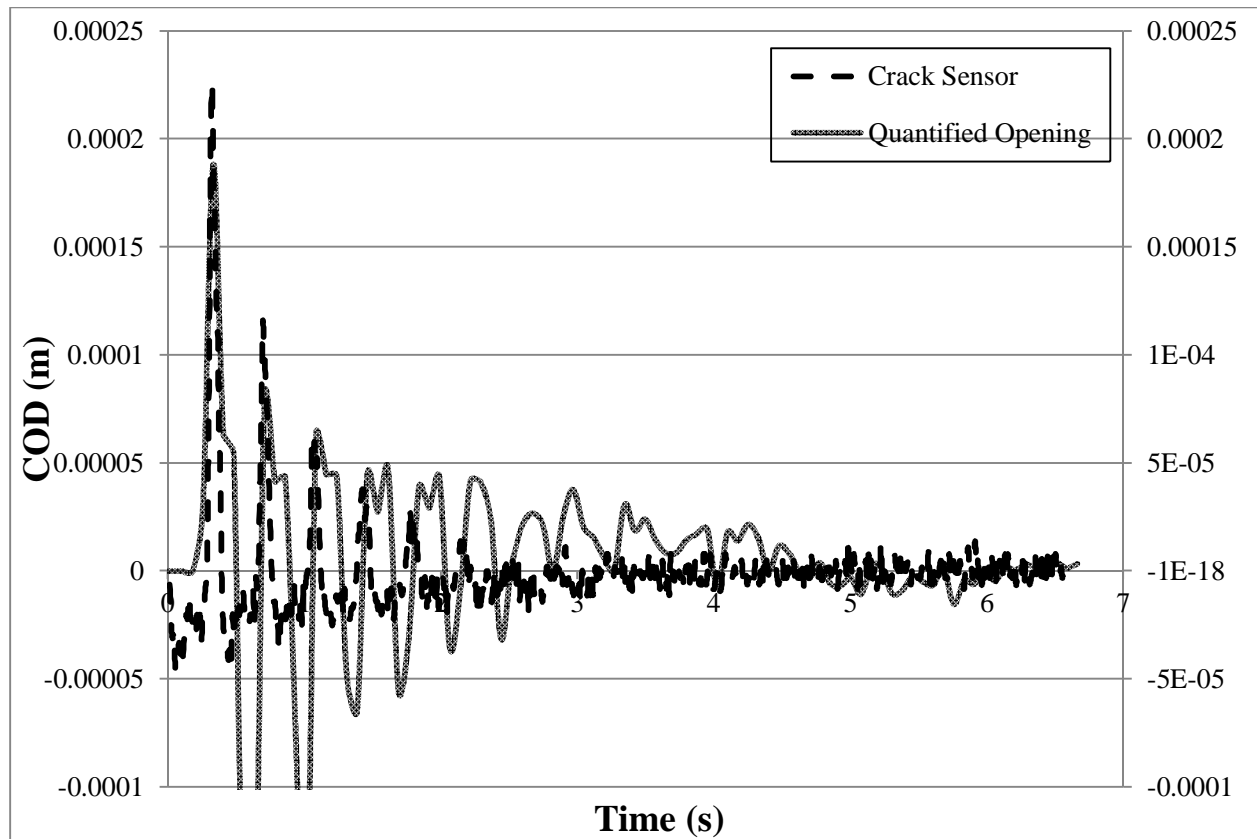
Figure 4.23 The estimated COD compared to measured COD at the location of left joint during the CL8

4.4. Summary of the chapter

In the research described herein a theoretical model is introduced to quantify cracks width based on distributed monitoring of strains in large structural systems. The theoretical approach pertains to the simulation of strain within a segment of the optical fiber traversing a crack while the structure is being vibrated. The method employs the dynamic distributed strain data to calculate the crack opening displacement. It uses a single line of optical fiber by way of Amplitude Transfer Brillouin Scattering technique in order to acquire dynamic distributed strain data. The advantage of the method developed in this study is that it quantifies the structural defects sizes while the structure is being vibrated during its in-service operation.

133

The formulations necessary to establish the strain transfer from the structure surface to the optical fiber considered both linear and nonlinear mechanical characteristics of optical fiber's components. The spatial resolution effects were also numerically implemented within the formulation in order to simulate the measurement configurations. The proposed formulation is simple and directly relates the crack opening displacement to the distributed strain. The calibration process enables the method to be easily adjusted for different measurement configurations, fibers, and adhesives with their specific mechanical and geometric properties without requiring to know their actual values. An experimental program was conducted to investigate the feasibility of the proposed approach in quantification of defects sizes. During the experimental program, a Brillouin Optical Time Domain Analyzer (BOTDA) device has been utilized in order to measure the dynamic distributed strain along the 15 meter long steel I beam fabricated with two artificial cracks ranging between 50 and 550 microns opening. The experiment was used for calibration as well as the validation of theoretical formulation. The calculated crack opening displacements agreed well with the independently installed FBG displacement sensor measurements. Fundamentally, the method provides sufficient accuracy in quantification of crack widths ranging between 50-300 microns opening. The results reveal the robust performance of elastic and elasto-plastic formulations in their capabilities for COD less than 300 microns. However, for larger COD the behavior of fiber changes defying the elastic and elasto-plastic approaches established herein.

Further test programs, detailed FEM analysis as well as more advanced formulation addressing the contact phenomenon in optical fiber interfaces are required to be

established. Also, future studies are recommended to be expanded to bridges with actual defects in order to evaluate the robustness of the proposed approach for monitoring purposes. The proposed technique herein is a fundamental investigation capable of being implemented across different types of structures, including in buildings, dams, bridges, aeronautics, and power plants.

Chapter V: Conclusions

The worldwide aging of the infrastructure and the development of new technologies in the construction industry provided a need for SHM. SHM provides a tool for owners and researchers to assess the condition of a structure and monitor its behavior under real operational conditions. To avoid major failures or catastrophic it is necessary to inspect them frequently and assure their well in-service functionality. Due to the importance of transportation and the related infrastructure for the USA's economic and social developments, it was specifically tried to innovate methodologies for safety assessment of highway bridges.

In Chapter 2, an alternative BWIM approach was developed for accurate estimation of axle weights, axle spacing, and gross weights of the trucks as they travel over the bridges. The proposed technique is based on measurement of shear strains near the bridge abutments, which is different from the traditional flexural strain based systems. The measurements are achieved by use of shear strain rosettes on the girder webs. In doing so, the trucks' axle weights could be acquired at the bridge abutments, where due to the immediacy of the force path to the bridge supports, the effects of traffic configurations as well as bridge structural parameters on the measurements are dramatically reduced. The present approach is generalized for application in both statically determinate as well as indeterminate bridges. Three different bridges, a box girder prestressed concrete located in CA, and two concrete slab on steel girder bridges with different span lengths, located in IL, were instrumented for the evaluation of the proposed BWIM system. Field implementation involved a series of truck runs for

calibration and evaluating the efficiency of the BWIM system. In addition to ambient noise at higher sampling rates, the dynamic interaction of the bridge with the trucks at highway speeds generates additional signal oscillations to the static response. Accurate detection of signal peaks requires removal of the dynamic and noisy parts of the recorded signals. The wavelet filter has been applied on the measured response in order to address the above mentioned issues. For the box girder prestressed concrete bridge located in CA, called Lambert Road Bridge, the final individual axle weight results fall less than 18.5% while the error for GVW was less than 1.5%. Similarly the final individual axle spacing results fall less than 14.5% while the error for the total length was less than 5.2%. For the first experimented concrete slab on steel girder bridge located in IL, called Salt Creek Bridge, the final individual axle weight and spacing error results were respectively less than 5.9% and 13.2%. Similarly the results of GVW and the total length errors respectively released 4.2% and 2.1% errors. In the case of second concrete slab on steel girder bridge located in IL, called Lock Street Bridge, the final individual axle weight and GVW results respectively shown errors less than 18.4% and 7.9%. The error for the axle spacing results was reported less than 9.2%. More detailed studies will need to be conducted in order to consider a number of parameters that would influence the performance of the BWIM system. For instance, the spread of the load from the surface of the deck to the rosette level is considered to be direct in relating the measurements to the computation of the axle weights. Other factors influencing the performance of the system are the bridge type and size as well as the stiffness of the bridge, which is required to be addressed in the future investigations.

In the following Chapter 3, a reference-free distributed damage detection technique has been developed to locate the defects locations within the structures under in-service operating conditions. The proposed methodology was primarily established based on the Pulse-Pre-pump Brillouin Optical Time Domain Analysis (PPP-BOTDA) method. To sense the structural perturbations corresponding to the in-service operations, i.e. aircrafts vibration during flights or bridges subjected to traffic induced vibration, the dynamic measurement capability of the PPP-BOTDA has been employed. The advantage of the method developed in this study is that it enables the structure to be monitored at any stage during its service life without the need for prior reference data. In other words, the virtual reference strain response is reconstructed by conducting Regression analysis on the strain response of damaged structure. Then, using the constructed virtual reference and subtracting from the BOTDA measured strain response; the sole effects of defect induced strain will be visible. In this manner, the locations of defects can be easily determined. Laboratory experiments were designed in order to simulate the effect of ambient conditions in bridges, especially in terms of realistic displacements, i.e. deflections occurring in highway bridges. The experimental program involved testing of a long steel beam that embodied two fabricated defects. Loading was induced in the form of free vibrations. The beam was oscillated by lifting the beam mid-span by 9 mm and then releasing it. The objective was to examine the defect detection capability, both in terms of the resolution of the measurements as well as location detection. Different damage levels were introduced in the beam in order to simulate the defect initiation and growth, and to determine the extent of detectable damage by the proposed approach. Distributed strain measurements were compared

with the defect opening displacements measured by FBG displacement sensors. The experimental results indicated that the proposed method was capable of detecting defects in the order of 50 microns in width. Fundamentally, the method enables simultaneous detection of many existing small size cracks (i.e. 50 microns) over large sections of structural systems. The experiments performed in this study involved two defects. Future research should also involve experimentation with more closely spaced defects in order to examine the effect of multiple defects, and spatial resolution on the formulation of the virtual reference. Future studies should be expanded to bridges in order to evaluate the robustness of the proposed approach for monitoring damage under ambient conditions. The fundamental techniques established here will be transformative across different types of structures, including in bridges, dams, buildings, in aeronautics, power plants, and wind turbines.

In a following effort, Chapter 4 reports the procedure of developing a theoretical model in order to analysis the strain transfer mechanism from the structure surface to the distributed optical fiber components in the presence of local defects. The main objective pertained to the accurate quantification of local crack width based on distributed monitoring of strains in large structural systems. The theoretical formulation simulated the strain distribution within the components of an optical fiber crossing over a single crack opening. The proposed model was formulated in a manner to quantify defects, specifically cracks, in the presence of structural vibration. Both linear and nonlinear mechanical characteristics of optical fiber components were also assumed in the formulation. The spatial resolution effect was further numerically implemented within the formulation in order to simulate the measurement configurations. The method employs

the dynamic distributed strain data to calculate the crack opening displacement. It uses a single line of optical fiber by way of Amplitude Transfer Brillouin Scattering technique in order to acquire dynamic distributed strain data. The proposed formulation is simple and directly relates the crack opening displacement to the distributed strain. The calibration process enables the method to be easily adjusted for different measurement configurations, fibers, and adhesives with their specific mechanical and geometric properties without requiring to know their actual values. An experimental program was designed for calibration as well as the validation of theoretical formulation. The experiments involved dynamic tests of a 15 meter long steel I beam with two fabricated defects with small opening displacements ranging between 50 and 550 microns. Fundamentally, the method provides sufficient accuracy in quantification of crack widths ranging between 50-300 microns opening. Further test programs, detailed FEM analysis as well as more advanced formulation addressing the contact phenomenon in optical fiber interfaces are required to be established. Also, future studies are recommended to be expanded to bridges with actual defects in order to evaluate the robustness of the proposed approach for monitoring purposes.

CITED LITERATURE

An, Y. K., Lim, H. J., Kim, M. K., Yang, J. Y., Sohn, H., and Chang, G. L. (2014) "Application of Local Reference-Free Damage Detection Techniques to In Situ Bridges." J. Struct. Eng., 140(3), 04013069, 1-11.

Angulo-Vinuesa, X., Martin-Lopez, S., Corredera, P., and Gonzalez-Herraez, M. (2012) "Raman-assisted Brillouin optical time-domain analysis with sub-meter resolution over 100 km." Optics Express, 20(11), 12147-12154.

Ansari, F. (2005). Sensing Issues in Civil Structural Health Monitoring, Springer Publishing Co., Dordrecht, The Netherlands.

Ansari, F. (2007). "Practical Implementation of Optical Fiber Sensors in Civil Structural Health Monitoring." J Intelligent Mater. Sys. Struct., 18(8), 879-889.

Ansari, F., and Libo, Y. (1994). "Mechanics of bond and interface shear transfer in optical fiber sensors." J. Eng. Mech., 124(4), 385-394.

Atzlesberger, J., Zagar, B. G., Cihal, R., Brummayer, M., and Reisinger, P. (2013) "Sub-surface defect detection in a steel sheet." Meas. Sci. Technol., 24, 084003.

Bao, X. (2009) "Optical fiber sensors based on Brillouin scattering." Opt. Photo. News, 20(9), 40-46.

Bao, T., Babanajad, S. K., Taylor, T., and Ansari, F. (2015) "Shear Force based Real-Time Fiber Optic Bridge Weigh-in-Motion System." J. Bridge Eng., 04015029.

Bao, X., Brown, A., DeMerchant, M., and Smith, J. (1999) "Charaterization of the Brillouin-loss spectrum of single mode fibers by use of very short (<10 ns) pulses." Optic Letters, 24(8), 510-2.

Bao, X., and Chen, L. (2011) "Recent Progress in Brillouin Scattering Based Fiber Sensors. Sensors." 11, 4152-4187.

Bao, X., DeMerchant, M., Brown, A., et al. (2001) "Strain measurement of the steel beam with the distributed Brillouin scattering sensor. In: Chase SB and Aktan AE (eds) Health Monitoring and Management of Civil Infrastructure Systems, Proceedings of SPIE, SPIE, 4337, 223–233.

Bao, X., Webb, D. J., and Jackson, D. A. (1996) "Distributed temperature sensor based on Brillouin loss in an optical fiber for transient threshold monitoring." Canadian J. Physics, 74(1–2), 1–3.

Bao, X., Yu, Q., and Chen, L. 2004 "Simultaneous strain and temperature measurements with polarization- maintaining fibers and their error analysis by use of a distributed Brillouin loss system." Optics Letters, 29(12), 1342-1344.

Bassam, A., Iranmanesh, A., Ansari, F. (2011) "A simple quantitative approach for post-earthquake damage assessment of flexure dominant reinforced concrete bridges." Eng. Struct., 33, 3218–3225.

Bernini, R., Minardo, A., and Zeni, L. (2009) "Dynamic strain measurement in optical fibers by stimulated Brillouin scattering." Optic Letters, 34(17), 2613-5.

Brown, A. J. (2011) "Bridge Weigh-In-Motion deployment opportunities in Alabama." M.Sc. thesis, The University of Alabama, Alabam, USA.

Brown, K., Brown, A. W., and Colpitts, B. G. (2005) "Characterization of optical fibers for optimization of a Brillouin scattering based fiber optic sensor." Optical Fiber Tech., 11(2), 131–145.

142

Brown, A. W., Colpitts, B. G., and Brown, K. 2007 "Dark-pulse Brillouin optical time-domain sensor with 20-mm spatial resolution" J. Lightwave Tech., 25(1), 381-386.

Brownjohn, J. M. W., Moyo, P., Omenzetter, P., and Lu, Y. (2003) "Assessment of highway bridge upgrading by dynamic testing and finite element model updating." J. Bridge Eng., 8(3), 162–172.

Cardini, A. J., and DeWolf, J. T. (2009) "Implementation of a Long-Term Bridge Weigh-In-Motion System for a Steel Girder Bridge in the Interstate Highway System." J. Bridge Eng., 14(6), 418-423.

Cawley, P. (2001) "Non-destructive testing - current capabilities and future directions." Proc. Inst. Mech. Eng. Part. L-J. Mater. Design Appl., 215(L4), 213-223.

Cawley, P., and Alleyne, D. (1996) "The use of lamb waves for the long range inspection of large structures." Ultrasonics, 34(2–5), 287–290.

Chan, T. H. T., Law, S. S., and Yung, T. H. (1999) "An interpretive method for moving force identification." J. Snd. Vib., 219(3), 503–524.

Chang, P. C., Flatau, A., and Liu, S. C. (2003) "Review paper: Health monitoring of civil infrastructure." Struct. Health Monit., 2(3), 257–267.

Chatterjee, P., O'Brien, E. J., Li, Y., and Gonzalez, A. (2006) "Wavelet domain analysis for identification of vehicle axles from bridge measurements." Comp. Struct., 84, 1792–1801.

Chaube, P., Colpitts, B. G., Jagannathan, D., and Brown, A. W. (2008) "Distributed fiber-optic sensor for dynamic strain measurement." IEEE Sens. J., 8(7), 1067–1072.

Chedister, W. C. (2002) "Evaluation of magnetic gradients for magnetic particle testing." J. Mater. Evaluation, 60(2), 1083-1088.

Chen, Y., Feng, M. Q., and Tan, C. A. (2009) "Bridge structural condition assessment based on vibration and traffic monitoring." J. Eng. Mech., 135(8), 747–758.

Chen, Z., Li, Q., Ansari, F., and Mendez, A. (2000) "Serial Multiplexing of Optical Fibers for Sensing of Structural Strains." J. Struct. Ctrl., 7(1), 103–117.

Chopra, A. K. (2011) "Dynamics of Structures: Theories and applications to earthquake engineering" 4th edition, Prentice-Hall International Series in Civil Engineering and Engineering Mechanics, New Jersey, USA.

Cui, Q., Pamukcu, S., Xiao, W., and Pervizpour, M. (2011) "Truly Distributed Fiber Vibration Sensor Using Pulse Base BOTDA With Wide Dynamic Range." IEEE Photonics Tech. Letters, 23(24), 1887-9.

Dally, J. W., and Riley, W. F. (1991) "Experimental Stress Analysis." 3rd ed., McGraw-Hill Inc., New York, 639.

Dalton, R. P., Cawley, P., and Lowe, M. J. S. (2001) "The potential of guided waves for monitoring large areas of metallic aircraft fuselage structure." J. Nondestruct. Eval., 20(1), 29–46.

Deesomsuk, T., and Pinkaew, T. (2010) "Evaluation of effectiveness of vehicle weight estimations using bridge weigh-in-motion." The IES J. Part A: Civil Struct. Eng., 3(2), 96–110.

Diaz, S., Foaleng Mafang, S., Lopez-Amo, M., and Thevenaz, L. (2008) "A high performance Optical Time-Domain Brillouin Distributed Fiber Sensor." IEEE Sens. J., 8(7), 1268–1272.

Fan, W., and Qiao, P. (2011) "Vibration-based damage Identi_cation Methods: A Review and Comparative Study, Structural Health Monitoring." 10(1), 83-111.

Farrar, C. R., and Jaureguiz, D. A. (1998) "Comparative study of damage identification algorithms applied to a bridge: I experiment." Smart Mater. Struct., 7(5), 704–719.

Feng, X., Zhang, X., Sun, C., Motamedi, M. H., and Ansari, F. (2014) "Stationary wavelet transform method for distributed detection of damage by fiber-optic sensors." J. Eng. Mech., 140(4), 04013004.

Feng, X., Zhou, J., Sun, C., Zhang, X., and Ansari, F. (2013) "Theoretical and Experimental Investigations into Crack Detection with BOTDR-Distributed Fiber Optic Sensors." J. Eng. Mech., 139(12), 1797-1807.

Foaleng, S. M., Tur, M., Beugnot, J.-. and Thévenaz, L. (2010) "High spatial and spectral resolution long-range sensing using Brillouin echoes." J. Lightwave Tech., 28(20), 2993-3003.

Fujita, M., and Masuda, T. (2014) "Application of Various NDT Methods for the Evaluation of Building Steel Structures for Reuse." Materials, 7(10), 7130-7144.

Gandomi, A. H., Yun, G. J., and Alavi, A. H. (2013) "An evolutionary approach for modeling of shear strength of RC deep beams." Mater Struct, 46, 2109–2119.

Garus, D., Krebber, K., Schliep, F. and Gogolla, T. (1996) "Distributed sensing technique based on Brillouin optical-fiber frequency-domain analysis." Optics Letters, 21(17), 1402-1404.

Gere, J. M., and Timoshenko, S. P. (1990) "Mechanics of Materials." MA: PWS-KENT Publishing, Boston, US.

Giurgiutiu, V. (2008) "Structural health monitoring with piezoelectric wafer active sensors." Elsevier, London.

Glisic, B., and Inaudi, D. (2007) "Fiber Optic Methods for Structural Health Monitoring" John Wiley & Sons, Ltd, England.

Glisic, B., and Inaudi, D. (2011) "Development of method for in-service crack detection based on distributed fiber optic sensors." Struct. Health Monit., 11(2),161–171.

González, A., Rowley, C., and O'Brien, E. J. (2008) "A general solution to the identification of moving vehicle forces on a bridge." Int. J. Num. Eng., 75, 335–354.

Greve, D. W., Neumann, J. J., Nieuwenhuis, J. H., Oppenheim, I. J., and Tyson, N. L. (2005) "Use of lamb waves to monitor plates: Experiments and simulations." Proc., SPIE 5765, Smart Structures and Materials: Sensors and Smart Structures Technologies for Civil, Mechanical, and Aerospace Systems, 281.

Gu, P., Deng, C., and Wu, F. (2009) "Direct Index Method of Damage Degree Identification Based on Local Strain Mode Shape Area of Damage Structure." Y. Yuan, J. Z. Cui and H. Mang (eds.), Computational Structural Engineering, Springer Science+Business Media B.V., 823–832.

Guo, T., Li, A. Q., Song, Y. S., Zhang, B., Liu, Y., and Yu, N. S. (2009). "Experimental study on strain and deformation monitoring of reinforced concrete structures using PPP-BOTDA." Science in China Series E: Technological Sciences, 52(10), 2859-68.

Hellier, C. (2001). Handbook of nondestructive evaluation, McGraw-Hill, Columbus, USA.

Helmi, K., Taylor, T., and Ansari, F. (2014). "Shear force-based method and application for real-time monitoring of moving vehicle weights on bridges." J. Intelligent Mater. Sys. Struct., 1045389X14529612.

146

Horiguchi, T., Shimizu, K., Kurashima, T., Tateda, M., and Koyamada, Y. (1995) "Development of a distributed sensing technique using Brillouin scattering." J. Lightwave Tech., 13(7), 1296-1302.

Hotate, K. (2000) "Measurement of brillouin gain spectrum distribution along an optical fiber using a correlation-based technique-proposal, experiment and simulation." IEICE Transactions on Electronics, 83-C(3), 405-411.

Huth, O., Feltrin, G., Maeck, J., Kilic, N., and Motavalli, M. (2005) "Damage identification using modal data: Experiences on a prestressed concrete bridge." J. Struct. Eng., 131(12), 1898–1910.

Imai, M., and Feng, M. (2012) "Sensing optical fiber installation study for crack identification using a stimulated Brillouin-based strain sensor." Struct. Health Monit., 11(5), 501-9.

Imai, M., Nakano, R., Kono, T., Ichinomiya, T., Miura, S., and Mure, M. (2010) "Crack detection application for fiber reinforced concrete using BOCDA-based optical fiber strain sensor." J. Struct. Eng., 136(8), 1001–1008.

Iranmanesh, A., and Ansari, F. (2014) "Energy-Based Damage Assessment Methodology for Structural Health Monitoring of Modern Reinforced Concrete Bridge Columns." J. Bridge Eng. 19, SPECIAL ISSUE: Recent Advances in Seismic Design, Analysis, and Protection of Highway Bridges, A4014004.

Jacob, B. (2002) "Weigh-in-motion of axles and vehicles for Europe." Final Rep. Prepared for Project WAVE, LCPC, Paris.

Jaishi, B., and Ren, W.-X. (2005) "Structural finite element model updating using ambient vibration test results." J. Struct. Eng., 131(4), 617-628.

Kalin, J., Žnidarič, A., and Lavrič, I. (2006) "Practical Implementation of Nothing-on-the-Road Bridge Weigh-In-Motion System." 9th Int. Symp. on Heavy Vehicle Weights and Dimensions, The Pennsylvania State University, Pennsylvania, USA

Kalosha, V. P., Ponomarev, E. A., Chen, L., and Bao, X. (2006) "How to obtain high spectral resolution of SBS-based distributed sensing by using nanosecond pulses." Optics Express, 14(6), 2071-2078.

Kishida, K., Che-Hien, L., and Nishiguchi, K. (2005a) "Pulse pre-pump method for cm-order spatial resolution for BOTDA." Proceedings of SPIE, The international society for optical engineering, 559.

Kishida, K., Li CH, Mizutani, T., and Takeda, N. (2009) "2cm spatial resolution brillouin distributed sensing system using PPP-BOTDA." MATERIALS FORUM VOLUME 33. Edited by Galea S, Wingkong, and Mita A. Institute of Materials Engineering Australasia Ltd.

Kishida, K., Zhang, H., Li, C-H., Guzik, A., Suzuki, H., and Wu, Z. (2005b) "Diagnostic of corrosion based thinning in steam pipelines by means of Neubrescope high precision optical fiber sensing system." Proc., Int. The 5th International Workshop on Structural Health Monitoring, Stanford University, Stanford, CA, 1363-1370.

Klar, A., Dromy, I., and Linker, R. (2014) "Monitoring tunneling induced ground displacements using distributed fiber-optic sensing." Tunneling and Underground Space Tech., 40, 141-150.

Law, S. S., Chan, T. H. T., and Zeng, Q. H. (1997) "Moving force identification a time domains method." J. Snd. Vib., 201(1), 1–22.

Law, S. S., Chan, T. H. T., and Zeng, Q. H. (1999) "Moving force identification: a frequency and time domain analysis." J. Dyn. Sys., Meas. Control. ASME, 12, 394–401.

Lechner, B., Lieschnegg, M., Mariani, O., Pircher, M., and Fuchs, A. (2010) "A Wavelet-Based Bridge Weigh-In-Motion System." Int. J. Smart Sensing Intelligent Sys., 3(4), 573-591.

Lee, J. J., Fukuda, Y., Shinozuka, M., Cho, S., and Yun, C. (2007) "Development and application of a vision-based displacement measurement system for structural health monitoring of civil structures." Smart Struct. Syst., 3(3), 373–384.

Lee, J. W., Kim, J. D., Yun, C.-B., Yi, J. H., and Shim, J. M. (2002) "Health monitoring method for bridges under ordinary traffic loadings." J. Sound Vib., 257(2), 247–264.

Lee, J.J., Lee, J. W., Yi, J. H., Yun, C.-B., and Jung, H. Y. (2005) "Neural networks-based damage detection for bridges considering errors in baseline finite element models." J. Sound Vib., 280(3–5), 555–578.

Li, W., Bao, X., Li, Y., and Chen, L. (2008) "Differential pulse-width pair BOTDA for high spatial resolution sensing." Optics Express, 16(26), 21616-25.

Li, C. H., Guzik, A., and Kishida, K. (2010) "The high-performance BOTDA based systems for distributed strain sensing." The 3rd International Forum on Opto-electronic Sensor-based Monitoring in Geo-engineering, Suzhou, China, 1-10.

Lin, X. K., Zhang, L. M., Guo, Q. T., and Zhang, Y. F. (2009) "Dynamic finite element model updating of prestressed concrete continuous box-girder bridge." Earthq. Eng. Vib., 8(3), 399–407.

Littler, J. D., Ellis, B. R. (1995) "Measuring the dynamic characteristics of prototype structures." In: Krishna P (ed) A state of the art in wind engineering. New Age International/Wiley, New Delhi, 133–154.

Liu, R. M., Babanajad, S. K., Taylor, T., and Ansari, F. (2015) "Experimental study on structural defect detection by monitoring distributed dynamic strain." Smart Mater. Struct., 24, 115038.

Lynch, J. P. (2007) "An overview of wireless structural health monitoring for civil structures." Philos. Trans. R. Soc. A., 365(1851), 345–372.

Maeck, J., Peeters, B., and De Roeck, G. (2001) "Damage identification on the Z24 bridge using vibration monitoring analysis." Smart Mater. Struct., 10(3), 512–517.

Maeder, G., Lebrun, J. L., and Sprauel, J. M. (1981) "Present possibilities for the X-ray di_raction method of stress measurement" NDT International, 14(5), 235-247.

Mair, R. J. (2008) "Tunnelling and geotechnics: new horizons." Geotechnique, 58(9), 695-736.

Meng, D., and Ansari, F. (2013). "Damped fiber optic low-frequency tiltmeter for real-time monitoring of structural displacements." Meas. Sci. Tech., 24(12), 125106.

Meng, D., and Ansari, F. (2013). "Damped fiber optic low-frequency tiltmeter for real-time monitoring of structural displacements." Meas. Sci. Tech., 24(12), 125106.

Meng, D., Ansari, F., and Feng, X. (2015). "Detection and monitoring of surface micro-cracks by PPP-BOTDA." Applied Optics, 54(16), 4972-8.

Moses, F. (1979) "Weigh-in-motion system using instrumented bridges." Trans. Eng. J., 105, 233–249.

Moses, F., and Ghosn, M. (1983) "Instrumentation for weight trucks in motion for high bridge loads." Final Rep. No. FHWA/OH-83/001, Federal Highway Administration, Ohio Department of Transportation, Ohio.

Motamedi, M. H., Feng, X., Zhang, X., Sun, C., and Ansari, F. (2012) "Quantitative investigation in distributed sensing of structural defects with Brillouin optical time domain reflectometry." J. Intelligent Mater. Sys. Struct., 24(10), 1187-1196.

Moyo, P., Brownjohn, J. M. W., and Omenzetter, P. (2004) "Highway bridge live loading assessment and load carrying capacity estimation using a health monitoring system." Struct. Eng. Mech., 18(5), 609–626.

Nair, A., and Cai, C. S. (2010) "Acoustic emission monitoring of bridges: Review and case studies." Eng. Struct., 32, 1704-1714.

Nazarian, E., Ansari, F., and Azari, H. (2015a). "Recursive Optimization Method for Monitoring of Tension Loss in Cables of Cable-stayed Bridges." J. Intelligent Mater. Sys. Struct., in press.

Nazarian, E., Ansari, F., Zhang, X., and Taylor, T. (2015b). "Detection of Tension Loss in Cables of Cable-Stayed Bridges by Distributed Monitoring of Bridge Deck Strains." J. Struct. Eng., in press.

Newland, M. (2006) "INDOT Challenge: How to Maintain Our Highway Infrastructure", Presentation available at www.fhwa.dot.gov

O'Brien, E. J., Quilligan, M., and Karoumi, R. (2006) "Calculating an influence line from direct measurements" Bridge Engineering, Proceedings of the Institution of Civil Engineers, 159 (BE1), 31-34.

Ojio, T., and Yamada, K. (2002) "Bridge weigh-in-motion systems using stringers of plate girder bridges." Pre-Proc. 3rd Int. Conf. on Weigh-In-Motion, Orlando, Florida, 209–218.

Park, G., Cudney, H., and Inman, D. J. (2000) "Impedance-based health monitoring of civil structural components." J. Infrastruct. Syst., 6(4), 153–160.

Park, S., Lee, C. G., and Sohn, H. (2010) "Reference-free crack detection using transfer impedance." J. Sound Vib., 329(12), 2337–2348.

Peled, Y., Motil, A., and Tur, M. (2011) "Distributed and dynamical Brillouin sensing in optical fibers", Optical Fiber Sensor conference, OFS21, Ottawa, Canada.

Peters, R.J. (1984) "A system to obtain vehicle axle weighing." Proc.12th Australian Road Res. Board Conf., Hobart, Australia, ARRB, 12(2), 10-18.

Peters, R.J. (1986) "CULWAY- an unmanned and undetectable highway speed vehicle weighing system." Proc.13th Australian Road Res. Board Conf., Hobart, Australia, ARRB, 13(6), 70-83.

Peters, R.J. (1998) "Low cost calibration management." Pre-Proc.2nd European Conf. on Weigh-in-Motion of Road Vehicles, Lisbon, Luxemburg, European Commission, 153-160.

Pinkaew, T. (2006) "Identification of vehicle axle loads from bridge responses using updated static component technique." Eng. Struct., 28(11), 1599–1608.

Quilligan, M. (2003) "Bridge Weigh-in-Motion: Development of a 2-D Multi-Vehicle Algorithm." Licentiate Thesis, Royal Institute of Technology, Stockholm, Sweden.

Raghavan, A., and Cesnik, C. E. S. (2007) "Review of guided-wave structural health monitoring." Shock. Vib. Dig., 39(2), 91–114.

Ravet, F., Briffod, F., Glisic, B., Nikles, M., and Inaudi, D. (2009) "Submillimeter crack detection with Brillouin-based fiber-optic sensors." IEEE. Sens. J., 9, 1391–1396.

Rose, J. (2002) "A baseline and vision of ultrasonic guided wave inspection potential." J. Press. Vess. Technol., 124(3), 273–282.

Rowley, C. W., O'Brien, E. J., González, A., and Žnidarič, A. (2009) "Experimental Testing of a Moving Force Identification Bridge Weigh-in-Motion Algorithm." Expt. Mech., 49(5), 743-746.

Lambert, L., and Crawley, J. (2011) "Federal funding needed for bridge repairs: study" Reuters report, Washington, USA (available at www.reuters.com)

Rytte, A. (1993) "Vibration based inspection of civil engineering structures." Aalborg Univerity, Aalborg, Denmark.

Shi, B., Xu, H. Z., Chen, B., Zhang, D., Ding, Y., Cui, H., and Gao, J. (2003) "A feasibility study on the application of fiber-optic distributed sensors for strain measurement in the Taiwan Strait Tunnel project." Marine Georesources and Geotechnology, 21(3-4), 333- 343.

Soh, C. K., Tseng, K., Bhalla, S., and Gupta, A. (2000) "Performance of smart piezoceramic patches in health monitoring of a RC bridge." Smart Mater. Struct., 9(4), 533–542.

Taki, M., Soto, M.A., Bolognini, G., Di Pasquale, F. (2013) "Study of Raman amplification in DPP-BOTDA sensing employing Simplex coding for sub-meter scale spatial resolution over long fiber distances." Meas. Sci. Tech., 24 (9), 094018.

Talebinejad, I., Fischer, C., and Ansari, F. (2011) "Numerical evaluation of vibration-based methods for damage assessment of cable-stayed bridges." Computer-Aided Civil and Infrastruct. Eng., 26(3), 230–251.

Van Dalen, M., Wicker, C., and Wilson, G. J., (2009) "Non-destructive testing of materials subject to atmospheric stress corrosion cracking." Insight, 51(4), 201-206.

Voskoboinik, A., Wang, J., Shamee, B., Nuccio, S., Zhang, L., Chitgarha, M., Willner, A., and Tur, M. (2011b) "SBS-based fiber optical sensing using frequency-domain simultaneous tone interrogation," J. Lightwave Tech. 29(11), 1729–1735.

Voskoboinik, A., Yilmaz, O. F., Willner, A. W., and Tur, M. (2011a) "Sweep-free distributed Brillouin time-domain analyzer (SF-BOTDA)." Optics Express, 19(26), B842-7.

Wan, K. T., Leung, C. K. Y., and Olson, N. G. (2008) "Investigation of the strain transfer for surface-attached optical fiber strain sensors." Smart Mater. Struct., 17, 035037, 1-12.

WAVE. (2001) "Weighing-in-Motion of Axles and Vehicles for Europe (WAVE): Report of Work Package 1.3." E. J. O'Brien and A. Znidaric eds., University College Dublin, Dublin, Ireland.

Wu, J. B., Kang, Y. H., Tu J., Sun, Y. H., Wu, J., Kang, Y., and Sun, Y. (2014) "Analysis of the eddy-current effect in the Hi-speed axial MFL testing for steel pipe." Int. J. Appl. Electromagnetics Mech., 45(1), 193-199.

Yamauchi, Y., Guzik, A., Kishida, K., and Li, C. H. (2007) "A study of the stability, reliability, and accuracy of Neubrescope-based pipe thinning detection system" Proc.,

Int. The 3rd international conference on structural health monitoring of intelligent infrastructure, Vancouver, BC.

Yaman, I. O., Inci, G., Yesiller, N., and Aktan, H. M. (2001) "Ultrasonic pulse velocity in concrete using direct and indirect transmission." ACI Mater. J., 450-452.

Yan, S. Z., and Chyan, L. S. (2010) "Performance enhancement of BOTDR fiber optic sensor for oil and gas pipeline monitoring." Optical Fiber Tech., 16(2), 100-109.

Yu, L., and Chan, T. H. T. (2003) "Moving force identification based on the frequency–time domain method." J. Snd. Vib., 261, 329–349.

Yu, L., and Chan, T. H. T. (2007) "Recent research on identification of moving loads on bridges." J. Snd. Vib., 305, 3–21.

Zarafshan, A. (2013) "Multi-Parameter Correlation Approach for Structural Health Monitoring of Operational Highway Bridges." PhD Thesis, Department of Civil and Materials Eng., University of Illinois at Chicago, Chicago, USA.

Zarafshan, A., and Ansari, F. (2013) "Damage Index Matrix: A Novel Damage Identification Method Using Hilbert-Huang Transformation. R. Allemang et al. (eds.), Topics in Modal Analysis, Volume 7: Proceedings of the 31st IMAC, A Conference on Structural Dynamics, Conference Proceedings of the Society for Experimental Mechanics Series 45, The Society for Experimental Mechanics.

Zhang, Z., and Ansari, F. (2006) "Fiber-optic laser speckle-intensity crack sensor for embedment in concrete Sensors and Actuators." Sensors and Actuators, A-126, 107–111.

Zhu, X. Q., and Law, S. S. (2006) "Moving load identification on multi-span continuous bridges with elastic bearings." Mech. Sys. Sig. Proc., 20(7), 1759–1782.

Zhu, W., Rose, J. L., Barshinger, J. N., and Agarwala, V. S. (1998) "Ultrasonic guided wave NDT for hidden corrosion detection." J. Res. in Nondestructive Evaluation." 10(4), 205-225.

Znidaric, A., Kalin, J., and Lavric, I. (2002) "Bridge Weigh-in-Motion Measurements on Short Slab Bridges without Axle Detectors." 3rd Int. Conf. on Weigh-in-Motion, Orlando, Florida, 231-239.

Zornoza, A. (2014) "Investigation into improving resolution of strain measurements in BOTDA sensors." Master Thesis, Department of Civil and Materials Eng., University of Illinois at Chicago, 1066-1072.

Zornoza, A., Sagues, M., and Loayssa, A. (2012) "Self-heterodyne detection for SNR improvement and distributed phase-shift measurements in BOTDA." J. Lightwave Tech., 30(8), 1066-1072.

APPENDIX

Here, I present the written permission from the journal of my published paper that has been partly used for the write up of this thesis.

For chapter 2:

Saeed Karim Baba Najad Mamaghani

EDUCATION

2012-2015 **PhD of Civil Engineering**; Structural Engineering
Department of Civil and Materials Engineering, University of Illinois at Chicago, Chicago, USA

2009- 2011 **Master of Civil Engineering**; Construction Engineering & Project Management
Department of Civil Engineering, Faculty of Engineering, University of Tehran, Tehran, Iran

2005-2009 **Bachelor of Civil Engineering**,
Department of Civil Engineering, Faculty of Engineering, University of Tehran, Tehran, Iran

EXPERIENCE

2012-2015 **Research Assistant;** at Smart Sensors and NDT Laboratory, UIC

2012-2014 **Teacher Assistant;** at Department of Civil and Materials Engineering, UIC

2006-2011 **Teacher Assistant;** at School of Civil Engineering, University of Tehran

2007-2011 **Research Assistant;** at Construction Materials Institute, University of Tehran

2009 **Internship;** ALASTI-PLAN Ing.-Büro für Bauwesen (Consulting Engineers Co.), Halle, Germany

2007 **Internship;** Soufian Portland Cement Company, Soufian, Iran

PUBLICATIONS (OUTCOMES OF RESEARCH)

- "Generalized Method and Monitoring Technique for Shear Strain Based Bridge Weigh in Motion" *Journal of Bridge Engineering*, *ASCE*, 04015029, 2015
- "Experimental study on structural defect detection by monitoring distributed dynamic strain", *Smart Materials and Structures*, IOPscience, 24(11), 2015
- "Virtual Reference Approach for Dynamic Distributed Sensing of Damage in Large Structures" *Journal of Aerospace Engineering, ASCE*, under review
- "Selecting Proper Repair System for Rehabilitation of Deteriorated Structures in Severe Environmental Conditions" *Journal of Performance of Constructed Facilities*, *ASCE*, 04015080, 2015
- "Behaviour of Slurry In filtrated Fibre Concrete (SIFCON) under triaxial compression" *Cement and Concrete Research*, *Elsevier*, 40(11), 2010, 1571-1581
- "Failure Criteria and Triaxial Behaviour of HPFRC Containing High Reactivity Metakaolin and Silica Fume" *Construction and Building Materials*, *Elsevier,* 29, 2012, 215-229
- "A Novel Approach to Strength Modeling of Concrete under Triaxial Compression" *Journal of Materials in Civil Engineering*, *ASCE*, 24(9), 2012, 1132-43
- "Numerical Modeling of Concrete Strength under Multiaxial Confinement Pressures Using LGP" *Automation in Construction*, *Elsevier,* 36, 2013, 136-144

AWARDS & HONORS & FELLOWSHIPS

2015	***PhD: Christopher B. and Susan S. Burke Poster Competition,*** CME, UIC
2005-2011	***"Brilliant Talented Student Title"*** from Iran Graduate and Admission Office, Ministry of Education, Iran
2009	***Exempt from M.Sc. Entrance Examination;*** based on owning the best ranked students in B.Sc. ***3rdStudent among 100 students***
2009	Germany's **IAESTE** committee certification
2008	Iran's **IAESTE** (International Association for Exchange of Students for Technical Experience) committee certification
2005-2006	***B.Sc.: Granted 2 Times FOE (Faculty of Engineering) Award;*** based on achieving the Second rank in academic & 2006-2007 years